HETEROSTRUCTURE POLARIZATION CHARGE ENGINEERING FOR IMPROVED AND NOVEL III-V SEMICONDUCTOR DEVICES

A Dissertation
Presented to
The Academic Faculty

By

Jeramy Dickerson

In Partial Fulfillment
of the Requirements for the Degree
Doctor of Philosophy
in
Electrical and Computer Engineering

School of Electrical and Computer Engineering
Georgia Institute of Technology
May 2014

HETEROSTRUCTURE POLARIZATION CHARGE ENGINEERING FOR IMPROVED AND NOVEL III-V SEMICONDUCTOR DEVICES

Approved by:

Dr. Paul L. Voss, Committee Chair
Associate Professor, School of ECE
Georgia Institute of Technology

Dr. Jeffrey A. Davis
Associate Professor, School of ECE
Georgia Institute of Technology

Dr. Abdallah Ougazzaden, Co-advisor
Professor, School of ECE
Georgia Institute of Technology

Dr. David S. Citrin
Professor, School of ECE
Georgia Institute of Technology

Dr. Paul Douglas Yoder
Associate Professor, School of ECE
Georgia Institute of Technology

Dr. Mohammed Cherkaoui
Professor, School of ME
Georgia Institute of Technology

Date Approved: 19 December 2013

To my lovely wife Janice; for her love, support, and sacrifice. To my wonderful children, Kimber, Katelyn, and Emma; for being constant reminders of the joy and beauty of life.

ACKNOWLEDGMENTS

I would like to thank my advisor Dr. Voss and my co-advisor Dr. Ougazzaden for their support and encouragement. They helped me learn to ask the right questions and to look for the best in every situation. I would also like to thank Konstantinos Pantzas for many helpful discussions and insights on semiconductor physics. Thanks to Chris Bishop, Peter Mckeon, Renaud Puybaret, Manas Upadhyay, Mohamed Abid, Peter Bonanno, Charles Munson, Sarah Herbison, David Swafford, and many other colleagues for making my studies a fun and enjoyable experience. Thanks to the staff at Georgia Tech and Georgia Tech Lorraine for making my academic experience run smoothly. Finally a special thanks to France Telecom and the Region of Lorraine for funding my studies.

TABLE OF CONTENTS

ACKNOWLEDGMENTS iv

LIST OF TABLES vii

LIST OF FIGURES viii

SUMMARY xv

CHAPTER 1 INTRODUCTION 1
1.1 Origin and history of the polarization engineering in III-Ns 3
1.2 Problems to be solved 5
1.2.1 Outline of Dissertation 8

CHAPTER 2 III-N PARAMETERS, POLARIZATION THEORY, DEVICE MODELING, AND CHARACTERIZATION 9
2.1 Polarization Theory 12
2.2 Simulation and modeling software 17
2.3 DLTS characterization 22

CHAPTER 3 POLARIZATION ENGINEERING FOR IMPROVED DEVICE PERFORMANCE 26
3.1 HEMT Devices 26
3.2 Robust Solar Cells 36
3.3 Semibulk InGaN 45

CHAPTER 4 POLARIZATION ENGINEERED TUNNEL JUNCTIONS FOR INGAN MJSCS 49
4.1 State-of-the-art III-N device Tunnel Junctions 51
4.2 WKB and QM methods for calculating tunneling 53
4.2.1 Comparison of WKB and QM methods 60
4.3 Calculating the PTJ current 63
4.3.1 Carrier Statistics 64
4.3.2 Tunneling Probability 64
4.3.3 The drop of the applied bias V_{AB} over the depletion region 66
4.3.4 The leading coefficient 67
4.3.5 The limits of integration 69
4.4 Resonant Tunneling Equation and MATLAB implementation 73
4.5 GaN/AlN/GaN PTJ 75
4.6 GaN/InGaN/GaN PTJ 79
4.7 PTJ designs for InGaN MJSCs 81
4.7.1 InGaN PTJ for relaxed absorption layers 83
4.7.2 InGaN PTJ for strained absorption layers 84
4.7.3 Single AlN layer PTJ for low In InGaN MJSC designs 86

4.7.4 Resonant AlN/InGaN/AlGaN double barrier PTJ for low In InGaN MJSC designs 87
4.7.5 Single AlN layer PTJ for high In InGaN MJSC designs 91
4.7.6 Resonant AlN/InGaN/AlGaN double barrier PTJ for high In InGaN MJSC designsn 92

CHAPTER 5 CONCLUSION 94
5.1 Future work 95

REFERENCES 97

LIST OF TABLES

Table 1 Parameters used in simulations. Non-referenced values are from [1]. The piezoelectric tensor values are calculated from the piezoelectric modulus values from [1]. The P_{sp} value of BGaN is still under debate and will be assumed to be the same as GaN as indicated by the asterisk. The hole effective mass is set to be equal to 1.0 for all materials. 10

Table 2 Thickness of the BGaN back-barrier needed to form either a 0.25 or 0.5 eV barrier at least 10 nm wide. The channel thickness is fixed at 30 nm. . 31

Table 3 Semibulk $In_{.1}Ga_{.9}N$ semibulk fill factor for AM0 illumination as φ and interlayer thickness are varied. 46

Table 4 Semibulk $In_{.1}Ga_{.9}N$ semibulk EQE (%) for AM0 illumination as φ and interlayer thickness are varied. 46

LIST OF FIGURES

Figure 1 (a) A GaN/$Al_{.30}Ga_{.70}$N/GaN MODFET design where polarization effects are neglected. The shaded area indicates the intentionally doped region. (b) An $Al_{.30}Ga_{.70}$/GaN HEMT design. Electron concentrations are shown by a blue dashed line and indicate the formation of a 2DEG. . 4

Figure 2 Piezoelectric values for $In_xGa_{1-x}N$, $Al_xGa_{1-x}N$, and $B_xGa_{1-x}N$. 13

Figure 3 (a,b) Polarization sheet charge polarity for Ga-faced growth. (c,d) Polarization sheet charge polarity for N-faced growth. For InGaN and AlGaN, the sign of the PCs only depends on the direction of crystal growth. The magnitude of the PCs is composition dependent. 14

Figure 4 The evolution of energy bands and carrier concentrations in a GaN/$In_{.1}Ga_{.9}$N/GaN device as a function of $In_{.1}Ga_{.9}$N thickness. (a) The energy bands for 10, 20, 40, 80 and 160 nm $In_{.1}Ga_{.9}$N layers. The potential drop is limited to 3.4 eV, the bandgap of the neighboring GaN layers. (b) The formation of 2DEG regions. (c) The formation of 2DHG regions. The 2DEG and 2DHG screen polarization charges and prohibit any further drop in potential. 16

Figure 5 The GaAs/AlGaAs/GaAs MODFET design simulated with in-house software. 19

Figure 6 The simulation results of the AlGaAs MODFET design in Figure 5. (a) The initial potential profile. (b) The initial electron concentration profile. (c) The predicted formation of a quantum well in the conduction band. (d) The formation of a 2DEG in the electron concentration profile is clearly evident. 19

Figure 7 Capacitance as a function of applied bias for a GaN schottky diode. . . . 23

Figure 8 The DLTS signal as a function of temperature for three temperature scans. The shift in the peak and the increase in peak height as a function of bias voltage, for a fixed reverse bias, is attributed to interface trap states [2]. 24

Figure 9 Capacitance as a function of applied bias for an BGaN schottky diode. . . 25

Figure 10 The general structure of HEMT designs. (a) A Standard AlGaN/GaN design. (b) An AlGaN/GaN design with a back-barrier region to improve 2DEG carrier confinement. The channel thickness is defined as the thickness of the GaN layer between the AlGaN front-barrier and the back-barrier. 27

Figure 11 (a) $Al_{.3}Ga_{.7}N/GaN/Al_{.05}Ga_{.95}N/GaN$ HEMT design. (b) Conduction band and electron concentration profile. The PCs of the $Al_{.05}Ga_{.95}N$ back-barrier introduce an electrostatic barrier to electrons in the primary 2DEG and a secondary quantum well at the $Al_{.05}Ga_{.95}N/GaN$ interface. 28

Figure 12 (a) $Al_{.3}Ga_{.7}N/GaN/In_{.1}Ga_{.9}N/GaN$ taken from [3]. (b) Conduction band and electron concentration profile. The PCs of the $In_{.1}Ga_{.9}N$ back-barrier introduce an electrostatic barrier to electrons at the $In_{.1}Ga_{.9}N/GaN$ interface. A smaller secondary quantum well is created at the $GaN/In_{.1}Ga_{.9}N$ interface. 28

Figure 13 (a) $Al_{.3}Ga_{.7}N/GaN/B_{.01}Ga_{.99}N/GaN$ taken from [4]. (b) The conduction band profile. (c) The electron concentration profile. The small electrostatic barrier created by polarization effects in the back-barrier layer are shown in the inset of the conduction band profile. 29

Figure 14 Peak carrier concentration as a function of channel thickness using a 20 nm back-barrier for $B_xGa_{1-x}N$ with x=0.0, 0.5, 1.0, and 2.0 percent. . . . 30

Figure 15 Peak carrier concentration as a function of back-barrier thickness using a 30 nm channel for $B_xGa_{1-x}N$ with x = 0.5, 1.0, and 2.0. 31

Figure 16 (a) $B_{.005}Ga_{.995}N$ back barrier designs. (b) $B_{.01}Ga_{.99}N$ back barrier designs. (c) $B_{.02}Ga_{.98}N$ back barrier designs. The evolution of the conduction band as a function of back-barrier thickness and boron content is shown in each figure. The channel thickness is fixed at 30 nm while the back-barrier thickness is increased from 10 to 50 nm in 10 nm steps. Each color represents the conduction band for a particular design. The location and thickness, in nm, of the back barrier is indicated in (a) and is the same for (b) and (c). The black curve is the conduction band for a simple AlGaN/GaN HEMT. 32

Figure 17 (a) $B_{.005}Ga_{.995}N$ back barrier designs. (b) $B_{.01}Ga_{.99}N$ back barrier designs. (c) $B_{.02}Ga_{.98}N$ back barrier designs. The evolution of the conduction band as a function of channel thickness and boron content is shown in each figure. The back-barrier thickness is fixed to 20 nm while the channel thickness is increased from 10 to 50 nm in 10 nm steps. Each color represents the conduction band for a particular design. The location and thickness, in nm, of the back barrier is indicated in (a) and is the same for (b) and (c). The black curve is the conduction band for a simple AlGaN/GaN HEMT. 32

Figure 18 Comparison of conduction band and electron concentrations for optimized BGaN design versus normal HEMT design. 34

Figure 19 Conduction back for five periods of 5 nm/5 nm $B_{.02}Ga_{.98}N/GaN$ layers with a 30 nm channel thickness. 34

Figure 20 Energy band profiles for InGaN-based solar cells. (a) Pin devices. (b) Nip devices. Blue dot-dashed lines are for $\varphi = 0.0$, red dashed lines are for $\varphi = 0.25$ and black solid lines are for $\varphi = 1.0$. Pin devices are not expected to have good efficiency for high PCs as the photo-generated carriers in the InGaN region flow in the wrong direction. Nip device energy band profiles are nearly invariant with any amount of PCs. 37

Figure 21 Possible design configurations of InGaN solar cells. (a,c) Pin devices. (b,d) Nip devices. The electric fields from PCs and p-n junctions only align with n-i-p for Ga-faced growth and p-i-n for N-faced growth configurations. 38

Figure 22 (a) Conduction and valence bands for an n-i-p device. The curves are separated on the vertical scale to facilitate comparison. (b) Electron concentrations showing 2DEG forming near the n-GaN/i-InGaN interface. (c) Hole concentrations showing 2DHG forming at the i-InGaN/p-GaN interface. For all figures, a black curve is for $\varphi = 0$; a blue curve is for $\varphi = 0.25$, and a red curve is for $\varphi = 1.0$. 39

Figure 23 Minimum InGaN layer thickness d vs. indium content for potential drop across InGaN to reach E_g, and thus maximum V_{bi}. $\varphi = 0.2$ for green symbols and curves, $\varphi = 0.5$ for purple symbols and curves, and $\varphi = 1.0$ for orange symbols and curves. Solid curves from exact theoretical expression for d_{min}, circles for low doping concentrations n=10^{16}, i=10^{16}, and p=10^{16} cm^{-3}, and triangles are for high doping concentrations n=10^{18}, i=10^{16}, and p=5x10^{17} cm^{-3}. 41

Figure 24 Conduction and valence bands of an n-i-p design with a 200 nm setback layer. Black solid curve, $\varphi = 0.25$; red dashed curve, $\varphi = 0.0$. 42

Figure 25 IV curves for setback layer designs with and without a Mg doping tail of 1 decade/30nm. The fill factor is 0.53 and 0.44 with and without a Mg tail respectively for $\varphi = 0.0$, indicated by the red dash-dotted lines. The fill factor is 0.87 both with and without the Mg tail for the $\varphi = 0.25$ polarization case indicated by the solid black curves. 43

Figure 26 Conversion efficiency for $In_{.12}Ga_{.88}N$ solar cells as a function of the thickness of the $In_{.12}Ga_{.88}N$ layer. A setback layer decreases device performance unless PCs are included. 44

Figure 27 (a) HAADF-STEM images of semibulk InGaN with arrows indicating 1.5 nm interlayers between 23nm InGaN layers. (b) Bulk 120nm-thick InGaN sample grown under identical growth conditions. 45

Figure 28 Semibulk conduction band using 1 nm GaN interlayers. Black curves correspond to $\varphi = 0$ and red curves correspond to $\varphi = 1$. 47

Figure 29 Semibulk conduction band using 4 nm GaN interlayers. Black curves correspond to $\varphi = 0$ and red curves correspond to $\varphi = 1$. 48

Figure 30 A step potential discontinuity. The boundary conditions at x=0 determine the change in ψ as it crosses from Region I to Region II. 55

Figure 31 (a) A single 4 nm, 1 eV barrier. The effective mass inside the barrier is $0.4m_O$ whereas the outside the barrier it is $0.2m_O$. (b) The transmission probability as a function of energy using the WKB and QM methods. . . 60

Figure 32 (a) A double barrier structure. (b) The resonant nature of the electron is detected in the QM method, but is not apparent in the WKB approximation. The resonant peaks occur at the eigenenergy values of the quantum well created by the two barriers. 61

Figure 33 (a-d) Normalized $|\psi|^2$ for the four eigenenergies of the quantum well formed by the two barriers. (e) $|\psi|^2$ for a non-resonant case where the transmission probability is high. The sinusoidal curve of $|\psi|^2$ outside of the QM indicates the lack of resonant conditions in this case. 62

Figure 34 (a) InGaN PTJ structure from [5]. (b) AlN PTJ structure from [6]. The formation of the 2DEG and 2DHG from the strong polarization fields changes the nature of the many components of Equation 26 such as the limits of integration and tunneling lengths. 63

Figure 35 Devices from Figure 34, zoomed to show the tunneling area of concern. (a) InGaN PTJ tunneling distances are normally shorter than the InGaN layer thickness. For a particular applied bias voltage, the tunneling distance is relatively constant with respect to electron energy. However, the distance is likely to decrease with increasingly negative bias conditions. (b) AlGaN PTJ tunneling distances are equal to the thickness of the AlGaN layer. AlGaN tunneling distances remain constant for normal bias conditions where $|V_{AB}| \leq 2V$. 65

Figure 36 Devices from Figure 34, zoomed to show the tunneling area of concern. (a) InGaN PTJ depletion region are defined as the region between the edges of the 2DEG and the 2DHG ground state energy levels. (b) The AlGaN PTJ depletion region is simply the AlGaN layer. 66

Figure 37 Devices from Figure 34, zoomed to show the tunneling area of concern. The limits of integration are determined by the ground state energy levels for both the InGaN and AlGaN PTJ designs. It is the formation of the 2DEG and 2DHG regions through polarization effects, rather than doping, that crosses the bands and permits tunneling. 71

Figure 38 Using the first 20 eigenenergies for Equation 35 results in a tunneling current within an order of magnitude of the experimental result for the 2.8 nm AlN layer. Neither the WKB or QM method predict any significant current for the 5.0 nm layer, which indicates other mechanisms are likely responsible for the high current reported. 76

Figure 39 A comparison of the tunneling current contributions of the 1st and 20th energy states. The decrease in current for higher energy states is due to both a decreased band crossing and a lower probability of carriers existing at higher energies. 76

Figure 40 (a) The I-V curve for the ground state energy level. (b) The I-V curve for the second energy state level. This second energy state is barely crossed with the lowest ground state on the valence band side. Therefore the applied bias uncrosses this band very quickly resulting in very little current contribution to the PTJ. 78

Figure 41 (a) The simulated I-V curve for the ground state compared to the experimentally achieved current. The discrepancy in the voltage scale is due to the presence of a schottky barrier as indicated above. This model predicts that only 0.06 V drops across the PTJ, the other 0.74 V is dropped across the series resistance of the GaN layers and contacts of the experimental device. 79

Figure 42 The simulated I-V curve for the second energy state. The second state is quickly pinched off with forward bias, preventing any significant contribution to the tunneling current. 80

Figure 43 The PTJ design used in ref [7]. The 4 nm thickness of the InGaN is insufficient to cross the bands using only 25 percent In. The large tunneling current values reported in the paper are likely due to trap assisted tunneling. 80

Figure 44 Simulated current using Equation 26 for the design in Figure 43. Due to the wide-bandgap of the materials involved, tunneling using either the QM or WKB methods predicts very little current for this device configuration. 81

Figure 45 A MJSC design using the 7.0 nm $In_{.40}Ga_{.60}N$ PTJ reported in [5]. The PTJ has a series resistance of less than 1.2 mΩ for 1000x AM0 concentration. 84

Figure 46 Utilizing an nip configuration for the same device as shown in Figure 45. Using strained InGaN absorption layers, in this case 100% strained, is incompatible with an InGaN PTJ region as the electric fields align in the same direction. The PTJ must utilize an electric field anti-parallel to those formed by the subcells pn junctions. 85

Figure 47 AlN for a MJSC design. The InGaN layers are assumed to be 100% strained. The high polarization induced sheet charge at the AlN/InGaN interfaces alleviates the need for n-type or p-type GaN layers to create the charge separation fields. 86

Figure 48 The I-V curve corresponding to a 2.2 nm AlN PTJ region for the device in Figure 47. The maximum current is insufficient for the device design and will limit the current through the subcells to a maximum of 500 $mAcm^{-2}$. 87

Figure 49 The location of the AlN layer, which is responsible for crossing the energy bands, and the second barrier is important. Either placing the AlN closer to the surface or closer to the substrate appears to correctly cross the energy bands as needed. (a) The AlN layer is closer to the surface of the MJSC. (b) The AlN layer is closer to the bottom of the the MJSC. (c) For the AlN layer on top, the tunneling particle through both the $Al_{.3}Ga_{.7}N$ and AlN barriers is an electron. (d) For the AlN layer on the bottom, the AlN tunneling particle is an electron. However, for the $Al_{.3}Ga_{.7}N$ layer, the tunneling particle is a hole, which will both decrease the tunneling probability as well as eliminate the possibility of resonant tunneling. 88

Figure 50 Resonant PTJ design using a double barrier configuration. The InGaN interlayer In content is slightly higher than the InGaN absorption regions on either side of the PTJ. The AlN layer is 2.2 nm, which is the thinnest possible thickness that will cross the energy bands. 90

Figure 51 Resonant tunneling through the PTJ design of Figure 50. The peak resonant current is 11.9 $mAcm^{-}3$, which is almost 24 times as large as the single barrier design. The 4.6 $m\Omega cm^2$ series resistance of the PTJ is able to support up to 7 sun illumination. The triangular shape of the I-V curve is characteristic of resonant tunnel diodes. The WKB current is also shown here, magnified 1000 times, and is another indicator that the current is due to resonant effects of the double barrier design. 90

Figure 52 A single barrier PTJ for a multi-junction solar cell consisting of $In_{.25}Ga_{.75}$ and $In_{.51}Ga_{.49}N$ for the top and bottom subcells, respectively. Due to the strong PC charges from the 100% strained layers, only 1.6 nm of AlN is needed to cross the conduction and valence bands. 91

Figure 53 The I-V curve predicted for the device in Figure 52. 92

Figure 54 A double barrier PTJ for a multi-junction solar cell consisting of an $In_{.25}Ga_{.75}$ top subcell and an $In_{.51}Ga_{.49}N$ bottom subcell. Due to the strong PC charges from the 100% strained layers, only 1.5 nm of AlN is needed to cross the conduction and valence bands. 93

Figure 55 The I-V curve for the PTJ of Figure 54. The triangular shape predicted by the QM method is indicative of a strong resonant tunneling effect. . . 93

SUMMARY

Innovative electronic device concepts that use polarization charges to provide improved performance were validated. The strength of the electric fields created by polarization charges (PCs) was suggested to act as an additional design parameter in the creation of devices using III-nitride and other highly polar materials. Results indicated that polarization induced electric fields can replace conventional doping schemes to create the charge separation region of solar cells and would allow for a decoupling of device performance from doping requirements. Additionally, a model for calculating current through polarization induced tunnel diodes was proposed. The model was found to agree well with experimental current values. Several polarization induced tunnel junction (PTJ) designs were analyzed. A novel double-barrier PTJ was conceived that would allow for the creation of a multi-junction solar cell using strained InGaN absorption layers. Future research would include the fabrication of these devices and the inclusion of thermal effects in the model for calculating current through PTJs.

CHAPTER 1

INTRODUCTION

In 1989 magnesium was reported as a suitable means of p-doping GaN [8], which enabled the fabrication of III-nitride (III-N) based semiconductor devices. The III-N system, which includes AlGaN, InGaN, and BGaN, exhibits many useful qualities such as large breakdown fields (3.5 MV cm^{-1}), large saturation and overshoot velocities ($3x10^7$ cm s^{-1}), and high two-dimensional electron gas (2DEG) densities ($>10^{19}$ cm^{-3}) [9]. AlGaN is a wide-bandgap material system whose bandgap extends from a very insulating 6.14 eV (202 nm wavelength) for AlN to 3.43 eV (361 nm wavelength) for GaN [1]. Additionally, AlGaN HEMT devices display superior power and frequency handling capabilities when compared with other material systems such as GaAs [10], thus making AlGaN an excellent candidate for millimeter-wave and power-switching applications. Improvement of solar cell efficiency beyond the current record of 43% [11] requires further development of wide-bandgap material systems. InGaN is a direct bandgap material with a large absorption coefficient, around 10^{14} cm^{-1} for photon energies close to the bandgap, through the entire compositional range. The bandgap of InGaN ranges from 0.69 eV (1823 nm wavelength) for InN [12] to 3.43 eV (361 nm wavelength) for GaN. Because the InGaN bandgap is both direct and covers a significant portion of the solar spectrum, it is an attractive candidate for the top sub-cell, or potentially all of the sub-cells [13], of a multi-junction solar cell (MJSC). The InGaN system also shows high resistance to radiation deterioration, which makes it a useful material for space applications [14].

As part of the increased interest in the III-N system, the strong spontaneous and piezoelectric polarization effects, resulting from the wurtzite crystal structure, were carefully investigated [15, 16]. The ab-initio values used to calculate these sheet charge densities indicate that they are one to ten orders of magnitude higher than many other III-V or II-VI materials [17]. Modern theories of polarization have developed *Ab initio* predictions of

polarization charges (PCs), which are in close agreement with experimental results. For instance in the AlGaN system, theoretically obtained PC values are only 20% larger than experimentally determined values [18].

Many practical challenges exist for the III-N system. The unintentional n-type doping [19, 20] and the high threading dislocation density of GaN promote unfavorable current leakage [21] and limit the output power of high-frequency HEMT operation. The growth of thick, high-quality InGaN layers, important for solar cell applications, poses many challenges that are due to indium segregation effects [22–24]. Experimental work has demonstrated that most thick InGaN epitaxial films exhibit double diffraction and luminescence peaks [25, 26] indicative of poor material quality. Recent work from our group demonstrated a method of obtaining a thick InGaN layer with a single diffraction and luminescence peak by growing ultrathin (~1.5 nm) GaN interlayers every 25 nm of InGaN growth [24].

1.1 Origin and history of the polarization engineering in III-Ns

The polarization effects of the III-N material system have historically been underestimated, or even ignored, in device simulation and design. Knowledge of polarization-induced effects in III-N material devices has led to increased simulation accuracy. For example, the research of polarization in III-Ns has led to novel devices such as AlGaN/GaN High Electron Mobility Transistors (HEMTs) that rely exclusively on PCs to form the highly conducting electron channel. Furthermore, polarization charge engineering has been effectively used to increase performance of AlGaN/GaN HEMTs [3] and have been shown as a possible explanation for the poor performance of conventional p-i-n InGaN solar cells [27, 28]. Indeed, as will be seen below, the full potential of the polarization effect has only recently been utilized and merits careful consideration.

The rapid evolution of the AlGaN/GaN HEMT device from a theoretical to a commercialized device will be used to illustrate the usefulness of polarization engineering. Classical HEMT devices, often referred to as modulated-doping field effect transistors (MODFETs), utilize the doping of heterojunctions to create the 2DEG carrier channel. A MODFET design similar to an AlGaAs/GaAs MODFET is shown in Figure 1. The first AlGaN/GaN HEMT [29] was demonstrated in 1993. In the years that followed, experimental work rarely mentioned polarization effects, and modulated doping was used to create the 2DEG [30]. During this time an understanding of polarization induced effects on devices was increasing [31–33]. As a result, by 1999, polarization effects were considered as equally important as modulated doping schemes [34]. However, by 2002, the full potential of polarization was understood and it was shown that the electron concentration of the 2DEG region could be controlled by the thickness and composition of the AlGaN top layer [35]. The large PCs existing at the AlGaN/GaN interface create the 2DEG with no intentional doping needed, as seen in Figure 1(b).

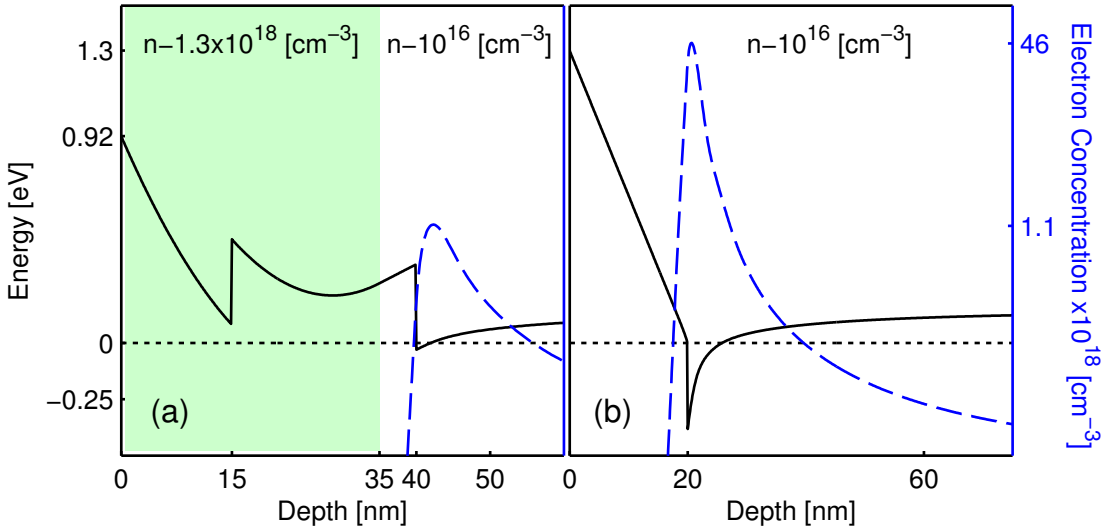

Figure 1: (a) A GaN/$Al_{.30}Ga_{.70}N$/GaN MODFET design where polarization effects are neglected. The shaded area indicates the intentionally doped region. (b) An $Al_{.30}Ga_{.70}$/GaN HEMT design. Electron concentrations are shown by a blue dashed line and indicate the formation of a 2DEG.

A similar trend in the treatment of polarization effects is found in the evolution of InGaN-based solar cells. InGaN-based solar cells did not receive much attention until after the bandgap of InN was discovered to be 0.69 eV in 2003 [12]. Many of the original papers on these devices mention very little, if any, polarization-based effects [36–41]. However, evidence for polarization effects were not apparent in these experimental works, which is likely correlated to the difficulties of achieving thick, strained InGaN layers. PCs in InGaN devices arise primarily as a result of piezoelectric polarization from pseudomorphically stained growth. As will be explained in the section on polarization theory, the piezoelectric polarization is zero for relaxed layers. As material quality continues to improve for coherently strained InGaN layers, polarization is expected to play an increased role in device design [27, 28, 42]. Additionally, polarization effects are being explored in novel device concepts such as polarization-induced doping [43], which may further increase InGaN solar cell efficiency.

1.2 Problems to be solved

Heterojunction polarization charge engineering is the design, simulation, and modeling of polarization effects in devices. The objective of polarization engineering is to consider polarization to be as important of a parameter as doping schemes, bandgaps, and layer thicknesses in determining device functionality. The strength of the electric fields created by PCs is expected to have a dramatic impact on devices created with III-nitride materials. However, polarization engineering is still in its infancy with most reported simulations and modeling done in the last decade.

The objective of this dissertation is to validate innovative electronic device designs through the careful simulation of polarization charge effects. Four possible applications will be studied. First, PCs occurring in strained layers form electrostatic barriers that influence carrier concentrations in devices that can increase carrier confinement. This can be utilized to increase the performance of devices such as AlGaN/GaN HEMTs. Specifically, BGaN will be studied as the material of choice for the creation of a back barrier layer. Polarization-induced electric fields will be shown to greatly increase carrier confinement near the AlGaN/GaN interface. This is useful for high frequency applications as poor carrier confinement decreases the maximum frequency of operation.

Second, polarization induced electric fields can significantly impact InGaN solar cell performance. Traditionally, doping schemes are used to create the charge separation region of solar cells. Solar cells rely on active regions formed by p-n junctions to separate photogenerated carriers. Polarization induced electric fields have been experimentally measured to be as large as 2.45 MV cm^{-1} with just 18% indium [44]. This field would constitute a potential drop of 2.5 eV in 10.2 nanometers. Such strong electric fields could assist or possibly replace the electric fields created historically through p-n junctions. In fact, the large PCs in pin configurations, which are designs that have a p-type layer on top and a n-type layer on the bottom of a device, can decrease efficiency to unacceptable levels. On the other hand, for nip configurations, PCs can create robust solar cells by allowing for minimal

p-type doping, thinner window layers, and the insertion of setback layers to prevent dopant diffusion. This research will investigate the use of PCs to form active regions with zero or minimal p-doping.

Third, for solar cell applications, thick InGaN layers are needed to increase photo-generated current. Growing high quality, thick InGaN layers is difficult as thick layers often lead to 3D growth transitions that severely degrade material quality. Our group has shown that periodically introducing a thin GaN interlayer into the InGaN layer increases the quality of the InGaN layer. These layers of InGaN, with GaN interlayers, are called semi-bulk InGaN and could provide a way to increase the efficiency of InGaN solar cells. Due to the inherent high quality of growth, semi-bulk layers are expected to exhibit high levels of strain and thus have PCs on the GaN / InGaN interfaces. The effects of these PCs are investigated to determine if they are detrimental to device performance. A relation between the thickness of the GaN interlayers and the total amount of strain will be studied to determine an optimal growth configuration.

Finally, due to the very wide spectrum of light that the InGaN material can absorb, InGaN is an ideal candidate for multi-junction solar cell (MJSCs) applications. In MJSCs, tunnel junctions are essential components that allow individual subcells to be connected in series to allow for current flow. Normal tunnel diodes make use of non-local band to band tunneling between an n+ and p+ region. The high levels of doping create very strong electric fields that place the conduction band within a few nanometers of the valence band. An electron can subsequently tunnel to the valence band and recombine with a hole; thus permitting photo-generated carriers to travel through subcells to the contacts and out of the device. Unfortunately, p-type doping has long been a limiting factor for wide-bandgap materials such as AlGaN, GaN, ZnO and MgZnO. The doping required for a highly conductive tunnel junction is on the order of 10^{20} cm^{-3} for both n-type and p-type regions. These levels of p-type doping are not currently possible. Thus without a method for creating efficient tunnel junctions, the creation of MJSCs using InGaN will not

be possible even if high quality InGaN growth is achieved.

Recent work has experimentally demonstrated tunnel junction diodes based on polarization-induced electric fields [5, 6, 45]. This work will investigate the nature of these tunneling diodes. The WentzelKramersBrillouin (WKB) method for predicting the tunneling probability is often used along with a standard analytical expression for estimating current through classical tunnel junctions. However, the derivation of the standard current equation for TJs fails to take into account the 2D density of states that are often involved in polarization-induced tunnel junctions (PTJs). A mathematical model is introduced and shown to closely match experimental results to within one or two orders of magnitude.

The forward bias current predicted in Ref. [5] is adequate even 1000 sun illumination. However, the design used in this paper is a PTJ where strained InGaN provides the strong electric field needed to enable tunneling. As we will show, this design is only useful if the InGaN absorption layers are completely relaxed. For strained InGaN absorption layers AlN must be used to create the PTJ region. However, the model for calculating the current in PTJs indicates that using a single-barrier AlN layer, as experimentally demonstrated in Ref. [6], is incapable of providing enough current for even 1 sun illumination. A novel double barrier design is introduced that utilizes two thin AlGaN layers. Because of the addition of the second barrier, the phenomena of resonant tunneling can be used to greatly increase the tunneling current. Resonant tunneling effects cannot be predicted with the WKB tunneling approximation so the quantum matrix method, which uses the wavelike nature of electrons to predict tunneling, is used to calculate the tunneling probability. The resonant tunneling through these double barrier devices is shown to provide enough current for multiple sun illumination. This paves a way for the creation of MJSC based solely on the III-N material system.

1.2.1 Outline of Dissertation

This dissertation is organized as follows. Chapter 2 will contain information on III-N parameters used in simulations, details of polarization theory, methods used for modeling devices, and the use of DLTS as a characterization tool for III-Ns. The result of polarization engineering on HEMT, InGaN solar cells, and InGaN semibulk devices are detailed in chapter 3. The modeling of polarization based tunnel junctions will be described in chapter 4. This chapter will explain the theoretical foundations for calculating tunneling, the model created for estimating tunneling current, comparisons of the model with experimentally reported devices, and design configurations for MJSC devices. Chapter 5 will be the conclusion and discussion of possible future studies.

CHAPTER 2

III-N PARAMETERS, POLARIZATION THEORY, DEVICE MODELING, AND CHARACTERIZATION

The accuracy of simulations is only as good as the accuracy of the parameters used. Compared to the parameters for GaAs and Si, knowledge of the III-N material system parameters is relatively new. As such, many of the common material parameters are the subject of ongoing research. For example the bandgap of InN was assumed to be nearly 1.97 eV until it was demonstrated to be closer to 0.68 eV in 2003 [12]. The discrepancy in the actual height of the bandgap was due to the poor material quality of the InN material growth before the discovery. In 2003 a comprehensive review of the III-N material system parameters was published [1]. The parameter values used in our simulations are the recommended values from this extensive review and often represent a simple average of multiple studies and published results. In addition BGaN, which is a material system actively researched in our group, is still relatively unknown and is in fact not mentioned in Ref. [1] despite being a member of the III-N family. A list of the values used in our simulations is shown in Table 1.

The parameter values for the ternary materials $Al_xGa_{1-x}N$, $In_xGa_{1-x}N$, and $B_xGa_{1-x}N$ are calculated from the binary constituents through Equation 1:

$$\text{Al,In,B}_x\text{Ga}_{1-x}\text{N} = \text{A}x + \text{B}(1-x) + \text{C}x(1-x), \text{where } (0 \leq x \leq 1). \quad (1)$$

The parameter A indicates the parameter value for AlN, InN or BN; while B indicates the parameter value for GaN. The parameter C is a bowing parameter used for material bandgaps, where C= 1.4 for InGaN [49], C= 0.7 for AlGaN [1], and C= 9.2 for BGaN [50]. A bowing parameter also exists for P_{sp} and is C=0.021 for AlGaN and C=0.037 for InGaN. BGaN assumes the same P_{sp} as GaN as explained later and thus does not have a bowing coefficient. The value C is set to zero for all other parameters to indicate a simple linear interpolation.

Table 1: Parameters used in simulations. Non-referenced values are from [1]. The piezoelectric tensor values are calculated from the piezoelectric modulus values from [1]. The P_{sp} value of BGaN is still under debate and will be assumed to be the same as GaN as indicated by the asterisk. The hole effective mass is set to be equal to 1.0 for all materials.

Parameter	Symbol	GaN	InN	AlN	BN
Static Dielectric Constant	ε_s	8.9 [46]	10.5 [47]	8.5 [46]	6.8 [46]
BandGap (eV)	E_g	3.43	0.68 [12]	6.14	5.73
Electron Effective Mass	m_e^*	0.20	0.07	0.32	0.35 [46]
Lattice Constant (nm)	a	0.3189	0.3545	0.3112	0.255 [46]
Elastic Constants (Gpa)	c_{13}	106	92	108	61 [48]
Elastic Constants (Gpa)	c_{33}	398	224	373	1061 [48]
Piezoelectric Tensor (C m^{-2})	e_{13}	-0.527	-0.484	-0.536	0.31 [48]
Piezoelectric Tensor (C m^{-2})	e_{33}	0.895	1.058	1.561	-0.94 [48]
Spontaneous Polarization (C m^{-2})	P_{sp}	-0.034	-0.042	-0.09	-0.034*

There are no well-established bowing parameters for the piezoelectric constants (e_{13} and e_{33}) or elastic tensor constants (c_{13} and c_{33}), so a simple linear approximation is used. Polarization charges can be screened as a result of defects, relaxation, and free carriers. These screening mechanisms will have a more substantial influence on any device design than any, comparatively small, nonlinear variations of the polarization parameters. A detailed discussion of the elastic constants and piezoelectric coefficients can be found in [51]. Additionally, as indicated in Ref. [51], a simple linear interpolation produces valid results and is good for indicating the order of magnitude of the polarization effects. In other words, while the polarization parameters are actually non-linear functions of composition [35], a non-linear model is currently not expected to greatly increase the accuracy of simulations.

The discovery of 0.68 eV as the bandgap for InN lead to a surge in InGaN solar cell research. The equation for calculating the absorption coefficient, α, as taken from Ref. [52], is shown here:

$$\alpha(x, E) = 10^5 \sqrt{(3.53 - (6.02x))(E - E_g(x)) + (-0.66 + (2.25x))(E - E_g(x))^2}. \quad (2)$$

The absorption coefficient, in units of cm⁻1, is a function of indium incorporation, x, and the energy, E, of incident photons, where $E \geq E_g$ and $x \leq 0.5$. Carrier mobility equations, as a function of doping, are also taken from Ref. [52] and room temperature is assumed in simulations.

The bandgap difference between AlN and GaN is 2.7 eV. When a heterointerface is formed, a portion of this discontinuity is distributed to the conduction band and is called the conduction band offset (CBO). The remainder is distributed to the valence band and is called the valence band offset (VBO). The values for the VBO range from 0.15 to 1.38 eV in experimental work [1]. This corresponds to a CBO that is 49-94% of the bandgap difference. A CBO of 1.89 eV, or 70% of the bandgap difference, was used for the devices in Chapter 3. However, in an attempt to match the tunneling estimations found in Ref. [6], CBO was changed to have a value of 2.1 eV. For InGaN, 70% of the bandgap offset between InGaN and GaN is attributed to the conduction band offset. In the Silvaco software this is taken into account by adjusting the electron affinity of each material involved.

2.1 Polarization Theory

The III-N system is unique from many other systems in that the crystal lattice is highly polar. In a macroscopic view, the polarization of the III-N system can be defined as dipolar; which means that like water molecules, the unit cell of III-Ns has a positive and negative side. III-N polarization is a result of the orientation of atoms in the crystal structure and is not dependent on external electric fields; therefore, it should not be confused with dielectric polarization. Because these dipole charges are equal and opposite for a given unit cell, only the surfaces of a given epitaxial layer form sheet charges [53]. Thus polarization can be thought of as a bulk property [54].

Unfortunately, *ab initio* calculations of polarization cannot be constructed from such a simplified view. Calculations for bulk systems must use periodic unit cells. Since the unit cell is not unique, different dipole values could be obtained for each configuration. Polarization is calculated through the use of quantum mechanics. The information needed to precisely describe polarization is contained in a system's wave functions, specifically in the phase of the wave functions. The details of this theoretical approach are outlined in [15, 16]. The following review of the critical results of III-N polarization theory is partially taken from my paper accepted for publication in *The European Physical Journal - Applied Physics* [55], a more detailed description can be found in [35, 51, 56].

The two classifications of polarization are spontaneous polarization (P_{sp}) and piezoelectric polarization (P_z). Spontaneous polarization in the III-N system arises from deviations of a material's lattice constants from those of the ideal wurtzite crystal structure. AlN has a spontaneous polarization coefficient of -0.09 Cm^{-2}, which is the highest of semiconductor materials [35]. The P_{sp} coefficients of GaN and InN are -0.034 Cm^{-2} and -0.042 Cm^{-2} respectively [1]. The spontaneous polarization of BGaN has not been established due to the difficulty of growing high quality layers. As we will only use very small amounts of B in our designs, typically less than 3%, we will use the P_{sp} coefficient of GaN for any composition of BGaN. The calculation of P_{sp} values for the other ternary materials will be

explained later.

Piezoelectric polarization (P_z) is generated by compressive or tensile strain that can form when lattice mismatch occurs during growth of heterostructures and is calculated as shown in Equation 3:

$$P_z = 2\left(\frac{a_{GaN} - a_o}{a_o}\right)\left(e_{13} - e_{33}\frac{c_{13}}{c_{33}}\right) \ [Cm^{-2}]. \quad (3)$$

This equation for strain assumes growth in the ⟨0 0 0 1⟩ direction. The first term of Equation 3 represents the strain of the layer in question. The devices we normally study consist of GaN layers grown on Sapphire substrates. The GaN layer is relaxed; therefore, a_{GaN} represents the lattice constant of GaN which is 3.189 angstroms. The parameter a_o represents the calculated lattice constant of the material layer of concern. For instance, a_o=3.112 angstroms for AlN grown strained onto GaN. The second term in Equation 3 is comprised of piezoelectric constants (e_{13} and e_{33}) and elastic tensor constants (c_{13} and c_{33}). The calculation of the piezoelectric and elastic tensor constants will be explained later. The values of P_z for $In_xGa_{1-x}N$, $Al_xGa_{1-x}N$, and $B_xGa_{1-x}N$ as a function of composition are shown in Figure 2.

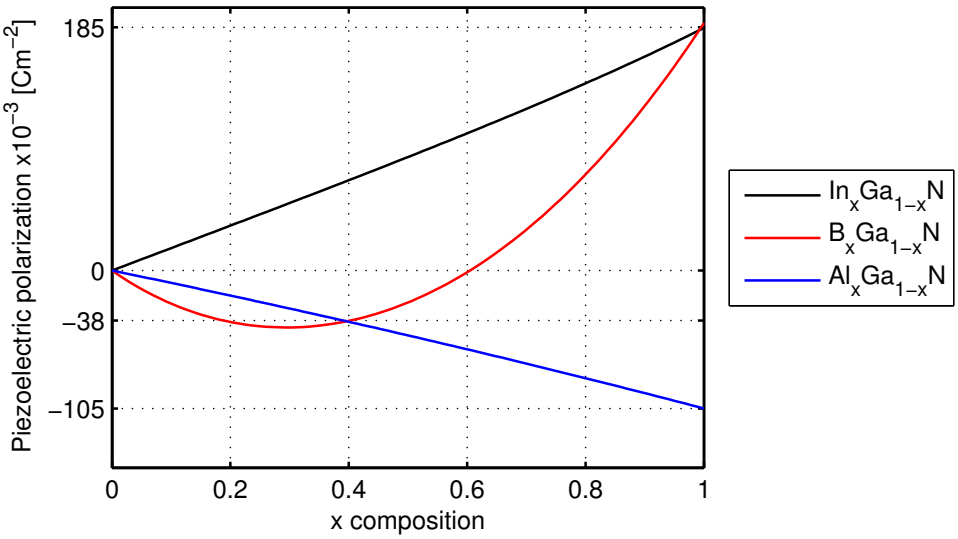

Figure 2: Piezoelectric values for $In_xGa_{1-x}N$, $Al_xGa_{1-x}N$, and $B_xGa_{1-x}N$.

The total polarization for a given III-N material layer is simply the sum of its P_{sp} and P_z values. As can be seen by the units of Equation 3, the calculation results in the formation of sheet charge densities or PCs . Therefore, even though polarization is considered a bulk property, the effects do not appear in the volume of a given epitaxial layer. PCs form on the top and bottom surfaces of the III-N layer, which are of equal magnitude and opposite sign. The sign of the calculated total polarization of a layer and the direction of crystal growth determine whether the top or bottom surface is positively charged. See Figure 3.

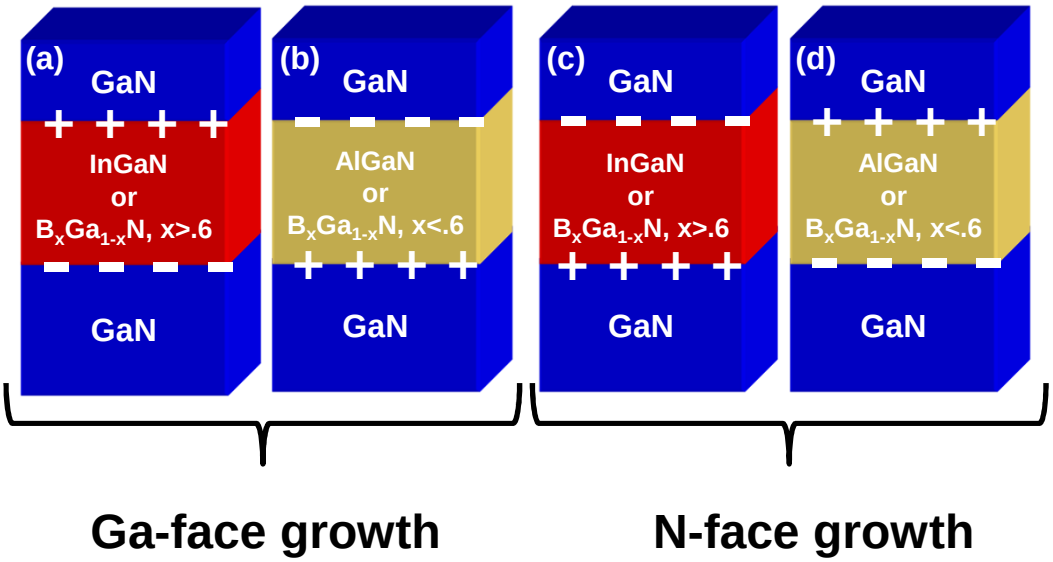

Figure 3: (a,b) Polarization sheet charge polarity for Ga-faced growth. (c,d) Polarization sheet charge polarity for N-faced growth. For InGaN and AlGaN, the sign of the PCs only depends on the direction of crystal growth. The magnitude of the PCs is composition dependent.

The magnitude of the sheet charge density at a given interface is the sum of the polarization values of the layers that form the interface. For Ga-faced crystal growth in the $\langle 0\ 0\ 0\ 1 \rangle$ direction, which is typical in experimental work and will be afterwards assumed, the P_z vectors for InGaN ($0 \leq x \leq 1$) and for BGaN ($0.60 \leq x \leq 1$) point in the $\langle 0\ 0\ 0\ 1 \rangle$ direction or towards the surface as shown in Figure 3(a). This creates a negative charge

density at the interface closest to the substrate and a positive charge density, of equal magnitude, at the interface closest to the surface. The P_z vectors for AlGaN ($0 \leq x \leq 1$) and for BGaN ($0 \leq x \leq 0.60$) layers are oriented along the $\langle 0\ 0\ 0\ \overline{1} \rangle$ direction or towards the GaN substrate. A schematic of this situation is shown in Figure 3(b). N-faced growth simply reverses the overall direction of the polarization charges as seen in Figure 3(c) and Figure 3(d). Finally, it should be noted that PCs are also created when III-Ns interface with non-polar materials, such as the top surface of a device or the GaN/sapphire substrate. However, these PCs are generally passivated by surface states.

The resulting electrostatic properties of these sheet charges are nicely summarized in Ref. [57]. Among the most notable implications, is the fact that the shape of the energy bands becomes a strong function of device geometry. In other words, the thickness and position of the layers are important for creating the desired electrostatic effects such as the formation of electrical fields and quantum gas regions. Therefore, polarization induced effects are not directly linked to any specific doping profile. A device can be designed based on the thicknesses of the layers used. This interesting result will be utilized below in the discussion of InGaN-based solar cells. A second characteristic is that while the electric fields are very large, the largest potential drop of the energy bands is limited by the bandgap of the material involved. Once the bandgap is reached the formation of either a 2DEG or a two-dimensional hole gas (2DHG) will screen the polarization effects to prevent a further drop in potential [58, 59]. This trend is shown in Figure 4. A description of a simple model that predicts the thickness of the strained layer needed to create a potential drop equivalent to the bandgap is described later. Any further increase in thickness results in the conduction and valence bands punching through the Fermi-level to produce the quantum gas regions.

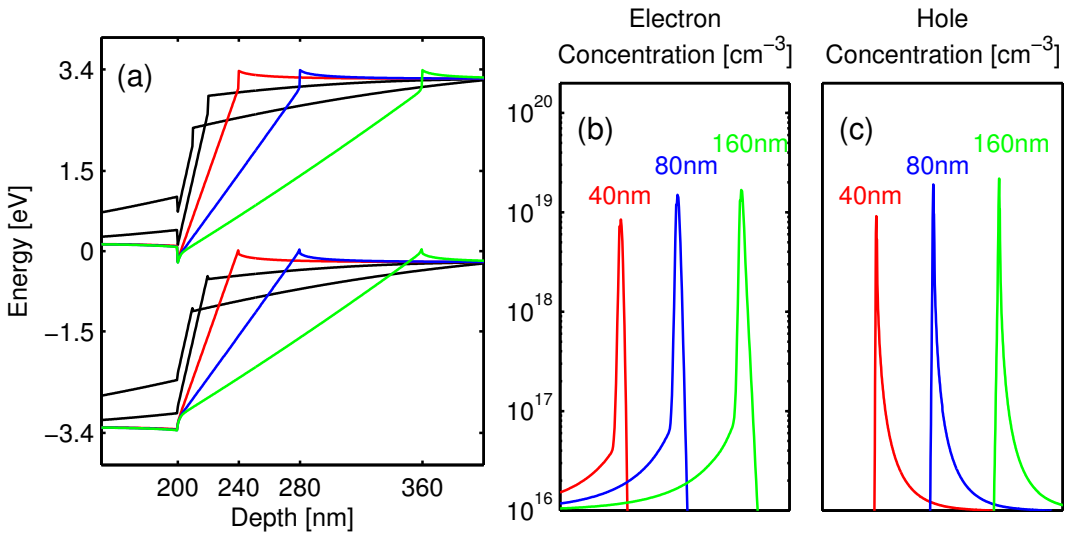

Figure 4: The evolution of energy bands and carrier concentrations in a GaN/ $In_{.1}Ga_{.9}N$/GaN device as a function of $In_{.1}Ga_{.9}N$ thickness. (a) The energy bands for 10, 20, 40, 80 and 160 nm $In_{.1}Ga_{.9}N$ layers. The potential drop is limited to 3.4 eV, the bandgap of the neighboring GaN layers. (b) The formation of 2DEG regions. (c) The formation of 2DHG regions. The 2DEG and 2DHG screen polarization charges and prohibit any further drop in potential.

Polarization sheet charges can be screened by defects, doping and free carriers and therefore are highly dependent on material quality and design [58, 60, 61]. Because these polarization screening mechanisms are growth condition dependent, it is difficult to precisely determine the quantity of polarization effects existing in devices. We introduce a coefficient φ, such that $(0 \leq \varphi \leq 1)$, to indicate the percentage of the theoretical PCs that we are simulating. A value $\varphi = 1$ indicates that the full theoretical value is used, whereas a value of $\varphi = 0$ would indicate that no polarization values are used. The former can be considered a perfect, defect free condition, while the latter would indicate relaxed crystal layers and complete screening through other mechanisms. Intermediate values assume that PCs are only partially screened. Values of φ as high as 0.8 have been demonstrated in experimental work indicating that this is an appropriate method for modeling polarization effects in devices [18].

2.2 Simulation and modeling software

To gain an understanding of the basic physics of semiconductors, our first simulations where programmed with C++ and Matlab. The finite-difference numerical method was implemented [62]. Basic equations for semiconductor physics and statistics are contained in many textbooks [63–65] and will not all be outlined here. Our first objective was to model an AlGaAs/GaAs MODFET device to obtain conduction band and electron concentration profiles. The one-dimensional, time-independent Schrodinger equation was used and is shown here in Equation 4:

$$\frac{-\hbar^2}{2}\frac{d}{dx}\left(\frac{1}{m^*(x)}\frac{d}{dx}\right)\psi + V(x)\psi = E\psi, \tag{4}$$

where $\hbar$ is the reduced Planck constant. The values of m^*, the effective mass of an electron, and V, the electrostatic potential, are used to solve for the wave functions, ψ, and the energy of the system, E. This is an eigenvalue problem that gives the bound energy levels of the system and can be used to obtain the electron density $n(x)$. The details of this procedure are outlined in Ref. [66]. The information of the electron density as a function of the spatial coordinate x is used along with the doping profile, $N_D(x)$ to solve Poisson's equation shown here:

$$\frac{d}{dx}\left(\epsilon_s(x)\frac{d}{dx}\right)V(x) = q^2\left(\frac{N_D(x) - n(x)}{\varepsilon_o}\right), \tag{5}$$

where ϵ_s is the static dielectric constant, q is the charge of an electron, and ε_o is the permittivity of free space. A solution to Poisson's equation with the carrier concentration obtained from the Schrodinger equation results in a new value for the electrostatic potential. If the new value of V is identical to the value of V used in the Schrodinger equation than a solution is found. If they are not equal the process is repeated until a user-defined convergence criteria is met.

Unfortunately, this simple iterative procedure is prone to instability problems and can quickly diverge. Newton's method was implemented to provide a faster and more robust

routine to reach convergence. In this method we consider the actual value of the electrostatic potential $V(x)$ to be defined as $V(x) = V_{init} + \delta V$. Where V_{init} is the initial approximation of the potential profile and δV is defined as the error term, or simply the difference between the initial guess and the actual solution. We then assume that the electron concentration, which is a function of V through the Schrodinger equation, can be defined according to Equation 6 shown here:

$$n\{V_{init} + \delta V\} = n\{V_{init}\} + n\{\delta V\}. \tag{6}$$

This permits Equation 5 to be split into two independent parts as seen in Equation 7,

$$\frac{d}{dx}\left(\epsilon_s(x)\frac{d}{dx}\right)V_{init}(x) - q^2\left(\frac{N_D(x) - n(V_{init})}{\varepsilon_o}\right) = -\frac{d}{dx}\left(\epsilon_s(x)\frac{d}{dx}\right)\delta V(x) + q^2\left(\frac{n(\delta V)}{\varepsilon_o}\right), \tag{7}$$

where the left side contains only n as a function of the initial guess, and the right side contains only n as a function of the error term. The left hand side is simply the solution to the Poisson's equation from the initial potential. A nonzero value for the left hand side of Equation 7 indicates that the initial guess is wrong. This nonzero value is used to solve for δV which is added to the initial potential to provide a new initial guess. This process is repeated until δV is considered sufficiently small.

This process was used to implement the AlGaAs/GaAs MODFET described in [66] and shown in Figure 5. The results of this program are indicated in Figure 6. The initial guess for the conduction band is shown in Figure 6(a). The converged solution is illustrated in Figure 6(c). A schottky contact of 0.7 eV was used as the top contact. The electron concentrations of the initial guess and the converged solution are shown in Figure 6(b) and Figure 6(d) respectively.

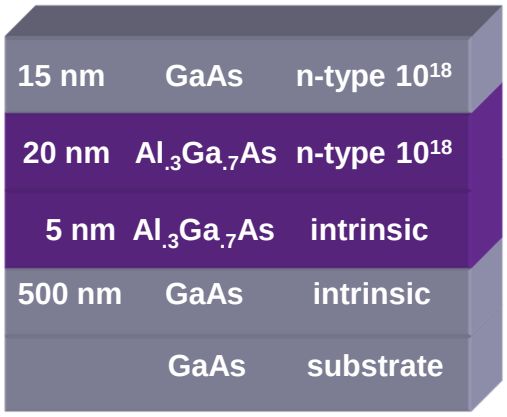

Figure 5: The GaAs/AlGaAs/GaAs MODFET design simulated with in-house software.

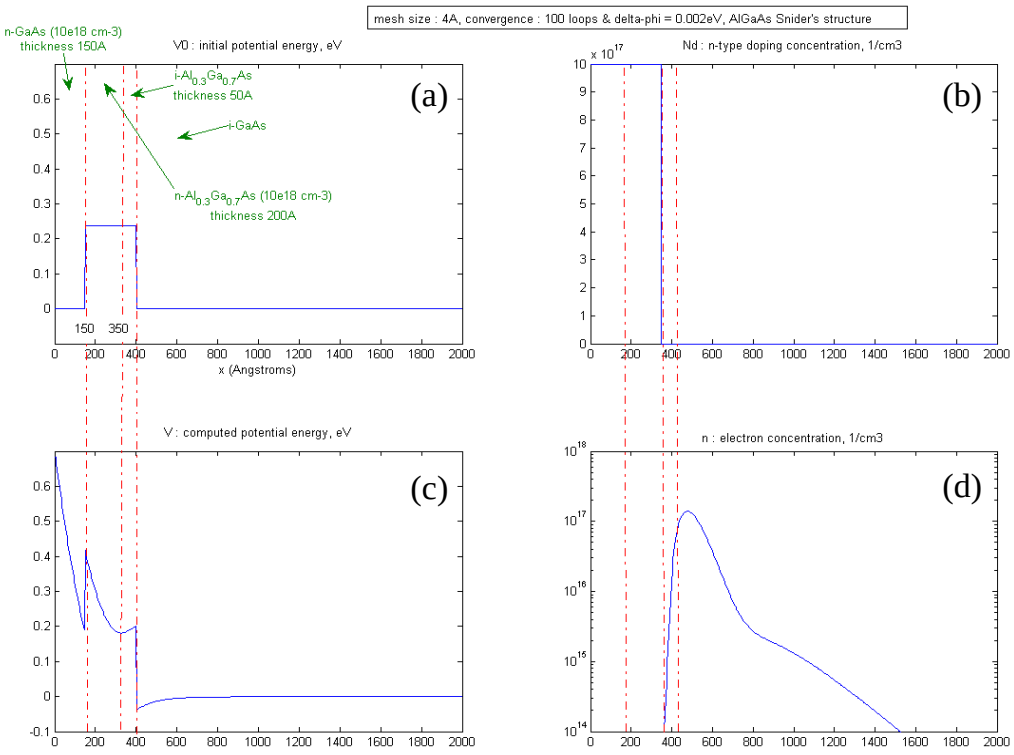

Figure 6: The simulation results of the AlGaAs MODFET design in Figure 5. (a) The initial potential profile. (b) The initial electron concentration profile. (c) The predicted formation of a quantum well in the conduction band. (d) The formation of a 2DEG in the electron concentration profile is clearly evident.

Once a basic understanding of semiconductor physics was reached, it was deemed necessary to switch from in-house simulations to a commercially available software. Commercial semiconductor physics modeling software are able to quickly and accurately predict the energy band profiles for many materials and calculate carrier transport in order to provide I-V curves. Material parameters and many other physics models such as temperature effects on bandgaps, thermal activation of carriers, and quantum effects are integrated into the software alleviating the need to program each component individually. The remaining simulations of device designs are performed using Silvaco's TCAD software [67]. This software solves Poisson's equation, continuity equations and carrier transportation equations using the finite element method. Details of the equations and methods used are found in Ref. [67] and will not be reproduced here. Another reason for selecting the Silvaco TCAD software was that polarization effects in the III-N system can be easily integrated into energy band calculations. Because of the very wide-bandgap of the III-Ns the intrinsic carrier concentration is very low and leads to numerical stability problems for 64 bit calculations. The software can handle 128 bit or 256 bit calculations if the program is run in a Linux environment. Nearly all of the simulations that follows were run using 128 bit precision.

The Silvaco software was used to model all of the devices designed and discussed in Chapter 3. However, it became evident that the software would not be able to calculate the tunneling of the polarization-induced tunnel junctions, which are discussed in length in Chapter 4. This is due to two factors, first the Schrodinger-Poisson solver used to predict the energy bands is not capable of calculating carrier transport. Other quantum models built into the software are not currently compatible with polarization charges. A quantum transport model is of critical importance as the use of strained III-N layers quickly lead to 2DEG and 2DHG regions that necessitate the use of the Schrodinger equation for accurate carrier concentration calculations. Second, Silvaco uses the WKB method to calculate tunneling probabilities. As will be explained in section 4.2 the WKB method is not able

to predict resonant tunneling mechanisms which will be shown to device efficiency. In order to calculate current in PTJ devices, a separate model was implemented in MATLAB. Equilibrium energy band diagrams and information was produced by Silvaco and imported into the MATLAB environment whereupon PTJ tunneling current calculations where performed. This process is the focus of Chapter 4.

2.3 DLTS characterization

Deep-level transient spectroscopy is an efficient experimental method used to detect these defects [68]. DLTS uses high frequency capacitance transient thermal scanning to determine information on trap activation energy, concentration, electron- and hole-capture cross sections, and defect energy levels. These material defects are a primary source of recombination in solar cells as well as a possible screening method of polarization charge effects. Defect states increase recombination rates and degrade device performance. Additionally, these states can screen polarization charge effects. Knowledge of defect densities and their location in the bandgap will improve the modeling of recombination effects which can be very detrimental for solar cells.

The SEMILAB DLTS system, DLS-83D, was used to characterize two samples. This system includes a bath type liquid nitrogen cryostat which will permit low-temperature scans. The hardware is capable of measuring the 10^{-3} pF capacitance transients needed for accurate measurements by using a built in capacitance compensator. Additionally, a lock-in integrator is used to improve the signal to noise ratio. A pulse generator gives a programmable excitation signal with pulse widths of 50 ns to 65 ms and a repetition frequency range of ∼.1 to 2500 Hz. The pulse rise and fall times are less than 25 ns.

One application where an understanding of defects is very important is HEMT sensors. These sensors are comprised of a simple AlGaN / GaN HEMT structure that uses Platinum as a schottky contact. Platinum is a very good catalyst and these devices have been shown to be able to detect NH3, NO, NO2, N2O, CO, CO2, and O2. The sensitivity of these devices are a function of temperature and gate bias. The underlying principle of these devices is that for a particular gas, after reacting with the Pt gate, some of the gas atoms diffuse onto the AlGaN surface. This alters the surface states and changes the conductivity of the sensor. HEMT sensor applications rely on a precise understanding of the concentration of interface states on the AlGaN top layer.

DLTS has been used with AlGaN / GaN HEMT devices to detect interface charges [69].

Normally DLTS is used to detect defects that are at a specific energy level, but spread spacially in the device. These defects are called bulk defects. The surface states are different from normal bulk defect states in that they are localized in space, residing at an interface, and spread out over a range of energies. Therefore a different approach must be taken to analyze these interface states.

The first sample shown here is a simple GaN schottky diode. The capacitance as a function of voltage is shown in Figure 7. As we are using a constant capacitance DLTS measurement, it is necessary to have a relatively constant capacitance for the reverse and pulsed bias range. From Figure 7 it was determined that a reverse bias of -0.75 V would be used with a maximum pulse bias of 0.0 V.

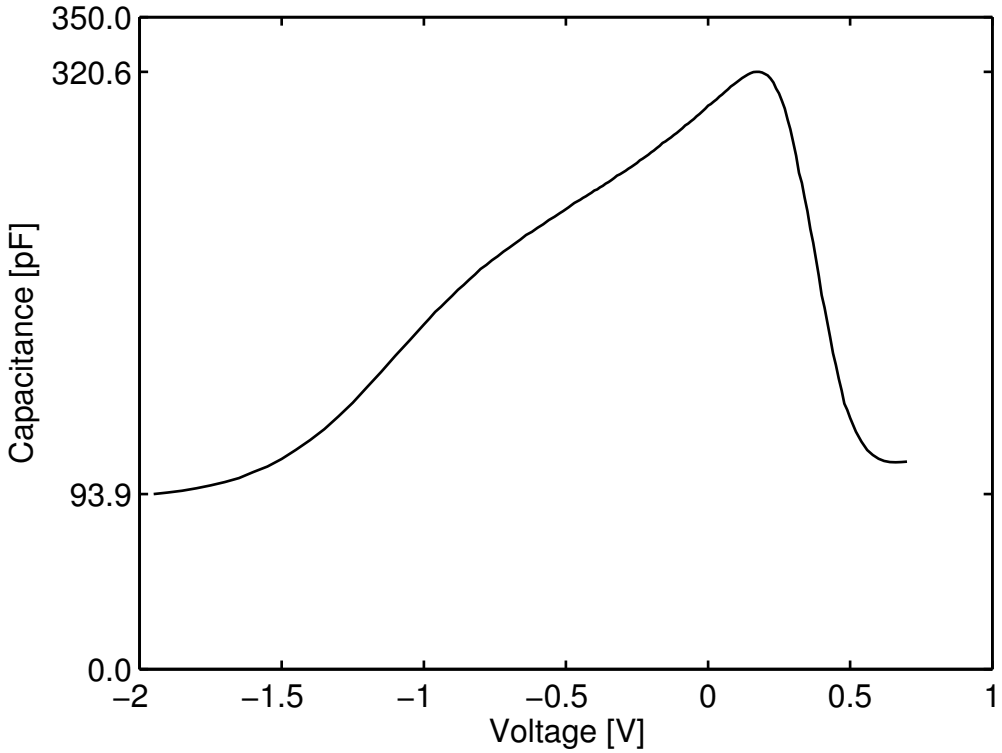

Figure 7: Capacitance as a function of applied bias for a GaN schottky diode.

The pulse frequency was set to 67 Hz with a pulse width of 100 μ s. Three separate runs were performed with a pulse bias value of -0.5, -0.2, and 0.0 V. The resulting DLTS

measurement are shown in Figure 8. The shift in both the maximum peak and shape by simply changing the level of the pulse bias is attributed to interface trap states [2, 70].

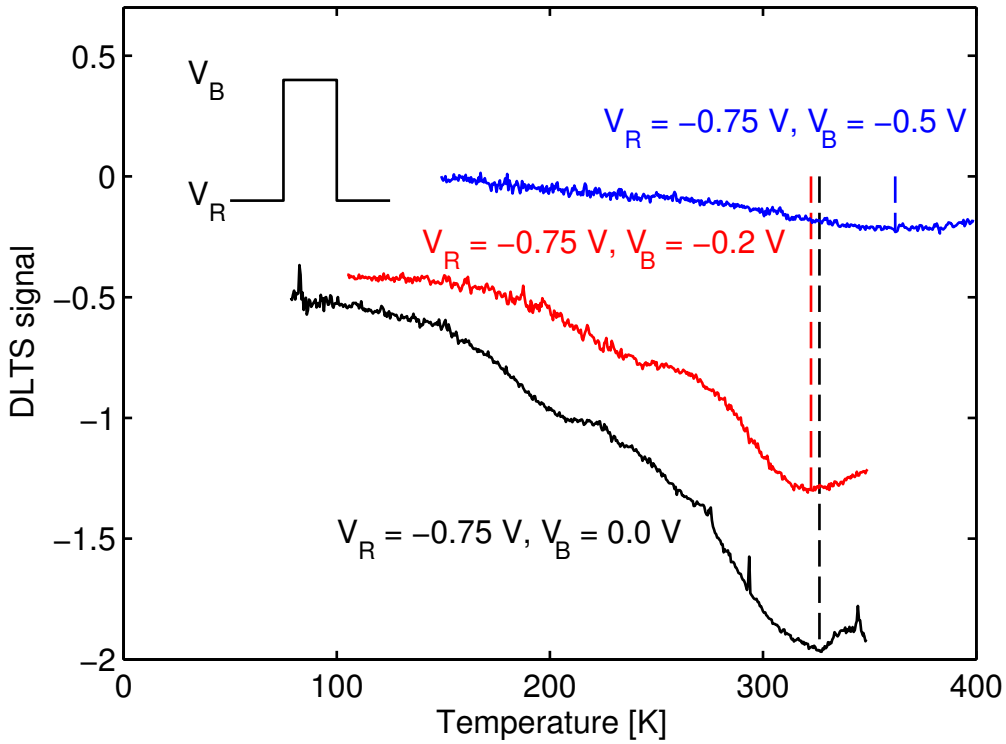

Figure 8: The DLTS signal as a function of temperature for three temperature scans. The shift in the peak and the increase in peak height as a function of bias voltage, for a fixed reverse bias, is attributed to interface trap states [2].

A second sample, also a schottky diode, consisted of a $B_{.0047}Ga_{.9953}N$ top layer. A capacitance scan was performed resulting in Figure 9. The parabolic shape of the capacitance curve corresponds to a metal-insulator-semiconductor (MIS) device. A successful DLTS profile of this device was not possible due to the non-constant nature of the capacitance curve. However, the curve does indicate that the BGaN layer is indeed highly resistive as proposed in Ref. [71].

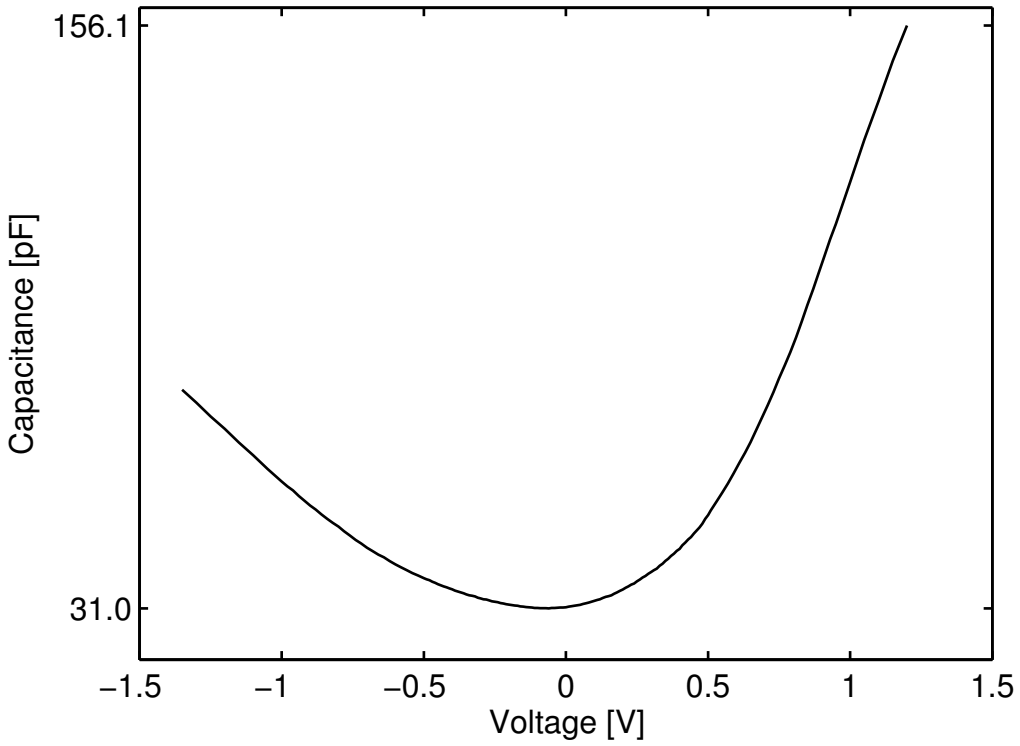

Figure 9: Capacitance as a function of applied bias for an BGaN schottky diode.

CHAPTER 3

POLARIZATION ENGINEERING FOR IMPROVED DEVICE PERFORMANCE

This chapter deals primarily with the impact, both positive and negative, of PCs on the energy bands of designs. The first section deals with using polarization to increase the carrier confinement in HEMT structures. The next section discusses the application of PCs in InGaN devices and shows that the charge separation regions can be created nearly independently from doping schemes. This leads to very robust designs. Finally the last section deals with polarization implications for semi-bulk InGaN.

3.1 HEMT Devices

The first focus of research was conducted on AlGaN/GaN HEMTs. The remainder of this section is taken from our paper published in *The European Physical Journal - Applied Physics* [55]. Current AlGaN/GaN HEMTs have resulted in a record-high current gain cutoff frequency of 300 GHz with an extrinsic transconductance of 530 mS mm^{-1} [72]. To increase the frequency performance of these HEMTs, there is a need to reduce the gate length. Unfortunately, a reduction of the gate length leads to short channel effects such as soft pinch-off and increased output resistance. These negative short channel effects can be offset by increasing carrier confinement in the channel region [72]. In conventional $Al_yGa_{1-y}N$/GaN HEMTs, bulk GaN is used to form the buffer as well as the electron carrier channel while $Al_yGa_{1-y}N$ is used as a front-barrier, as represented in Figure 10. The strong PCs present in the AlGaN material system forms a quantum well dipping below the Fermi level, which confines a 2DEG at the $Al_yGa_{1-y}N$/GaN interface [33].

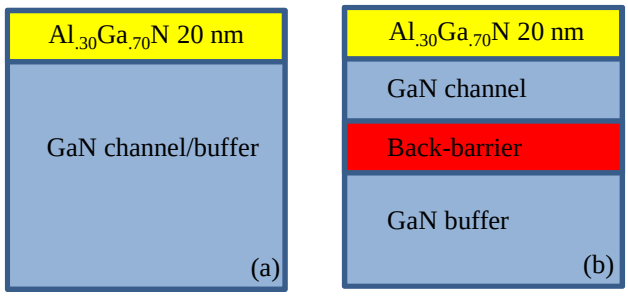

Figure 10: The general structure of HEMT designs. (a) A Standard AlGaN/GaN design. (b) An AlGaN/GaN design with a back-barrier region to improve 2DEG carrier confinement. The channel thickness is defined as the thickness of the GaN layer between the AlGaN front-barrier and the back-barrier.

Despite the high carrier confinement between the channel and the gate in III-N HEMTs, there exists a problem with electrons being excited into the buffer layer from the channel region. Several methods have been researched to eliminate this buffer current leakage; for example, compensation with dopants such as iron and carbon [73, 74], wide-bandgap insulators such as AlN [75], and through double-heterojunction structures [76–79]. These methods were unsuccessful for high voltage and frequency operation as they introduced deep-level traps in the buffer region [80, 81].

Another approach is to insert a strained back-barrier layer such as $Al_xGa_{1-x}N$ [82–84] or $In_xGa_{1-x}N$, see Figure 10(b), that utilize the polarization effects of III-N materials to create an electrostatic potential to carriers [3, 72, 85, 86]. In-house simulations were run for both the AlGaN and InGaN back-barrier designs. The conduction band profile for an $Al_yGa_{1-y}N/GaN/Al_xGa_{1-x}N/GaN$ back-barrier device are shown in Figure 11. Here it can be seen that the $GaN/Al_xGa_{1-x}N$ interfaces forms a negative sheet charge and creates a potential barrier for electrons. The $Al_yGa_{1-y}N/GaN$ and $Al_xGa_{1-x}N/GaN$ interfaces form positive sheet charge densities that create quantum wells (QWs). The electron concentration in the QW at the $Al_xGa_{1-x}N/GaN$ in Figure 11 is an order of magnitude smaller than the primary QW. However, the carrier concentration of this secondary QW become larger

than that of the primary QW for thick back-barrier layers or high aluminum content. In fact, as indicated in Ref. [87], a 10 nm thick $Al_{.15}Ga_{.85}N$ back-barrier layer reduced the primary $Al_{.3}Ga_{.7}N$/GaN interface 2DEG concentration to $5x10^{18}$ cm^{-3} and created a secondary 2DEG concentration of $2x10^{19}$ cm^{-3} at the back-barrier / buffer interface.

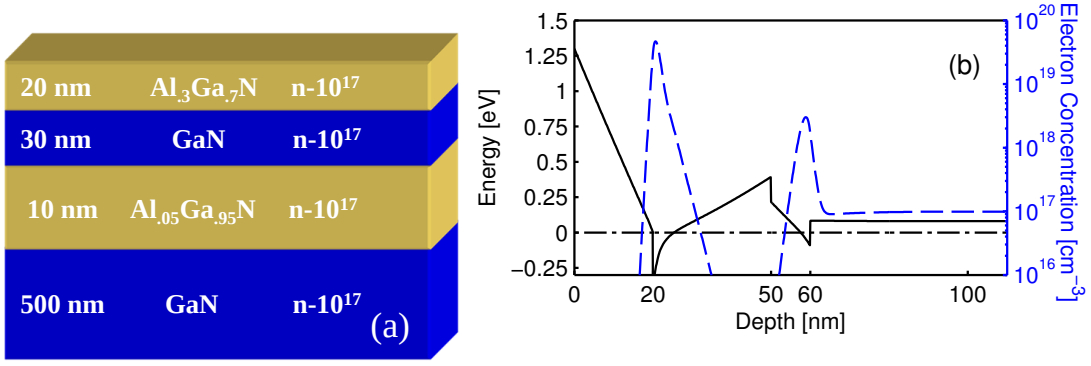

Figure 11: (a) $Al_{.3}Ga_{.7}N$/GaN/$Al_{.05}Ga_{.95}N$/GaN HEMT design. (b) Conduction band and electron concentration profile. The PCs of the $Al_{.05}Ga_{.95}N$ back-barrier introduce an electrostatic barrier to electrons in the primary 2DEG and a secondary quantum well at the $Al_{.05}Ga_{.95}N$/GaN interface.

The polarization fields are reversed in the InGaN back-barrier designs as noted in Ref. [3] and reproduced here in Figure 12. The PCs of the InGaN back-barrier form a QW at the GaN/InGaN interface and an electrostatic barrier at the InGaN/GaN interface.

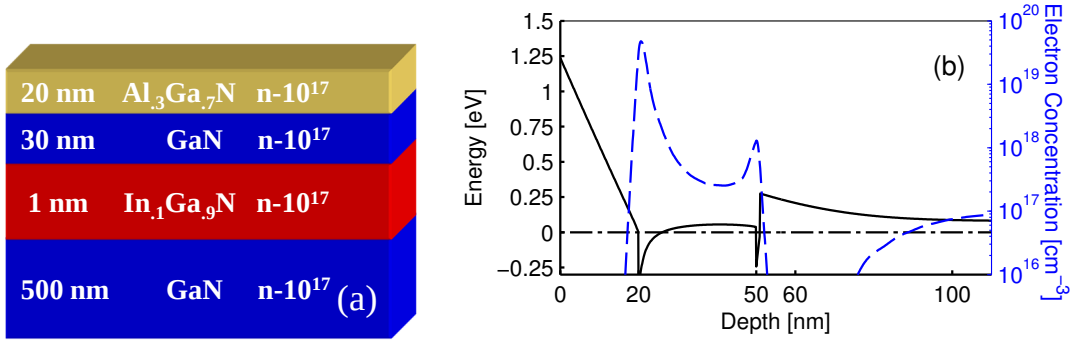

Figure 12: (a) $Al_{.3}Ga_{.7}N$/GaN/$In_{.1}Ga_{.9}N$/GaN taken from [3]. (b) Conduction band and electron concentration profile. The PCs of the $In_{.1}Ga_{.9}N$ back-barrier introduce an electrostatic barrier to electrons at the $In_{.1}Ga_{.9}N$/GaN interface. A smaller secondary quantum well is created at the GaN/$In_{.1}Ga_{.9}N$ interface.

In one of our group's first studies of HEMT structures, we investigated the use of BGaN as a back-barrier [4]. It was shown previously by our group that BGaN is highly resistive with only a few percent of boron (<5%) [71]. This increased resistance was expected to help increase the confinement of the 2DEG electrons to the AlGaN/GaN interface. Several HEMT samples were grown with a 1.0 nm thick $B_{.01}Ga_{.99}N$ layer inserted 40 nm below the $Al_{.3}Ga_{.7}N$/GaN interface. These structures where compared to those without the BGaN back-barrier grown under the same conditions. Hall measurements for the BGaN back-barrier devices indicated a 2DEG carrier sheet density of $1.0x10^{13}$ cm^{-2} and a carrier mobility of 1230 $cm^2V^{-1}s^{-1}$. The back-barrier free device exhibited lower values of $7.5x10^{12}$ cm^{-2} for the carrier sheet density and a carrier mobility of 906 $cm^2V^{-1}s^{-1}$. This indicated that the BGaN back-barrier improved the device performance. However, as shown in Figure 13, simulations of the polarization effects indicate that a 1 nm thick $B_{.01}Ga_{.99}N$ layer provides an insignificant potential barrier of less than 0.05 eV. Therefore the improved performance of the device is attributed to the resistivity of the BGaN region or possibly through decreasing the residual doping of oxygen in the AlGaN barrier layer [88].

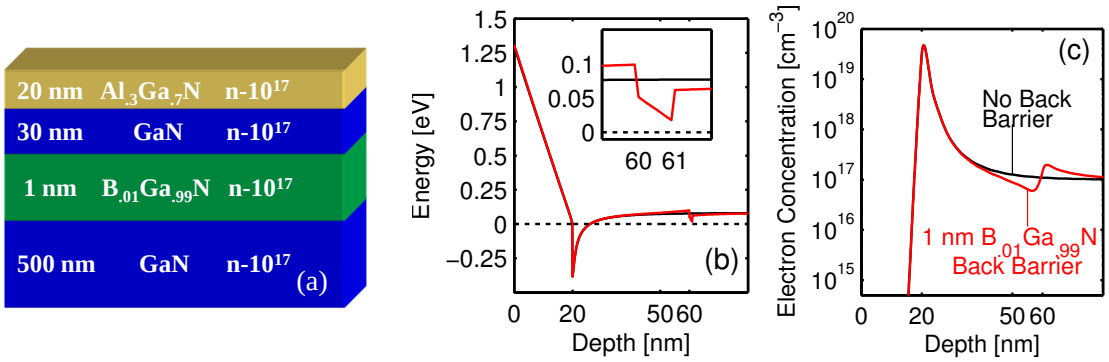

Figure 13: (a) $Al_{.3}Ga_{.7}N$/GaN/$B_{.01}Ga_{.99}N$/GaN taken from [4]. (b) The conduction band profile. (c) The electron concentration profile. The small electrostatic barrier created by polarization effects in the back-barrier layer are shown in the inset of the conduction band profile.

Because BGaN is a new material system and Ref. [4] is the first active device made using BGaN we investigated possible designs focusing on the polarization properties of BGaN. We showed that an electrostatic barrier is created at the GaN/BGaN interface similar

to the AlGaN back-barrier case. Our design restricted boron content to a maximum of 2%, which was similar to our use of boron content of 1% that improved HEMT performance [4], but less than our demonstrated 3.6% content [89].

Our study researched the effects of variations in the channel thickness and back-barrier thickness. Our first set of simulations varied the channel thickness from 10 to 50 nm while the barrier thickness was held to 20 nm. Figure 14 shows the dependence of the peak carrier concentration of the 2DEG versus channel thickness. Two important effects can be seen in Figure 14. First, in all cases the peak carrier concentration will be within 8.2% of that of an AlGaN/GaN HEMT without a back-barrier, the worst case being the 10 nm channel with 2% B. Second, the further the back-barrier is from the interface, the higher the 2DEG concentration. For a 30 nm channel thickness the carrier concentration is within 3% of the maximum value for all three compositions simulated.

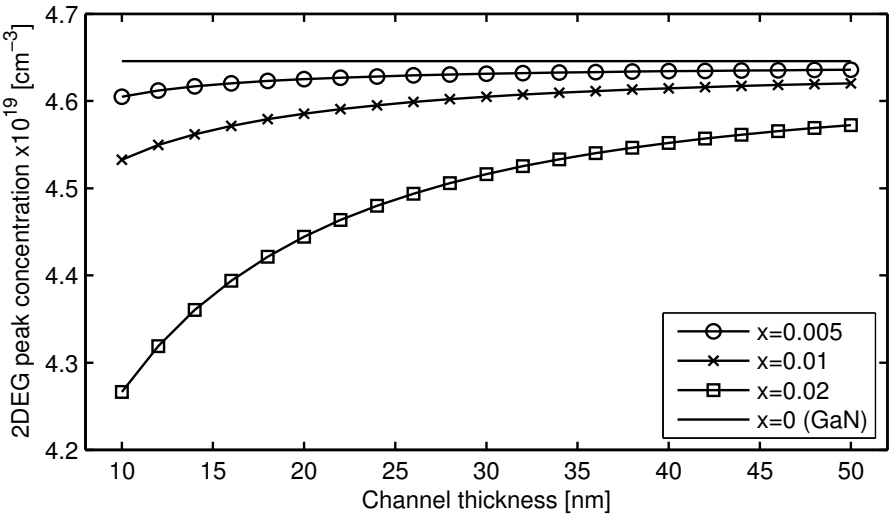

Figure 14: Peak carrier concentration as a function of channel thickness using a 20 nm back-barrier for $B_xGa_{1-x}N$ with x=0.0, 0.5, 1.0, and 2.0 percent.

The next gamut of simulations was used to study the effect of back-barrier thickness. The channel width was set to 30 nm and the thickness of the barrier was scanned from 2 to 50 nm. The change in the peak carrier concentration in the 2DEG for these cases is shown in Figure 15. For a 30 nm channel thickness, back barriers have only a slight effect on the

peak concentration in the AlGaN/GaN channel. The worst case for this set of simulations is a 6% drop for the 50 nm $B_{.02}Ga_{.98}N$ layer.

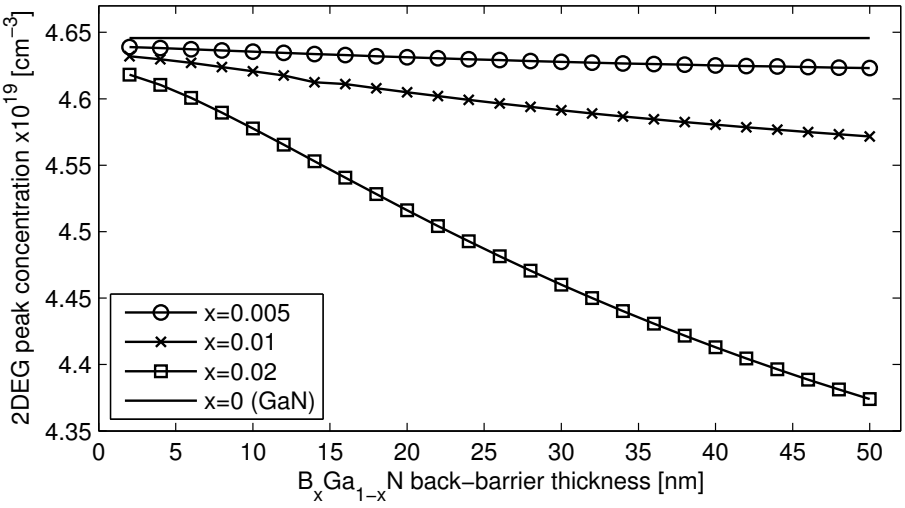

Figure 15: Peak carrier concentration as a function of back-barrier thickness using a 30 nm channel for $B_xGa_{1-x}N$ with $x = 0.5$, 1.0, and 2.0.

The conduction band evolution for both changes in the channel and in the back-barrier thickness can be visualized in Figure 16 and Figure 17. The electrostatic barrier peak increases with higher boron content and, more importantly, with thicker back-barrier layers. The saturation and overshoot velocity for GaN are around $3x10^7$ cm s^{-1} [9]. An electron with this velocity has about 0.26 eV of kinetic energy. With this consideration in mind, our objective is to create a barrier that is at least 0.26 eV above the conduction band and thick enough to prevent carriers from tunneling through. Table 2 indicates the compositions that have a barrier height of 0.25 eV and 0.50 eV and barrier thickness of at least 10 nm.

Table 2: Thickness of the BGaN back-barrier needed to form either a 0.25 or 0.5 eV barrier at least 10 nm wide. The channel thickness is fixed at 30 nm.

Energy (eV)	$B_{.005}Ga_{.995}N$ (nm)	$B_{.01}Ga_{.99}N$ (nm)	$B_{.02}Ga_{.98}N$ (nm)
0.25	36	14	6
0.50	Not reached	42	16

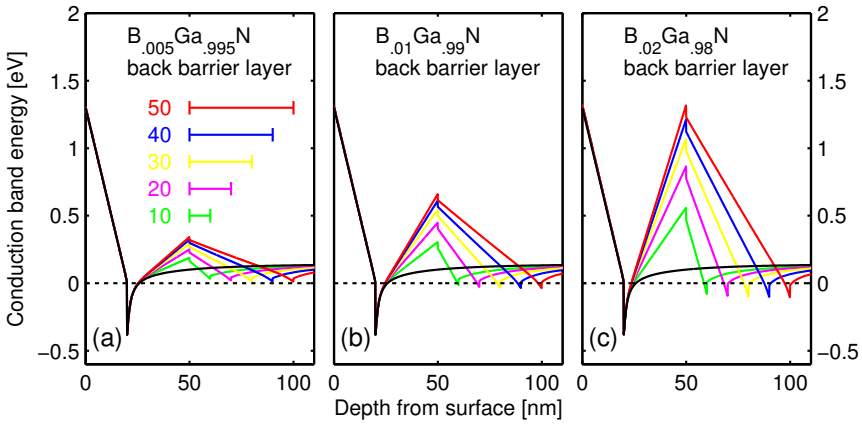

Figure 16: (a) $B_{.005}Ga_{.995}N$ back barrier designs. (b) $B_{.01}Ga_{.99}N$ back barrier designs. (c) $B_{.02}Ga_{.98}N$ back barrier designs. The evolution of the conduction band as a function of back-barrier thickness and boron content is shown in each figure. The channel thickness is fixed at 30 nm while the back-barrier thickness is increased from 10 to 50 nm in 10 nm steps. Each color represents the conduction band for a particular design. The location and thickness, in nm, of the back barrier is indicated in (a) and is the same for (b) and (c). The black curve is the conduction band for a simple AlGaN/GaN HEMT.

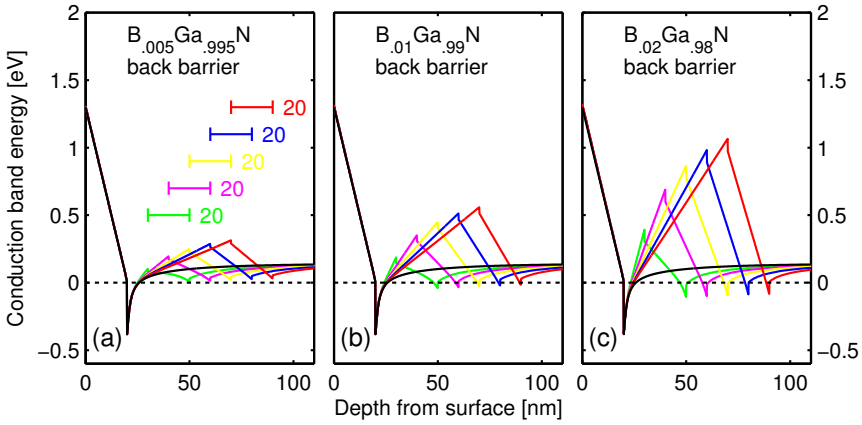

Figure 17: (a) $B_{.005}Ga_{.995}N$ back barrier designs. (b) $B_{.01}Ga_{.99}N$ back barrier designs. (c) $B_{.02}Ga_{.98}N$ back barrier designs. The evolution of the conduction band as a function of channel thickness and boron content is shown in each figure. The back-barrier thickness is fixed to 20 nm while the channel thickness is increased from 10 to 50 nm in 10 nm steps. Each color represents the conduction band for a particular design. The location and thickness, in nm, of the back barrier is indicated in (a) and is the same for (b) and (c). The black curve is the conduction band for a simple AlGaN/GaN HEMT.

In summary, we find that the peak carrier concentration in the 2DEG region decreases for increased B percentages, for increased back-barrier thickness and for decreased channel width. The electrostatic barrier increases for higher B percentages and for thicker back-barriers. Both a sufficiently high electrostatic barrier and high carrier concentrations are needed to achieve good device performance.

A good design should also take into account a few growth concerns as high B incorporation poses challenges. Additionally, high levels of strain lead to defect formations, which can degrade performance. From these considerations the use of a lower B concentration is attractive. With this information we now optimize the BGaN back-barrier design. An optimized channel thickness of 30 nm should provide an adequate buffer to prevent any B impurities from decreasing electron mobility by diffusing into the channel region. $B_{.01}Ga_{.99}N$ was selected as the composition of choice as it has smaller effects on the carrier concentration, yet it is still able to provide an adequate barrier. Our optimal design will use a 30 nm channel with a 50 nm $B_{.01}Ga_{.99}N$ layer. This provides a 15 nm electrostatic barrier at 0.5 eV and should only decrease the 2DEG by 1.6% compared to a HEMT with no back-barrier.

The BGaN back-barrier design is compared to a simple AlGaN/GaN HEMT in Figure 18. While the conduction band profile indicates the strong back-barrier created, the carrier concentration profile helps to better show the effects of the design on electrons. For normal AlGaN/GaN HEMTs the carrier concentration is as high as $5x10^{16}$ cm^{-3} for 28 nm after the AlGaN/GaN interface. However, for our optimized design the carrier concentration drops below $6x10^{15}$ cm^{-3} at less than 9 nm. This suggests that carriers are strongly confined to the AlGaN/GaN interface. The secondary quantum well created by the BGaN back-barrier is located 80 nm from the AlGaN/GaN interface and has a peak carrier concentration of $1.9x10^{18}$ cm^{-3}. This channel could be pushed further from the 2DEG region with increased back-barrier thickness or decreased by using a graded BGaN at the back end of the barrier.

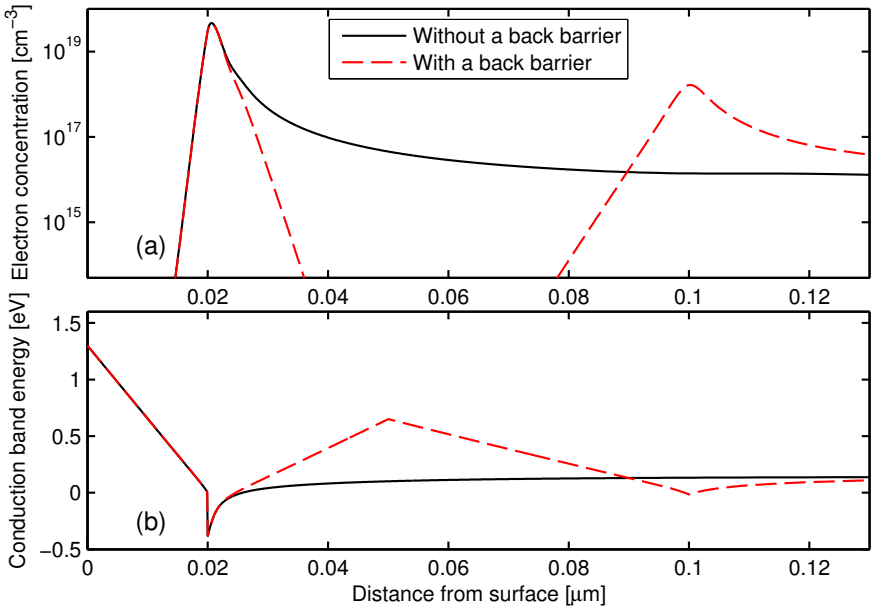

Figure 18: Comparison of conduction band and electron concentrations for optimized BGaN design versus normal HEMT design.

If the growth of thick BGaN layers proves experimentally difficult, it is possible to use a superlattice approach. For instance, if only 5 nm layers of $B_{.02}Ga_{.98}N$ can be epitaxially strained before relaxation occurs it would be important to investigate other designs. Five layers of 5 nm $B_{.02}Ga_{.98}N$/5 nm GaN produce similar results. See Figure 19.

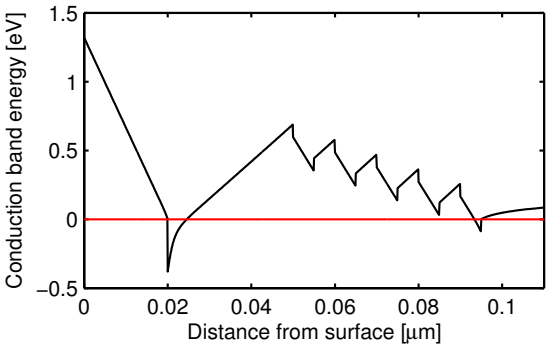

Figure 19: Conduction back for five periods of 5 nm/5 nm $B_{.02}Ga_{.98}N$/GaN layers with a 30 nm channel thickness.

This concluded our study of AlGaN/GaN/BGaN/GaN HEMT structures. The study indicates that BGaN back-barriers are advantageous because carriers are tightly confined to the higher mobility GaN channel region. Simulations show that electrons can be confined to within 17 nm of the AlGaN/GaN interface using a 50 nm $B_{.01}Ga_{.99}N$ back-barrier and a GaN channel width of 30 nm. It was shown that MQW designs are possible that would allow for thinner interlayers of BGaN to be used to help alleviate growth issues if thicker layers prove difficult to grow. This design confines carriers to a region comparable to that of the current state-of-the-art InGaN back-barrier design [90, 91]. As the carriers are confined to be within about 17 nm of the AlGaN/GaN interface for a back-barrier that is 30 nm away, BGaN is expected to introduce relatively few traps into the 2DEG region. The use of BGaN back-barriers should allow for shorter gate lengths and therefore improved high-frequency performance. Target system applications include satellite communications and high-performance radars as well as other RF and microwave systems.

3.2 Robust Solar Cells

Polarization charges can aid in the design of InGaN solar cells in order to make robust and efficient devices. The following two sections are comprised of work taken from three published papers. First, a conference paper describing the adverse effects of polarization on conventional p-i-n solar cell designs [92] was published in *IEEE, 2012 12th International Conference on Numerical Simulation of Optoelectronic Devices (NUSOD)* Second, a follow up paper that describes the effects of polarization on semibulk InGaN layers has been published in *Optical and Quantum Electronics* [93]. Third, a paper accepted for publication by *IEEE Electron Device Letters* details the possible use of polarization to alleviate the need for heavily doped n- or p-type regions [94].

Solar cells using a GaN/InGaN/GaN layer configuration have historically been created with a p-i-n design. A p-i-n configuration has an n-type layer as the substrate and a p-type top layer, which is referred to as the window layer. Pin structure solar cells often provide improved performance over n-i-p devices because acceptors are easier to activate when the p-type layer is close to the surface. Additionally, the minority carrier diffusion length of electrons is generally larger than that of holes, which would allow for more carriers absorbed in the window layer to successfully transport to the contacts of the solar cell [95]. Due to the low levels of p-type doping, pin devices require thick p-doped layers to create an effective space-charge region [36] which lowers quantum efficiency by increasing the distance minority carriers must travel to reach contacts [37,41]. However, for InGaN layers strained on GaN, the polarization induced electric field creates a barrier for photocurrent that impedes device performance as seen in Ref. [27] and reproduced here in Figure 20. The p-type regions was doped at $5x10^{17}$ cm^{-3} while the doping in n-type regions was 10^{18} cm^{-3}. The InGaN region was doped at 10^{16} cm^{-3} n-type.

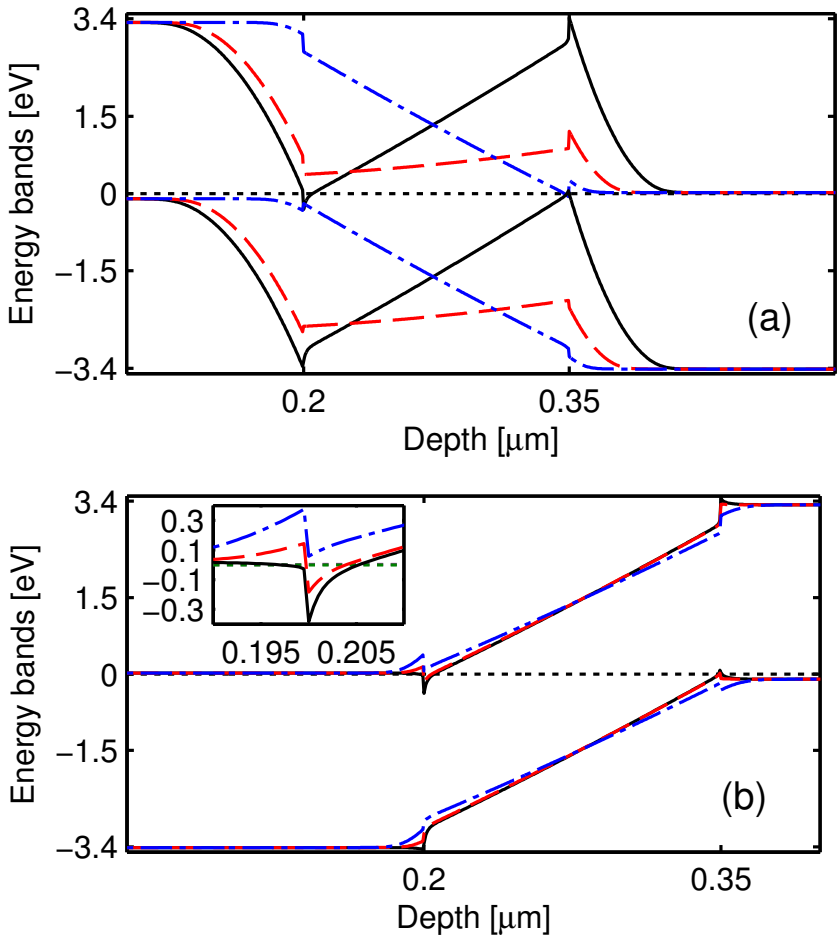

Figure 20: Energy band profiles for InGaN-based solar cells. (a) Pin devices. (b) Nip devices. Blue dot-dashed lines are for $\varphi = 0.0$, red dashed lines are for $\varphi = 0.25$ and black solid lines are for $\varphi = 1.0$. Pin devices are not expected to have good efficiency for high PCs as the photo-generated carriers in the InGaN region flow in the wrong direction. Nip device energy band profiles are nearly invariant with any amount of PCs.

In InGaN solar cells, it beneficial to have coherently strained layers as this reduces dislocations and has been shown to improve device quality [37]. The PCs of strained GaN/InGaN/GaN layers can create large polarization electric fields. Experimental results have shown these electric fields to be around 2.45 MVcm^{-1} with just 18% indium [44]. Thus, as seen in Figure 20, the use of only 25% of the theoretical maximum number of PCs has drastic effects on the band diagram, reversing the direction of the photo-generated current inside the absorption layer. As material quality improves the effect is likely to become more substantial and could severely lower the efficiency of solar cells used in the

p-i-n configuration. It should be noted that for GaN/InGaN/GaN devices, the piezoelectric polarization is the dominant polarization term and is around 20 times larger than the spontaneous polarization. For example at an $In_{.1}Ga_{.9}N$ interface, the total P_z value is 17.1 mCm^{-2} while the total P_{sp} value is 0.8 mCm^{-2}. Therefore, if the material is not coherently strained, the spontaneous polarization is negligible and not expected to affect device performance.

Because the strength of electric fields created by PCs can be larger than those created by p-n junctions, it is important that they align. A summary of the four possible configurations for a solar cell are indicated in Figure 21. Only the configurations of n-i-p for Ga-faced growth and p-i-n for N-faced growth led to an alignment of the electric fields. Our work studied the n-i-p configuration for Ga-faced growth; a study of the p-i-n configurations on N-face substrates was reported in [28].

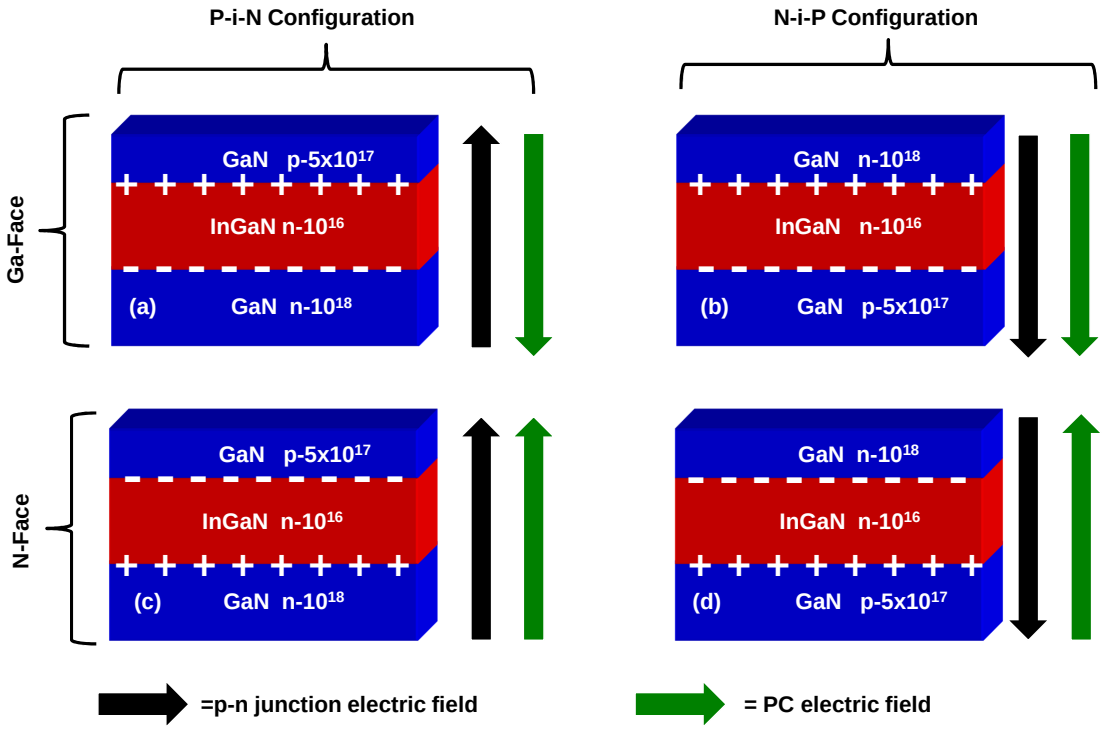

Figure 21: Possible design configurations of InGaN solar cells. (a,c) Pin devices. (b,d) Nip devices. The electric fields from PCs and p-n junctions only align with n-i-p for Ga-faced growth and p-i-n for N-faced growth configurations.

For the n-i-p on Ga-face configuration any polarization charges at the interfaces contribute to a drop in the potential of the conduction band from the i-p interface to the n-i interface. Band diagrams for three different values of φ are shown in Figure 22. The band diagram is only slightly modified for up to 100% of the theoretically predicted polarization. This indicates that with improved material quality, the natural polarization of the InGaN layer will assist rather than detract from the photo-generated current. After the potential drop is equal to the bandgap $E_g(x)$ of the intrinsic layer, the conduction and valence bands punch through the Fermi level, which induces self-screening [18]. This self-screening creates 2DEG and 2DHG regions that partially neutralize the polarization charge density and prevent any further drop in the potential [59]. This is evident in the blue and black curves of Figure 22(b) and Figure 22(c), which show the formation of a 2DEG and a 2DHG at the heterointerfaces.

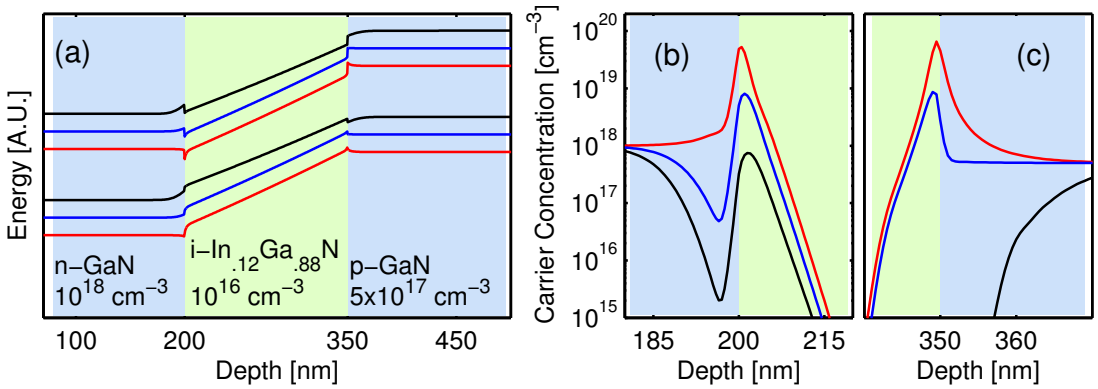

Figure 22: (a) Conduction and valence bands for an n-i-p device. The curves are separated on the vertical scale to facilitate comparison. (b) Electron concentrations showing 2DEG forming near the n-GaN/i-InGaN interface. (c) Hole concentrations showing 2DHG forming at the i-InGaN/p-GaN interface. For all figures, a black curve is for $\varphi = 0$; a blue curve is for $\varphi = 0.25$, and a red curve is for $\varphi = 1.0$.

We have systematically searched the n-i-p design space for variations of several parameters: φ from 0.0 to 1.0, n-layer thickness from 10 to 300 nm, p-layer thicknesses from 10 to 200 nm, n-layer doping from 10^{15} to 10^{18} cm^{-3} and p-layer doping from 10^{10} to 5x10^{17} cm^{-3}. Thicker n-type window layers lower J_{sc} in all cases simply by inefficiently absorbing higher energy photons. A 20 nm window layer has an AM0 (AM1.5) photocurrent

160% (129%) of that of a 200 nm-thick window layer design. For further comparison, we select a window layer thickness of 20 nm and doping level 10^{16} cm^{-3}, select 150 nm thick $In_{.12}Ga_{.88}N$ layer unintentionally doped at 10^{16} cm^{-3}, and examine this reduced design space for φ, p-doping, and p-layer thickness. This results in V_{oc} = 2.27 V, J_{sc} = 2.15 $mAcm^{-2}$, and a fill factor of 90.0%, values in agreement to two decimal places for the whole scanned design space when $\varphi \geq 0.2$. On the other hand when $\varphi = 0$, this n-doping is insufficient to effectively form a space-charge region [36]: a 200 nm p-layer doped to 5x10^{17} cm^{-3} results in V_{oc} = 4 mV and J_{sc} = 0.08 $mAcm^{-2}$. Thus the high V_{oc}, J_{sc}, and fill factor of these solar cells are almost entirely a result of the polarization induced field and are independent of both the n and p layer doping levels used.

We have performed 1-D simulations, which distinguish the charge separation process and transport normal to interfaces from lateral transport to contacts. In the regime where electrostatics are determined by PCs, the 2DEG and 2DHG contribute significantly to lateral transport to the contacts. The predicted carrier concentrations of ~10^{19} cm^{-3} in the region of the heterointerfaces imply that lateral transport is assisted by the 2DEG and 2DHG, facilitating thin n- and p-layers. The mobility of an AlGaN/InGaN 2DEG was experimentally found to be 730 $cm^2V^{-1}s^{-1}$ [96]. Assuming an average carrier concentration of 2x10^{19} cm^{-3}, a sheet resistance of 712 ohms was calculated for a 6 nm 2DEG channel. A 50nm window layer of 10^{18} cm^{-3} gives a sheet resistance of 4160 ohms, assuming an electron mobility of 300 $cm^2V^{-1}s^{-1}$. Thus the 2DEG has a lateral resistance equivalent to that of 350 nm of material doped to 10^{18} cm^{-3} without the lowered efficiency that such a capping layer would cause.

By modeling the charge densities at the interfaces as a parallel-plate capacitance $C = \varepsilon A/d = Q/V$, we can calculate d_{min}. Setting $V = E_g$ and setting the total polarization charge P_t to $P_t = \varphi Q/A$, we obtain $d_{min} = \left(\varepsilon(x)E_g(x)\right)/P_t(x)$, where ε is the the static dielectric permittivity of the intrinsic region. For indium content x, where $0 < x \leq 0.5$, one may approximate $d_{min}(x)$ in nanometers by $d_{min} \simeq 203x + 150\varphi x(58x + 111)$.

The solid curves in Figure 23 are from the exact expression for d_{min} for $\varphi = 0.2$, $\varphi = 0.5$, and $\varphi = 1.0$. A suite of simulations was used to determine the importance of doping of the n and p layers on the minimum i-region thickness needed to maximize the built-in voltage (V_{bi}) across the intrinsic region. The results of a low doping scheme, with $n=10^{16}$ and $p=10^{16}$ cm^{-3} are shown as the circles in Figure 23, while a typical doping scheme of $n=10^{18}$ and $p=5x10^{17}$ cm^{-3} are indicated with triangles. Figure 23 shows that d_{min} is a reasonable guide for predicting the attainment of maximum V_{bi} by means of polarization charges. We also report that further increase of the thickness of the i-region by 5-10 nm results in the creation of a 2DEG and a 2DHG for $x > 0.1$ and $\varphi \geq 0.5$ or for $x > 0.15$ and $\varphi \geq 0.2$. The usefulness of the analytic approximation for predicting which experimental regimes are dominated by polarization charges can be seen in Figure 23. Beyond d_{min}, the formation of the V_{bi} is indeed largely independent of doping levels in either the n- or p-type layers. It should be noted that most absorption regions are larger than 100 nm. Therefore, polarization effects are expected to be significant for strained InGaN layers.

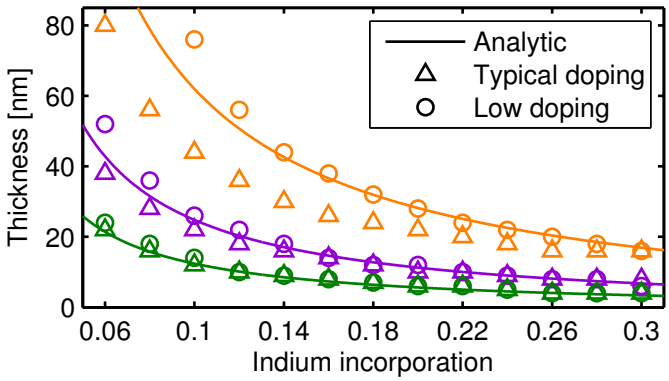

Figure 23: Minimum InGaN layer thickness d vs. indium content for potential drop across InGaN to reach E_g, and thus maximum V_{bi}. $\varphi = 0.2$ for green symbols and curves, $\varphi = 0.5$ for purple symbols and curves, and $\varphi = 1.0$ for orange symbols and curves. Solid curves from exact theoretical expression for d_{min}, circles for low doping concentrations $n=10^{16}$, $i=10^{16}$, and $p=10^{16}$ cm^{-3}, and triangles are for high doping concentrations $n=10^{18}$, $i=10^{16}$, and $p=5x10^{17}$ cm^{-3}.

Another possible use of polarization is to decrease the detrimental memory effect that can occur during epitaxial growth. The term memory effect refers to residual, non-intentional

doping of a material by a dopant after the precursor is turned off. The Mg doping of GaN is prone to substantial memory effects with a dopant decay as high as 115 nm/decade [97], which may affect device performance. Procedures for minimizing the memory effect of Mg are outlined in [97]. Another option is to add an intrinsic GaN setback layer to allow the residual doping to decay to insubstantial amounts to allow for good quality heterostructures. One may either use grown p-layers or p-type substrates [98]. We find that polarization charges also stabilize device performance when setback layers are used. Figure 24 illustrates a 200 nm setback layer in the device design where the window layer thickness is 50 nm. For $\varphi = 0$, the p-n junction forms across the InGaN layer and the setback layer. However, when $\varphi = 0.25$, the polarization induced field dominates to ensure that the potential drops only across the InGaN layer. The IV curve for $\varphi = 0$ and $\varphi = 0.25$ for a 200 nm setback layer, with and without a magnesium concentration decay of a 30 nm/decade is shown in Figure 25. The modified decay rate simulated was taken from Ref. [97]. Polarization charges are seen to increase fill factor to 0.87 from unacceptable levels, showing that even thicker than necessary setback layers have good performance.

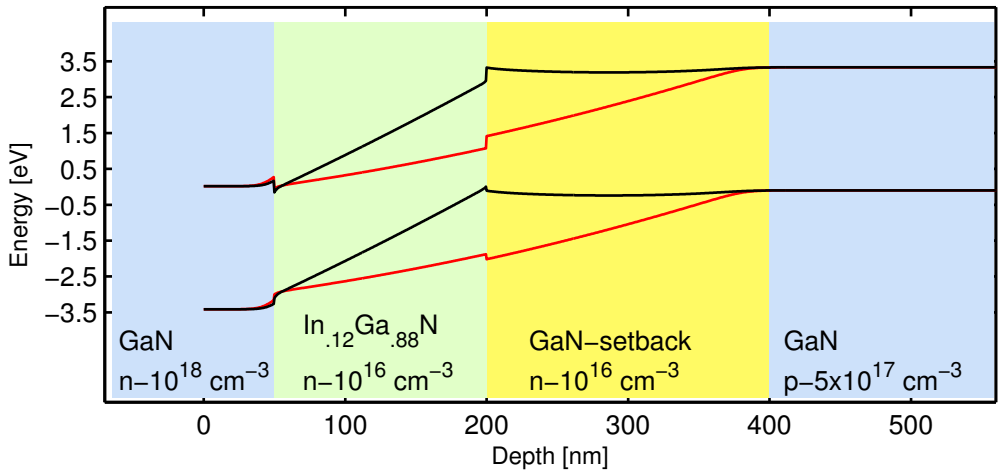

Figure 24: Conduction and valence bands of an n-i-p design with a 200 nm setback layer. Black solid curve, $\varphi = 0.25$; red dashed curve, $\varphi = 0.0$.

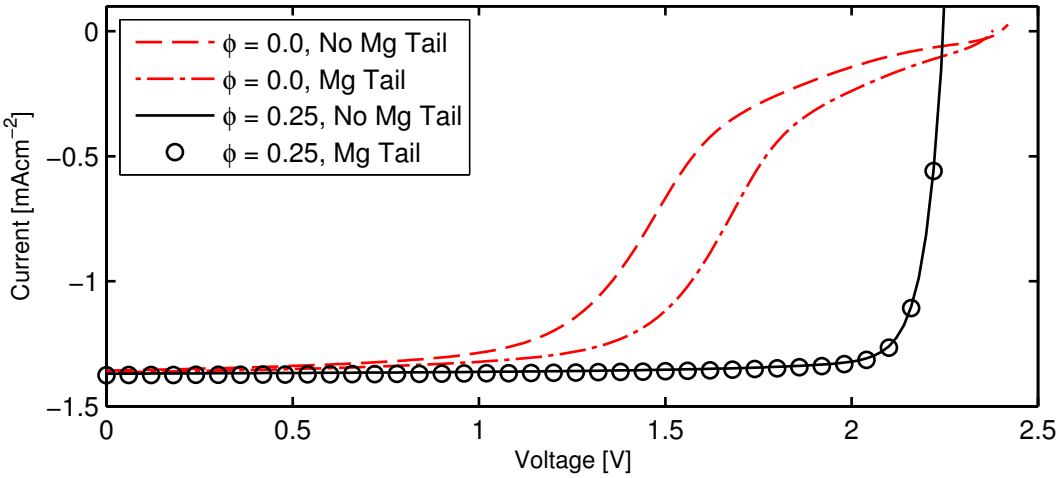

Figure 25: IV curves for setback layer designs with and without a Mg doping tail of 1 decade/30nm. The fill factor is 0.53 and 0.44 with and without a Mg tail respectively for $\varphi = 0.0$, indicated by the red dash-dotted lines. The fill factor is 0.87 both with and without the Mg tail for the $\varphi = 0.25$ polarization case indicated by the solid black curves.

Figure 26 indicates the conversion efficiency as a function of $In_{.12}Ga_{.88}N$ layer thickness for AM1.5 sunlight. As expected the efficiency increases for thicker layers, corresponding to increased light absorption, then peaks at about 235 nm. The subsequent decrease in efficiency is due to increased recombination as the electric field decreases for thicker InGaN layer. This maximum efficiency point is dependent on the 10^{16} cm^{-3} intrinsic n-doping levels of the InGaN region. Lower background doping would allow for thicker layers and increased efficiency. Polarization charges are again seen to pin the conversion efficiency to optimal levels even with a 200 nm intrinsic setback region added to the design.

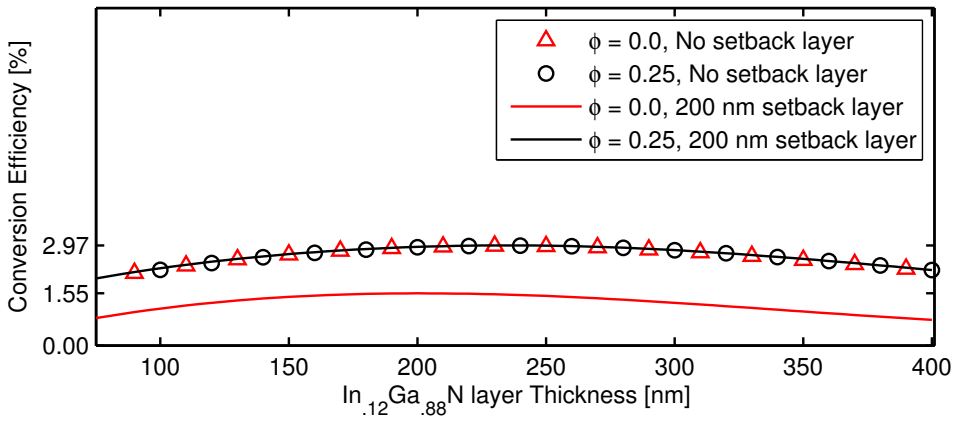

Figure 26: Conversion efficiency for $In_{.12}Ga_{.88}N$ solar cells as a function of the thickness of the $In_{.12}Ga_{.88}N$ layer. A setback layer decreases device performance unless PCs are included.

These solar cells exhibit remarkably robust independence from the thickness and doping level of the p- and n-doped layers. The minimum thickness, d_{min}, of the InGaN layer to reach maximum V_{oc} is predicted, delineating the regime where electrostatics are controlled by PCs. Further consequences of this design paradigm are improved lateral conductivity as a result of 2DEG and 2DHG regions created by self-screening. This is compatible with thinner window layers for improved AM0 and AM1.5 efficiency. We also note that p-doped GaN substrates are commercially available [98]. These principles could also potentially be applied to solar cell devices from the ZnO/CdO system, a system where p-doping is currently very difficult.

3.3 Semibulk InGaN

Our recent experimental work [24] has demonstrated 125 nm-thick InGaN layers that exhibit 2-D morphology, are coherently strained, and exhibit no phase-separation. This thick InGaN layer is created by periodically inserting an ultrathin GaN interlayer in the InGaN absorbing region and is referred to as semibulk. In this case the InGaN bulk region was experimentally replaced by 6 regions of 21 nm $In_{0.1}Ga_{0.9}N$ layers separated by 1.5 nm GaN interlayers. The HAADF-STEM images of grown semibulk material is shown in Figure 27 and it can be seen that 3D growth is prevented by these interlayers. A sample grown under the same conditions but without the interlayers results in much lower material quality and 3D growth as seen in Figure 27(b).

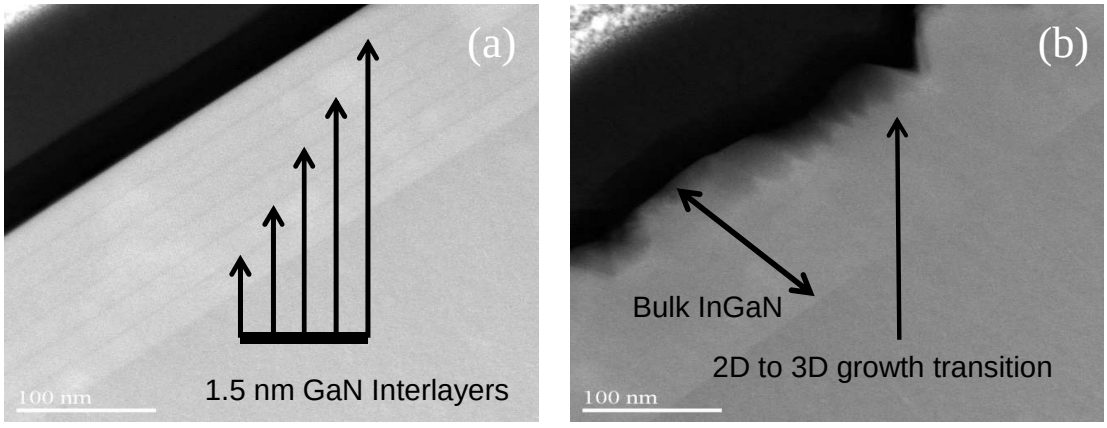

Figure 27: (a) HAADF-STEM images of semibulk InGaN with arrows indicating 1.5 nm interlayers between 23nm InGaN layers. (b) Bulk 120nm-thick InGaN sample grown under identical growth conditions.

Extensive characterization shows that semibulk InGaN has uniform indium content and is coherently strained [24]. Semibulk InGaN should increase the quality of the InGaN layer and possibly increase the solar cell performance for these devices through its improvement of material quality. It is then of interest to investigate the effect of polarization charges on these designs.

One would expect the performance to be good if the polarization charges on the interlayers do not have adverse effects on tunneling through the GaN interlayers. All simulations used twelve 12.5 nm $In_{.1}Ga_{.9}N$ layers for a total InGaN thickness of 150 nm, while the interlayer thicknesses are varied. The doping for all p-type regions is set to $5x10^{17}$ cm^{-3} while the doping in n-type regions is fixed to 10^{18} cm^{-3} and the InGaN absorption region is unintentionally doped to n-type 10^{17} cm^{-3}. We have investigated solar cell performance for a range of interlayer thicknesses and φ. The fill factor and the external quantum efficiency (EQE) for selected values of these parameters can be seen in Table 3 and Table 4 respectively.

Table 3: Semibulk $In_{.1}Ga_{.9}N$ semibulk fill factor for AM0 illumination as φ and interlayer thickness are varied.

Gan Layer (nm)	$\varphi = 0$	$\varphi = 0.25$	$\varphi = 0.50$	$\varphi = 0.75$	$\varphi = 1.0$
0.2	0.90	0.90	0.90	0.90	0.90
0.5	0.89	0.90	0.89	0.88	0.86
1.0	0.89	0.88	0.83	0.64	0.44
1.5	0.86	0.82	0.59	0.39	0.37
2.0	0.78	0.69	0.41	0.36	0.35
2.5	0.63	0.56	0.36	0.34	0.33

Table 4: Semibulk $In_{.1}Ga_{.9}N$ semibulk EQE (%) for AM0 illumination as φ and interlayer thickness are varied.

Gan Layer (nm)	$\varphi = 0$	$\varphi = 0.25$	$\varphi = 0.50$	$\varphi = 0.75$	$\varphi = 1.0$
0.2	2.00	2.00	2.00	2.00	2.00
0.5	2.00	2.00	1.99	1.96	1.90
1.0	1.98	1.96	1.83	1.37	0.86
1.5	1.92	1.81	1.25	0.72	0.63
2.0	1.73	1.49	0.80	0.61	0.57
2.5	1.36	1.18	0.63	0.56	0.53

As expected, the fill factor and EQE drop for thicker GaN interlayers. Increased polarization also decreases the fill factor and EQE. Very roughly, we see that every increase of φ by 0.25 is equivalent to approximately a 0.5 nm increase in the interlayer thickness for 10% indium content. Conduction bands for interlayer thicknesses of 1.0 nm are shown in Figure 28 and 4.0 nm are shown in Figure 29 for the cases of $\varphi = 0$ and $\varphi = 1$. A visual inspection of Figure 28 and Figure 29 shows that maximum polarization charges ($\varphi = 1$) cause a distortion of the energy bands, which significantly increase the distance that photocarriers must tunnel. The increased tunneling distance increases recombination, lowering the short-circuit current, and it would also increase the series resistance of the device. That this is the case is evident in resulting V-I curves, which exhibit decreased short-circuit current and lower fill-factor. We therefore conclude that the n-i-p configuration is interesting for interlayer thickness up to 1.5 nm for $\varphi \leq 0.25$ and up to 1.0 nm for $\varphi \leq 0.5$, which is predicted to degrade the performance by less than 10%. Because p-doped substrates are commercially available [98], one may grow the proposed devices by inserting an i-GaN setback layer on the p- substrates before i-InGaN growth is started. The effectiveness of setback layers was shown above in Figure 24.

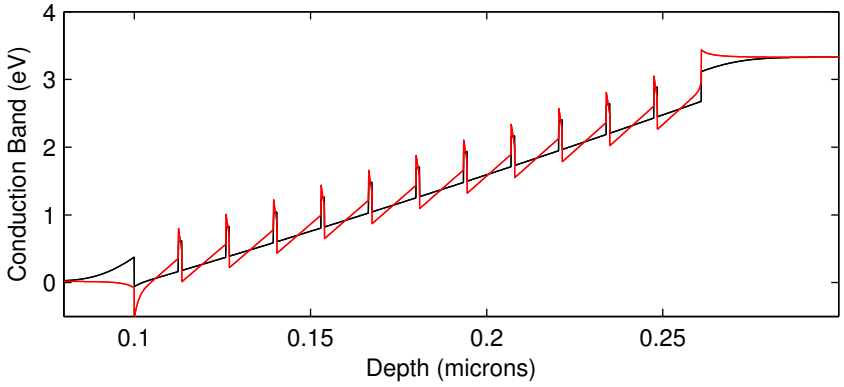

Figure 28: Semibulk conduction band using 1 nm GaN interlayers. Black curves correspond to $\varphi = 0$ and red curves correspond to $\varphi = 1$.

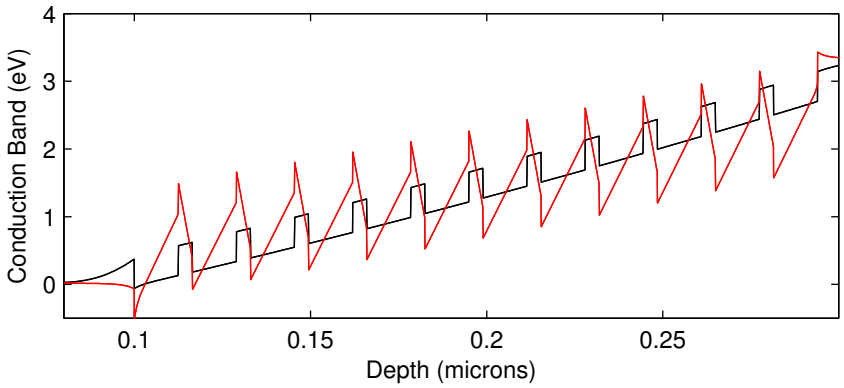

Figure 29: Semibulk conduction band using 4 nm GaN interlayers. Black curves correspond to $\varphi = 0$ and red curves correspond to $\varphi = 1$.

We have shown that thin interlayers that have been added inside the InGaN layer to improve material quality are compatible with an n-i-p on Ga-face substrate configuration, and that the interlayers decrease device EQE less than 5% for interlayer thickness up to 1.5 nm when polarization charges are not present. As long as the GaN layers are ≤ 1 nm thick and $\varphi \leq 0.5$, the effects of polarization degrade the EQE by less than 10%. Because a corresponding p-i-n design at $\varphi = 0.5$ has a greatly reduced EQE, we conclude that the n-i-p structure is more favorable for semibulk InGaN. We identify the cause of degradation in n-i-p structures to be an increased tunneling distance for photocarriers, resulting in degraded EQE and fill factor by increasing recombination and series resistance.

CHAPTER 4

POLARIZATION ENGINEERED TUNNEL JUNCTIONS FOR INGAN MJSCS

InGaN is an ideal candidate for multi-junction solar cell (MJSC) applications as it is direct bandgap from 0.68 to 3.43 eV, which covers the majority of the solar spectrum. Unfortunately, the high level of doping needed to create the p+/n+ tunnel junctions inside these MJSCs is not currently possible. Without a suitable method of creating a tunnel junction, creating MJSCs using InGaN will not be possible, even with perfect InGaN material quality.

Recent work has experimentally demonstrated tunnel junction diodes based on polarization-induced electric fields [5, 6]. These devices, called polarization-based tunnel junctions (PTJs), use the strong polarization-induced electric fields to bring the the conduction and valence bands in close proximity to enable the possibility of tunneling. Thus PCs replace the role of p+/n+ in creating a tunnel junction. The experimental results for III-N tunneling devices will be discussed in the next section.

Despite the success of these PTJ devices, to date an accurate model for calculating current through PTJs has not been established. This work will address two general problems. First, an accurate model for predicting PTJ current must be formulated. Second, design configurations that lead to favorable PTJ current need to be analyzed.

The heart of all tunneling current equations is the function for estimating the probability of tunneling. Therefore this will be discussed before the tunneling equation is introduced. Two methods of calculating tunneling probability will be outlined. The first method is the Wentzel-Kramers-Brillouin (WKB) approximation. This is an analytic approximation, that is computationally inexpensive and has been used to successfully predict the majority of TJ devices. A second method is the more complicated numerical quantum matrix (QM) method. This method treats the tunneling particle as a wave and solves the Schrodinger

equation through the device using various boundary conditions at interfaces. A comparison of the WKB and QM method will be shown to indicate their differences.

Once the means of determining the tunneling probability is established, a new equation for tunneling will be derived. The equation used to calculate classic tunneling diode problems assumes a 3D density of states (DOS) carrier profile throughout the device. However, for PTJs the 2D DOS nature of III-N heterojunction interfaces needs to be considered. As will be discussed below, this will lead to a change in the leading coefficient of the tunneling equation and lead to a change in the limits of integration. The methodology of solving for the energy bands and predicting current with an applied bias will be outlined. The calculated reverse and forward bias currents for several PTJs are compared with experiment.

The second major consideration for InGaN MJSC is the design configuration. InGaN and AlN have both been proposed as the principle material for creating a PTJ. It will be shown that under certain configurations the InGaN based PTJ will not lead to an efficient device. Furthermore, using a single barrier AlN layer will not provide enough current to allow for all the photo-generated carriers to pass through. This chapter will conclude with the discussion of a novel two-barrier PTJ design that will allow for high levels of current. These two-barrier PTJ rely on resonant tunneling effects. The high currents from two-barrier PTJs allow for multi-sun illumination where a simple one-barrier design is inadequate. The results of this study provide a means to successfully create InGaN based MJSCs.

4.1 State-of-the-art III-N device Tunnel Junctions

The quantum-mechanical principle of tunneling was famously verified in 1958 with the first demonstrated tunnel diode [99]. Esaki showed that with high levels of doping, generally degenerate, it is possible for the conduction and valence bands to cross and thus create a tunnel junction (TJ). When this happens the available state for the electron on the other side of the barrier is a hole in the valence band. This process is referred to as interband tunneling. Tunnel junctions are devices that can exhibit very little resistance for negative bias and for small forward bias. After a few mV of forward bias, the current reaches a peak and exhibits a negative-forward-differential resistance for any further applied forward bias. This negative-forward-differential resistance, where current decreases with increased bias, is a famous characteristic of TJ devices.

Classical tunnel junctions make use of the non-local interband tunneling of carriers between an n+ and a p+ region. The doping required is on the order of 10^{20} cm^{-3} for both regions. Unfortunately, P-type doping has long been a limiting factor for wide-bandgap materials such as AlGaN, GaN, ZnO, and MgZnO. Additionally, the wider bandgap of these devices would further increase the difficulty of tunneling compared to low bandgap materials like GaAs, Ge, and Si, as will be shown latter. Early attempts to create TJs using degenerate doping were not very successful and led to very high tunneling resistances [100, 101] as high as 45 Ω cm^2.

In 2005, Grundmann proposed to use the polarization effects of strained AlN on GaN to create conditions favorable for interband tunneling [102]. The principle is that the strong electric field of the polarization would assist high doping levels and decrease the thickness of the barrier to the point where tunneling is favorable. For instance, high doping levels of N_A=10^{19} and N_D=9x10^{19} would create a barrier thickness of 25 nm in a GaN TJ device, while a strained 3 nm thick AlN layer is all that is needed to create a PTJ device [6]. In 2011, InGaN was studied as a possible alternative to AlN as the principle medium for creating a PTJ [5]. Very recently a PTJ grown in series with a GaN p-n junction was used

to eliminate the need for a p-type contact, which is another difficult fabrication step in III-N devices [7].

4.2 WKB and QM methods for calculating tunneling

The WKB approximation for tunneling is given by

$$\mathrm{T}_{\mathrm{wkb}}(E) = e^{-2\varphi(x,E)}, \text{ where} \tag{8}$$

$$\varphi(x,E) = \int_0^l \sqrt{\frac{2m^*}{\hbar^2}(V(x) - E)}\mathrm{d}x\,. \tag{9}$$

The derivation of 8 will not be shown here but can be easily found in textbooks such as [65]. The symbol l represents the thickness of the potential barrier, and the qauntity $(\varphi - \mathcal{E})$ is the height of the potential as a function of position for a given electron total energy. Finally, m^* is the reduced effective mass of the tunneling particle: Equation 10.

$$m^* = \left(\frac{1}{m_e^*} + \frac{1}{m_h^*}\right)^{-1}, \tag{10}$$

where m_e^* is the electron effective mass and m_h^* is the hole effective mass. For the III-N system the electron effective mass ranges from .07 to .35 times m_O, the mass of a free electron, see Table 1. While the values of electron effective mass is well established and accepted, the effective mass of the hole is much more complicated to calculate and values range dramatically in both theoretically and experimentally reported values [1]. For all simulations the hole effective mass is simply set to m_O for all materials.

While Equation 8 is a nice analytical expression for tunneling probability calculations, the electrostatic potential, V(x), for our devices is not analytic. Therefore, we must numerically integrate Equation 9. The function V(x) is generated directly from Silvaco simulations and is a discrete function rather than a continuous function, with a grid spacing as small as 0.1 nm. A simple Riemann sum is used to determine the resulting tunneling probability. In order to increase the accuracy of the estimation V(x) is interpolated linearly over a grid with spacing smaller than 2 picometers.

The WKB method provides a very direct method for calculating the tunneling probability for a particle through a potential barrier. It is computationally inexpensive and is very

useful for a wide range of tunneling devices. However, in instances where the potential profile varies rapidly compared to the de Broglie wavelength of the carriers the assumptions assumed in the derivation of the WKB approximation are no longer valid. Many of the PTJ devices we will explore contain at least one quantum well. In the region of quantum wells, the thickness of the well becomes comparable to the de Broglie wavelength of the carrier which leads to quantum confinement and the creation of energy subbands or discrete energy levels within the quatum well. This effect is in direct conflict with the basic assumptions used to formulate the WKB approximation.

The WKB method is also inadequate for devices that have resonant tunneling. In fact, the results of Equation 8 do not depend on the profile of the potential. Any profile that results in the same area inside the integral will achieve the same probability [103]. Quantum tunneling occurs when an electron that is incident on one or more potential barriers has a non-zero probability of traveling through the barriers. While the transmission coefficient is always less than one for a single barrier, the wavelike nature of the electron allows for unity transmission in some instances if there are two or more barriers. This is referred to as resonant tunneling and has been the focus of numerous studies.

While many possible solutions for determining resonant tunneling have been proposed, the transfer matrix approach will be used [104–106]. The basis of this method is to consider the wavefunction, ψ, shown in Equation 11:

$$\psi(x) = Ae^{ikx} + Be^{-ikx} = \begin{pmatrix} e^{ikx} & e^{-ikx} \end{pmatrix} \begin{pmatrix} A \\ B \end{pmatrix}, \tag{11}$$

which is valid for a region of constant potential. Equation 11 is a solution to the one-dimensional, time independent Schrodinger equation if the wavenumber, k, is defined as

$$k = \sqrt{2m^*(E - V)/\hbar^2}, \tag{12}$$

where E is the total kinetic energy of the particle, V is the potential, and m^* is the effective mass of the particle. The transfer-matrix method is used to determine change in the wavefunction as it passes through a discontinuity in the potential profile. A simple step discontinuity is shown in Figure 30.

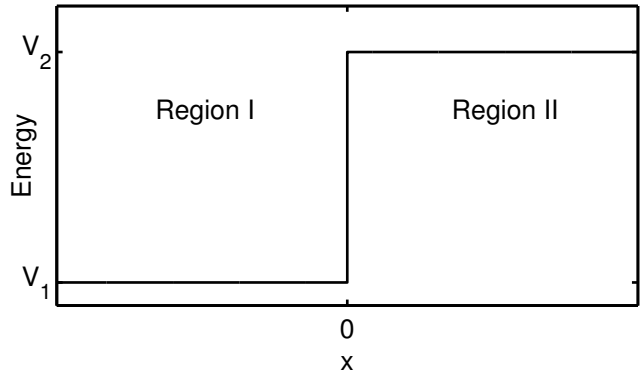

Figure 30: A step potential discontinuity. The boundary conditions at x=0 determine the change in ψ as it crosses from Region I to Region II.

The wavefunctions in the two regions of Figure 30 are of the form:

$$\psi_1(x) = A_1 e^{ik_1 x} + B_1 e^{-ik_1 x} \tag{13a}$$

$$\psi_2(x) = A_2 e^{ik_2 x} + B_2 e^{-ik_2 x}. \tag{13b}$$

The wavenumber in a particular region is

$$k_i = \sqrt{2m_i^*(E - V_i)/\hbar^2}, \tag{14}$$

where the subscripts refer to the value of the effective mass and potential in a particular region. The energy of the particle is assumed to remain constant in both regions. By setting two boundary conditions (BCs) on the interface, we can solve for A_2 and B_2 if we select a value for A_1 and B_1. Conceptually it is easier to work backwards. We first assume that $B_2 = 0$, which implies that there are no carriers incident on region I that come from region II. We then normalize the wavefunctions by assuming that $A_2 = 1$.

The boundary conditions imposed on the wavefunctions ψ_1 and ψ_2 at the interface are

$$\psi_1(0) = \psi_2(0) \tag{15a}$$

$$\left.\frac{1}{m_1^*}\frac{d\psi_1(x)}{dx}\right|_{x=0} = \left.\frac{1}{m_2^*}\frac{d\psi_2(x)}{dx}\right|_{x=0}. \tag{15b}$$

Equation 15a is simply the requirement that the wavefunctions be continuous at the interface. The second equation, Equation 15b, as indicated in [107], is a result of the necessity of having continuity in the probability density current, J, which is related to the wave function ψ by

$$J = \frac{q\hbar}{2im^*}\left(\frac{\psi^* d\psi}{dx} - \frac{\psi d\psi^*}{dx}\right). \tag{16}$$

While it is mathematically possible to solve for the transfer matrix for an interface at some arbitrary position x, it is more convenient to solve the BCs by assuming that the interface is at $x = 0$. This results in:

$$A_1 + B_1 = A_2 + B_2 \tag{17a}$$

$$\frac{ik_1}{m_1^*}A_1 + \frac{-ik_1}{m_1^*}B_1 = \frac{ik_2}{m_2^*}A_2 + \frac{-ik_2}{m_2^*}B_2. \tag{17b}$$

It is useful to point out that for the evaluation of the first derivative with respect to x, the value of k is constant with position inside a specific region. Equations 17a and 17b can be readily arranged into a matrix as follows:

$$\begin{pmatrix} 1 & 1 \\ \frac{ik_1}{m_1^*} & \frac{-ik_1}{m_1^*} \end{pmatrix}\begin{pmatrix} A_1 \\ B_1 \end{pmatrix} = \begin{pmatrix} 1 & 1 \\ \frac{ik_2}{m_2^*} & \frac{-ik_2}{m_2^*} \end{pmatrix}\begin{pmatrix} A_2 \\ B_2 \end{pmatrix} \tag{18a}$$

$$\begin{pmatrix} \frac{1}{2} & \frac{-im_1^*}{2*k_1} \\ \frac{1}{2} & \frac{im_1^*}{2*k_1} \end{pmatrix}\begin{pmatrix} 1 & 1 \\ \frac{ik_1}{m_1^*} & \frac{-ik_1}{m_1^*} \end{pmatrix}\begin{pmatrix} A_1 \\ B_1 \end{pmatrix} = \begin{pmatrix} \frac{1}{2} & \frac{-im_1^*}{2*k_1} \\ \frac{1}{2} & \frac{im_1^*}{2*k_1} \end{pmatrix}\begin{pmatrix} 1 & 1 \\ \frac{ik_2}{m_2^*} & \frac{-ik_2}{m_2^*} \end{pmatrix}\begin{pmatrix} A_2 \\ B_2 \end{pmatrix} \tag{18b}$$

$$\begin{pmatrix} A_1 \\ B_1 \end{pmatrix} = \frac{1}{2}\begin{pmatrix} 1+\frac{m_1^*}{m_2^*}\frac{k_2}{k_1} & 1-\frac{m_1^*}{m_2^*}\frac{k_2}{k_1} \\ 1-\frac{m_1^*}{m_2^*}\frac{k_2}{k_1} & 1+\frac{m_1^*}{m_2^*}\frac{k_2}{k_1} \end{pmatrix}\begin{pmatrix} A_2 \\ B_2 \end{pmatrix} \tag{18c}$$

$$\begin{pmatrix} A_1 \\ B_1 \end{pmatrix} = \mathbf{D}\begin{pmatrix} A_2 \\ B_2 \end{pmatrix}. \tag{18d}$$

The discontinuity matrix **D** reduces to the identity matrix if $m_1^* = m_2^*$ and $k_1 = k_2$. The discontinuity matrix as shown is only valid at a single position, $x = 0$. However, we can extend the usefulness of **D** to any arbitrary position $x = a$, by simply translating the coordinate system so that any particular discontinuity is centered at $x' = 0$. This is done through the use of a propagation matrix **P**, where the wavefunction ψ' in the new coordinate system, x', is related to the original wavefunction by $\psi'(x') = \psi(x)$. The derivation is straightforward but is included for completeness in Equation 19:

$$\begin{aligned} \psi'(x') &= \psi(x) \\ A'e^{ikx'} + B'e^{-ikx'} &= \psi(x'+a) \\ A'e^{ikx'} + B'e^{-ikx'} &= Ae^{ikx'}e^{ika} + Be^{-ikx'}e^{-ika} \\ A' + B' &= Ae^{ika} + Be^{-ika}. \end{aligned} \tag{19}$$

The value of k is constant and depends on the region that the wavefunction is traveling through. Equation 19 in matrix notation is as follows:

$$\begin{pmatrix} A' \\ B' \end{pmatrix} = \begin{pmatrix} e^{ika} & 0 \\ 0 & e^{-ika} \end{pmatrix} \begin{pmatrix} A \\ B \end{pmatrix}$$

$$\begin{pmatrix} A' \\ B' \end{pmatrix} = \mathbf{P} \begin{pmatrix} A \\ B \end{pmatrix}. \tag{20}$$

The use of the discontinuity matrix and the propagation matrix is sufficient to estimate the transmission coefficient for any arbitrary potential barrier that will be encountered in the semiconductor devices of interest here. The objective is to calculate the QM transfer matrix, **T**, as defined by

$$\begin{pmatrix} A_0 \\ B_0 \end{pmatrix} = \mathbf{T} \begin{pmatrix} A_N \\ B_N \end{pmatrix}. \tag{21}$$

The potential is discretized into N regions with N+1 nodes, where each region has a thickness of *a*. Each node represents a possible discontinuity interface where the region material parameters between x_{j-1} and x_j, are defined by the material parameters of the device at the node x_j. **T** is constructed as follows:

$$\mathbf{T} = \mathbf{T}_0 \mathbf{T}_1 \mathbf{T}_2 \cdots \mathbf{T}_N. \tag{22}$$

The first element of **T**, $\mathbf{T}_0$, is set to be the 2x2 identity matrix. All other elements of **T** are defined as

$$\mathbf{T}_j = \mathbf{D}_j \mathbf{P}_j, \tag{23}$$

where $\mathbf{D}_j$ and $\mathbf{P}_j$ are defined according to Equations 18 and 20 where $k_1 = k(x_j)$, $k = k_2 = k(x_{j+1})$, $m_1 = m(x_j)$, and $m_2 = m(x_{j+1})$. Each node from j = 1 to j = N is evaluated to create the term **T**. This process can be thought of as the sequence of taking a particular starting wavefunction, calculating its new form at a particular interface, then propagating the new shape forward, a distance of *a*, upon which we are at a new interface. The process is repeated until we reach the end of the device.

At this point it is useful to point out a few properties of **D** and **P**. The discontinuity matrix naturally reduces to the identity matrix for regions of constant potential and effective mass. The propagation matrix, **P**, for any energy higher than the potential is simply a phase shift of the wavefunction. However in cases which the energy is lower than the potential, the value of k is no longer real and **P** then contains both an exponentially increasing and an exponentially decaying term. Both of these terms need to be included in all calculations, one cannot simply remove the exponentially increasing term. The treatment of these terms is determined by the expected form of the wavefunction, ψ_n. For instance, if the final potential barrier is of infinite extent, then A_N must be set to zero for energies lower than the final barrier. No particles are expected to travel through any infinite barrier of energy greater than the particle.

In order to find the tunneling probability we make the assumption that $B_N = 0$. This is the equivalent of saying that we have no incident particles coming from the right. The value for A_N is set to unity to normalize the wavefunction. This final choice for the boundary conditions implies the following relations:

$$\begin{aligned} A_0 &= T_{11} \\ B_0 &= T_{21} \\ R_{QM} &= \frac{T_{21}T_{21}^*}{T_{11}T_{11}^*} \\ T_{QM} &= 1 - \frac{T_{21}T_{21}^*}{T_{11}T_{11}^*}. \end{aligned} \tag{24}$$

One could also write T_{QM} as

$$T_{QM} = \frac{m_1^*}{m_N^*}\frac{1}{T_{11}T_{11}^*}. \tag{25}$$

The tunneling probability T_{QM} can therefore be readily solved for any arbitrary potential. The accuracy of the calculations increases with the number of regions used, but the magnitude of the error introduced as a function of N has not been extensively calculated. A

relatively old paper on the QM method, from 1987, indicated no visible change in the plot of the transmission coefficient when going from 40 to 80 regions for a 35 nm barrier [105]. Because of the speed of current computer processors, computations using around three thousand points for a 40 nm region can be done in a matter of seconds.

4.2.1 Comparison of WKB and QM methods

An example of tunneling through a single barrier is shown in Figure 31. The transfer coefficient, which is the probability that a particle will successfully tunnel through a barrier, is shown in Figure 31(b). The particle-like nature of the WKB method can be seen in the fact that for electron energies higher than the 1 eV barrier, there is unity transmission. This corresponds to the semiclassical nature of the derivation of the WKB method. Classically, if the particle has more energy than the barrier, then there is a 100% chance that it will travel over the barrier. The wave-like nature of the QM method can be seen in the Ramsauer peaks that form for electrons with energy higher than the barrier [106].

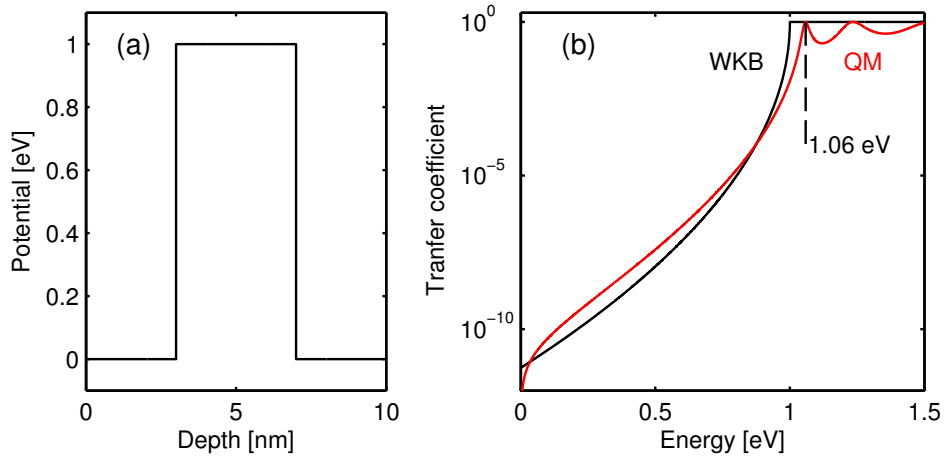

Figure 31: (a) A single 4 nm, 1 eV barrier. The effective mass inside the barrier is $0.4m_O$ whereas the outside the barrier it is $0.2m_O$. (b) The transmission probability as a function of energy using the WKB and QM methods.

The wave-like treatment of particles by the QM method is precisely what allows for the

prediction of resonant transmission. Resonant tunneling can occur once there are two or more barriers. For certain incident electron energies, the transmission through both barriers can approach unity for energies less than the barrier height. An example of two barriers is shown in Figure 32. In this example the barriers are 2.5 nm thick and separated by 5 nm. The effective mass inside barriers is set to $0.3m_O$ and is set to $0.2m_O$ outside the barriers. In this example the WKB is unable to predict the resonant energy levels that correspond to the eigenenergies of the QW. For non-resonant cases the WKB and QM methods are generally within two or three orders of magnitude difference.

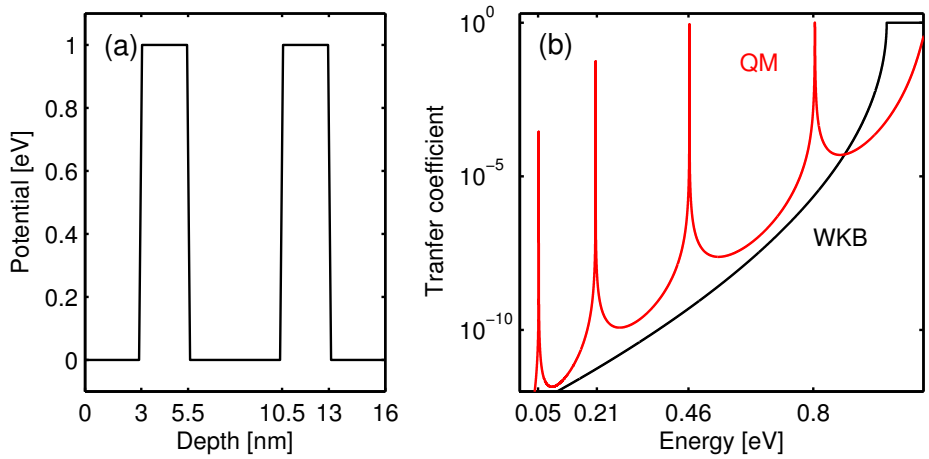

Figure 32: (a) A double barrier structure. (b) The resonant nature of the electron is detected in the QM method, but is not apparent in the WKB approximation. The resonant peaks occur at the eigenenergy values of the quantum well created by the two barriers.

The magnitude squared of the wavefunction for the QM method is shown in Figure 33 and is useful to see the nature of the wavefunction at the resonant energy levels.

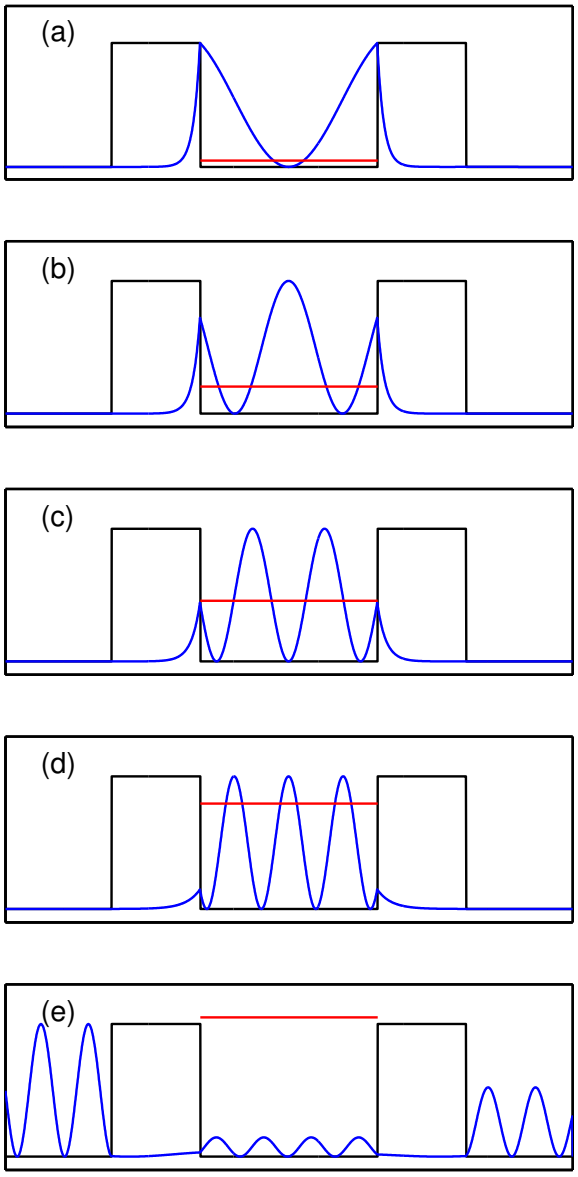

Figure 33: (a-d) Normalized $|\psi|^2$ for the four eigenenergies of the quantum well formed by the two barriers. (e) $|\psi|^2$ for a non-resonant case where the transmission probability is high. The sinusoidal curve of $|\psi|^2$ outside of the QM indicates the lack of resonant conditions in this case.

4.3 Calculating the PTJ current

The tunneling current equation typically used to approximate the tunneling current, J_{T3D}, is shown here:

$$J_{T3D}(V_{AB}) = \frac{qm^*}{2\pi^2\hbar^3}\int_0^{qV_{AB}}\int_0^{E} F\,(E, V_{AB})\,T\,(E, V_{AB})\;\mathrm{d}E_{\perp}\,\mathrm{d}E. \tag{26}$$

Here q is the elementary positive charge and $\hbar$ is the reduced Planck's constant. While Equation 26 works well for TJ applications, a few inherent differences in PTJs merit careful consideration. The primary need for adjustments in Equation 26 stem from the formation of the 2DEG and 2DHG at the heterointerfaces as shown in Figure 34. Components of the equation such as the treatment of the leading coefficient, the determination of the limits of integration, the specification of how the applied bias drops through the PTJ, and other details are explained in the next few sections.

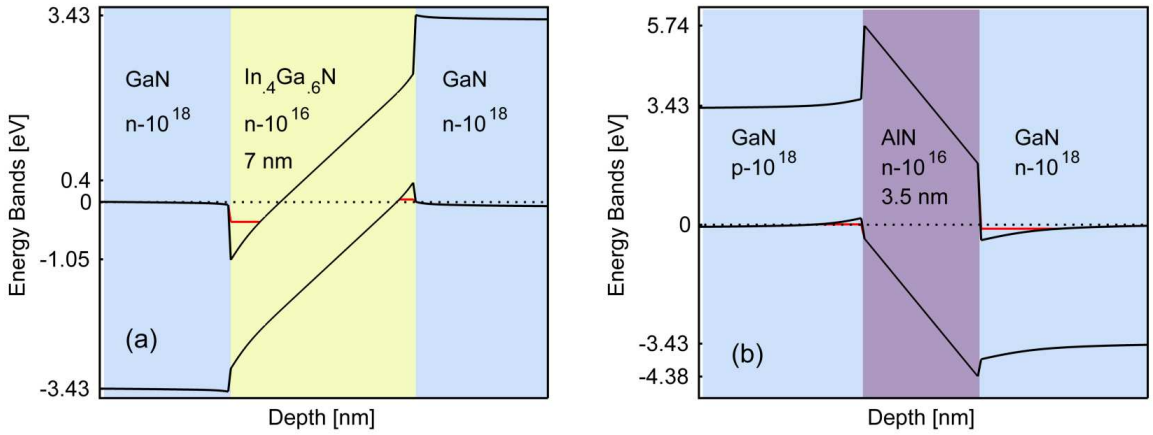

Figure 34: (a) InGaN PTJ structure from [5]. (b) AlN PTJ structure from [6]. The formation of the 2DEG and 2DHG from the strong polarization fields changes the nature of the many components of Equation 26 such as the limits of integration and tunneling lengths.

4.3.1 Carrier Statistics

Successful tunneling requires that an electron is available on one side and that a hole is available on the other side of the PTJ for a given energy. This probability, $F(E, V)$, is calculated using Fermi-Dirac distribution functions as follows:

$$\begin{aligned} F(E, V_{AB}) &= f^n(E, V_{AB}) - f^p(E, V_{AB}) \\ &= \frac{1}{1 + e^{\left(\frac{E - E_f}{k_b T}\right)}} - \frac{1}{1 + e^{\left(\frac{E - (E_f - qV_{AB})}{k_b T}\right)}}. \end{aligned} \tag{27}$$

Here k_b is the Boltzmann constant in eV/K, and T is the temperature. The symbols f^p and f^n represent the probabilities of finding an electron on the p-side and n-side, respectively, of the tunnel junction for a given energy and applied bias. The Boltzmann approximation of Fermi-Dirac distribution is not applicable as we are dealing with degenerately doped regions.

The first and second term on the RHS of Equation 27 are similar except for the value of qV_{AB} found in the second term. Because of this, $F(E, V_{AB})$ is identically zero when $V_{AB} = 0$. The range of Equation 27 is $(-1 \geq F(E, V_{AB}) \geq 1)$ with the sign following the sign of V_{AB}. Thus $F(E, V_{AB})$ is what specifies the direction of the current as all other components of Equation 26 are positive valued. As defined in Equation 27, a positive value implies a positive current traveling from the p-side to the n-side of the PTJ.

4.3.2 Tunneling Probability

The tunneling probability $T(E, V_{AB})$ can be calculated using either the WKB or WM methods outlined above. In either case, the tunneling distance needs to be clearly defined. It should be noted here that $T(E, V_{AB})$ is written as a function of the applied bias as a reminder that the energy bands change for each value of V_{AB} which affects the shape of the barrier the electron is tunneling through. The exact manner in which the energy bands change with applied bias will be discussed later. The tunneling distance can also depend

on the total energy of the electron. The tunneling length as defined in our model is shown in Figure 35. Except in the cases of significant applied Bias, $V_{AB} \geq 3V$, tunneling distance for AlGaN barriers is simply the thickness of the barrier. However, for InGaN barriers, we take the tunneling distance as shown in Figure 35(a). Tunneling starts when, for a given energy E, an electron reaches the conduction band on one side, and tunneling ends when the electron reaches the valence band level on the other side of the barrier. For the InGaN device a reverse bias tends to decrease the tunneling distance, leading to increased current.

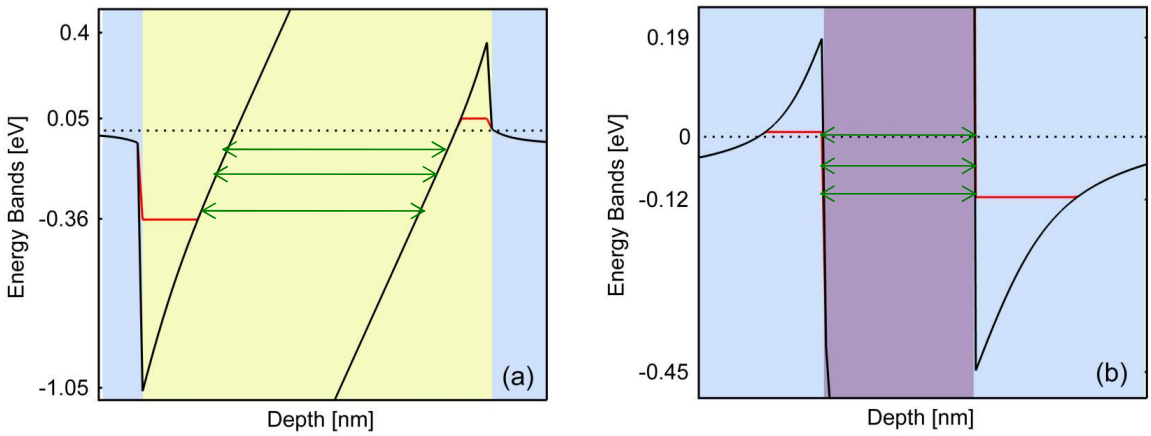

Figure 35: Devices from Figure 34, zoomed to show the tunneling area of concern. (a) InGaN PTJ tunneling distances are normally shorter than the InGaN layer thickness. For a particular applied bias voltage, the tunneling distance is relatively constant with respect to electron energy. However, the distance is likely to decrease with increasingly negative bias conditions. (b) AlGaN PTJ tunneling distances are equal to the thickness of the AlGaN layer. AlGaN tunneling distances remain constant for normal bias conditions where $|V_{AB}| \leq 2V$.

As a final note on tunneling probabilities, in our model we make a simple assumption that once the electron reaches the other side of a barrier, it is considered transmitted and subsequently added to the overall tunneling current. No calculations are performed to determine the probability of having a hole with the appropriate momentum for recombination is available. The recombination rate is assumed to be instantaneous. If the Fermi statistics indicate that there is an available state for the electron to exist in after tunneling, then it is simply counted and added to the tunneling current.

4.3.3 The drop of the applied bias V_{AB} over the depletion region

The applied voltage bias, V_{AB}, is the separation of the Fermi levels on either side of the tunnel junction. It is important to note that with this model any applied voltage is applied directly to the tunnel junction endpoints, not the device contacts. In essence we assume that V_{AB} is the portion of the applied bias on a given device that drops only over the tunnel junction region. This detail is important for comparing theoretical with experimentally demonstrated V-I curves.

Once an applied bias is set, the corresponding current will need to be considered in order to determine the change in the energy bands. Unfortunately, the Silvaco Poisson-Schrodinger solver is only valid for equilibrium conditions. Thus only the initial energy band profile is available for calculations and must be manually altered for applied bias voltages. We make a simple assumption that the applied bias drops linearly across the depletion region. The depletion regions are defined according to Figure 36.

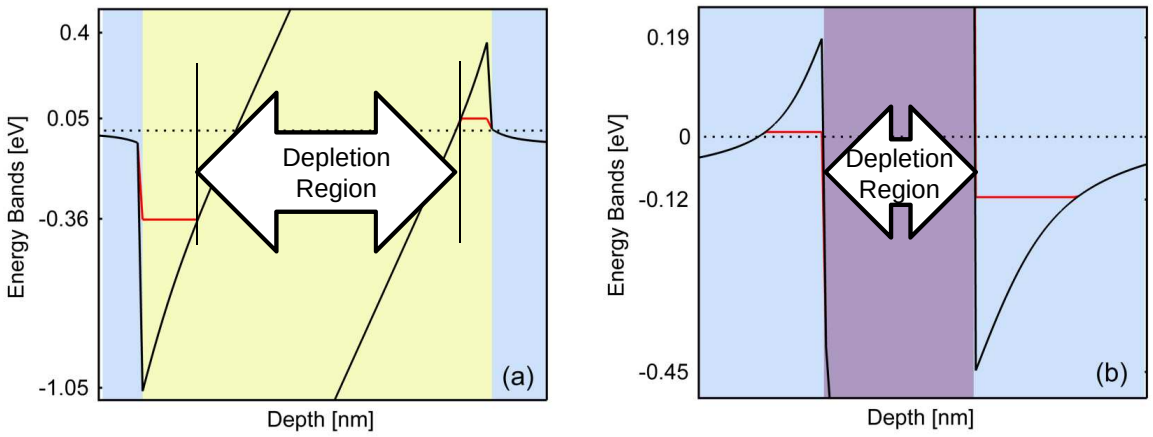

Figure 36: Devices from Figure 34, zoomed to show the tunneling area of concern. (a) InGaN PTJ depletion region are defined as the region between the edges of the 2DEG and the 2DHG ground state energy levels. (b) The AlGaN PTJ depletion region is simply the AlGaN layer.

As seen in Figure 36(a), defining the depletion region in the InGaN layer is not a simple task. In this case, the high concentrations of carriers located inside the 2DEG and 2DHG regions correspond to very low resistances and thus would not allow for any significant

drop in potential for an applied bias. We therefore, as a first order approximation, assume that all of the applied bias will drop from the edge of the 2DEG region to the edge of the 2DHG region, which we will assume are defined by the ground state energy levels. For reverse bias conditions this approximation is not expected to introduce substantial errors, however for high forward bias voltages the edges of the 2DEG and 2DHG regions would be expected to deviate substantially. Fortunately we can ignore this detail as only a few tens of millivolts of forward bias is typically needed before the energy bands uncross and tunneling is prohibited.

For AlGaN layers, the entire AlGaN layer is considered to be the depletion region. With the wide-bandgap of AlGaN, this assumption is accurate as excess carriers in the AlGaN would likely diffuse to the lower bandgap neighboring regions.

The applied bias could also alter the PC densities at the heterointerfaces. However, if for instance, we wanted to calculate -4 V on the device, then the change of the PC densities would be expected to have a rather large impact on the device performance. However, most of the other assumptions would likely fail and would need to be reconsidered. For the -1 to +1 range typically used, the PC change deviation would change by approximately 3% and this effect is therefore considered negligible and ignored.

4.3.4 The leading coefficient

One of the most basic assumptions used in formation of Equation 26 is that the density of states is 3D. This is accurate for heavily doped tunnel junction configurations, but for the III-nitride devices it fails to account for the 2D DOS that naturally arise as a result of the large polarization induced electric fields. As mentioned before, the extremely high polarization induced fields are capable of dropping the potential several eV in just a few nanometers. Any further increase in layer thickness will create quantum wells at the interfaces as the bands push through the fermi level and create quantum wells.

The derivation of Equation 26 can be found in [65]. The use of a 2D rather than 3D

density of states changes the results by a factor of 2π and changes the energy levels available for tunneling as explained above. The derivation is included here for completeness.

First we assume that there is an incident flux of carriers at the tunneling interface. The product of this flux, the tunneling probability $T(E, V_{AB})$, and $F(E, V_{AB})$ are integrated over the appropriate energy range to give the tunneling current. The flux of electrons per unit volume in a ring with perpendicular wave vector $k_\perp$ to $k_\perp + \mathrm{d}k_\perp$, is equal to the product of the elementary positive charge, the velocity of the particle in k space, the area of the ring of the incident particles, and the density of states in k space [65]. We assume that k can be decomposed into two parts, $k_\parallel$ and $k_\perp$ as we did for the total energy, E.

The velocity in k space is defined as $\mathrm{d}k/\mathrm{d}t$ which is equivalent to $\mathrm{qF}/\hbar$ where F is the electric field from the applied bias. This corresponds to our linear approximation for the drop in the applied bias over the depletion region. The 2D density of states in k space is $1/2\pi^2$, where a factor of 2 is included to account for spin degeneracy. The final component needed is the area of the ring, $2\pi k_\perp \mathrm{d}k_\perp$. The product of these components is written as

$$incident\,flux = \frac{q^2 F k_\perp \mathrm{d}k_\perp}{\hbar\pi}. \tag{28}$$

To proceed it is useful to use the parabolic energy band assumption:

$$E_\perp = \frac{\hbar^2 k_\perp^2}{2m^*}. \tag{29}$$

Taking the derivative of $E_\perp$ with respect to $k_\perp$ gives:

$$\frac{\mathrm{d}E_\perp}{\mathrm{d}k_\perp} = \frac{\hbar^2 k_\perp}{m^*}. \tag{30}$$

Which is rearranged to give:

$$k_\perp \mathrm{d}k_\perp = \frac{\mathrm{d}E_\perp m^*}{\hbar^2}. \tag{31}$$

Thus the incident flux can be written in terms of energy as:

$$incident\,flux = \frac{q^2 F m^* \mathrm{d}E_\perp}{\pi\hbar^3}. \tag{32}$$

The incident flux is used to determine the tunneling current by considering a volume A$\mathrm{d}x$, where $\mathrm{d}x$ is related to the total energy of the particle by $\mathrm{d}x$=$\mathrm{d}E$/qF. So finally we have a differential current of:

$$\mathrm{d}I = A\frac{qm^*}{\pi\hbar^3} T(E, V_{AB}(E)\, F(E, V)\, \mathrm{d}E_\perp \mathrm{d}E. \tag{33}$$

Finally Equation 33 is integrated to find the current density:

$$\mathrm{J_{2D}} = \frac{qm^*}{\pi\hbar^3} \int\int T(E, V_{AB}(E)\, F(E, V)\ \ \mathrm{d}E_\perp \mathrm{d}E. \tag{34}$$

As noted above, this is identical to the term found in [65] except for a factor of 2π.

4.3.5 The limits of integration

The last essential part of our tunneling model for calculating the tunneling current is a careful consideration of the limits of integration for Equation 34. For a typical TJ device, where the bands are crossed as a result of degenerate doping, the lowest possible energy for tunneling is the conduction band on the n-type side of the TJ. The highest possible energy is the valence band on the p-type side. To use the limits of integration seen on Equation 26, an assumption is made that all available states below the Fermi level are full, and all the states above the fermi level are empty. This is the zero temperature limit of the Fermi-Dirac distribution. With this assumption made, the lower limit of integration is simply the Fermi level, which is set as the reference voltage and is thus zero for both integrals. The outermost integral upper limit is simply qV, the applied bias across the tunnel junction. The inner integral upper limit is E, the total energy of the particle, which is also the differential term of the outer integral. The total energy of a particle can be decomposed into two components, one in the direction of tunneling, $E_\parallel$, and one perpendicular to the tunneling direction, $E_\perp$. Thus $E = E_\parallel + E_\perp$.This combination takes into consideration all

the combinations of $E_\perp$ and $E_\parallel$ which can give a total energy of E. It should be noted that we are assuming conservation of energy and perpendicular momentum for the tunneling process. Thus, while we may integrate over the differential $dE_\perp$, the tunneling probabilities remain functions of only the total energy, E.

If one wishes not to use the zero temperature approximation, then each energy level between the lowest point on the conduction band to the highest point on the valence band must be considered. Thus the lower limits of integration are simply the conduction band energy for the n-type side. The outermost integral limit is now the valence band on the p-type side, shifted down by qV_{AB}. The inner integral upper limit remains the same, E.

For reverse bias conditions in normal TJ devices, there is no theoretical limit to the magnitude of the reverse bias. In other words, the bias only serves to further cross the energy bands. In fact, even nominally doped pn junctions can result in favorable tunneling with a sufficiently high reverse bias. This is the operation principle of Zener diodes. However, if the reverse bias is set too high, then avalanche conditions are expected to prevail and become the dominant current mechanism. Forward bias is only permitted in highly doped p-n junctions if the bands are already crossed at equilibrium. A forward bias brings the edges of the conduction and valence band closer together until they become uncrossed and tunneling is no longer permitted. This gives the forward negative differential resistance characteristic of tunnel junction diodes. It should be noted that once the energy bands become uncrossed, for a particular bias, then no tunneling is possible and the current is set to zero. Such an evaluation is embedded in the code and not in the tunneling current equation.

The same arguments hold for the PTJ device considerations, except now we must additionally consider the quantum energy levels of the conduction and valence band. The first available crossing point for tunneling to occur is now tied to the location of the electron and hole ground states on either side of the junction. This is shown in Figure 37. Using the ground states as the limits of integration is appropriate as there are no electron states below the conduction band ground state to tunnel from and no states above the valence

band ground state for electrons to tunnel to.

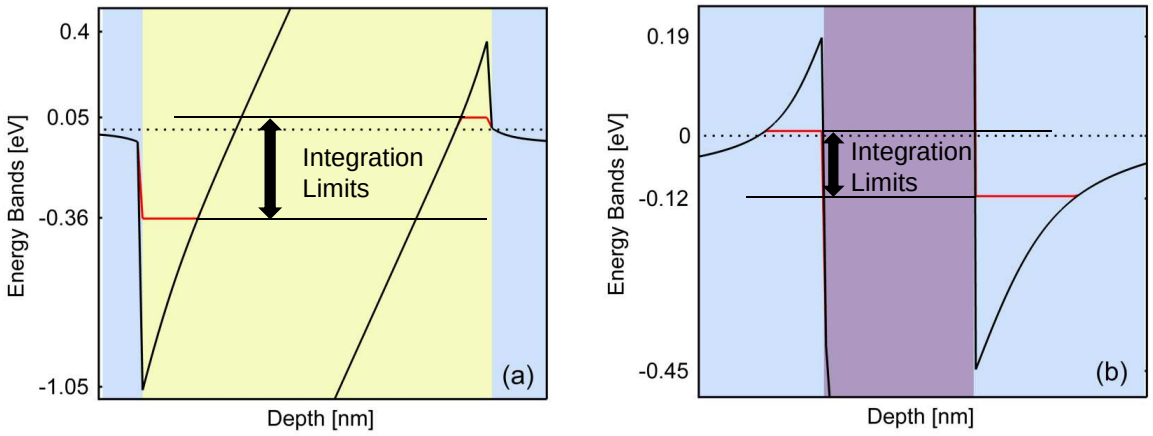

Figure 37: Devices from Figure 34, zoomed to show the tunneling area of concern. The limits of integration are determined by the ground state energy levels for both the InGaN and AlGaN PTJ designs. It is the formation of the 2DEG and 2DHG regions through polarization effects, rather than doping, that crosses the bands and permits tunneling.

The selection rule of simple quantum well devices is not expected to hold for PTJ devices. The selection rule states that only transitions between energy states with the same quantum number may occur, i.e., an electron in the ground state can only transition into the ground state of the holes. In essence an electron in the second quantum energy level of the conduction band cannot recombine with a hole in the first energy level of the valence band. Thus assuming that tunneling is performed by electrons, then the lower limit is the energy subband of interest, Ec_i, and the upper limit is always set to the ground state of the valence band. Thus after careful consideration of these points, our complete equation for tunneling is as follows:

$$J_{R2D} = \sum_{i=1}^{N} \Theta\left(Ev_0 - V - Ec_i\right) \frac{qm^*}{\pi\hbar^3} \int_{Ec_i}^{Ev_0} \int_{Ec_i}^{E} T_{QM}\left(E, V_{AB}\right) F\left(E, V_{AB}\right) \, dE_{\perp} dE \qquad (35)$$

Here Ev_0 and Ec_i are, respectively, the energy levels of the valence band ground state and the conduction band i^{th} quantum level. The heaviside function, $\Theta\left(Ev_0 - V - Ec_i\right)$, ensures that for a particular applied bias, V, we have a crossing of energy levels and thus

tunneling is possible. For this particular notation, the equilibrium Fermi energy level is considered as the reference voltage, therefore Ev_0 is typically positive and Ec_i is generally negative. We also assume that we are using the QM method for estimating the tunneling current in order to detect resonant tunneling conditions.

4.4 Resonant Tunneling Equation and MATLAB implementation

While Equation 35 is complete in that it takes care of each energy level in the QW regions, we will generally restrict our calculations for forward bias conditions to only account for the ground state conduction band energy level. This is a valid simplification due to the fact that the crossing of the second and higher energy state levels is very minimal in the best of conditions. Thus only a few millivolts would be needed to pinch off the current from higher energy states. This cannot be assumed for reverse bias conditions as it would underestimate the reverse bias. Increasing the reverse bias will not ever pinch off the current for any particular energy state. In fact, a reverse bias might cross higher energy energy states with the valence band ground state and enable current that was not possible before the applied bias.

The algorithm for evaluating Equation 35 is as follows. Silvaco's TCAD software is used to analyze the energy bands for each device. The details of the conduction and valence band profiles, polarization charges, and electron and hole bound state levels are simulated in Silvaco using a built in Schrodinger-Poisson solver. These parameters are exported into a text file and then imported into MATLAB.

In MATLAB the beginning and end of the entire tunneling region is selected. By this we simply mean that while a device might be several microns thick, with one or more p-n junctions, we simply select a region close to the tunnel junction and treat it separately from the rest of the device. The current through the PTJ region is in series with the remainder of the device. Thus for a multi-junction solar cell, for example, the current through each of the sub-cells would have to be equal to the current in the PTJ, and the voltage drop across the PTJ, V_{AB}, is a part of the globally-applied voltage on the entire device.

Regions that contain potential barriers and the depletion region are defined as indicated

above. In some cases, additional barriers are created that must be accounted for. For example, in a GaN-InGaN-GaN device, there is often a barrier in n-type GaN layer, caused by electrons diffusing easily into the neighboring InGaN region. This effect causes a depletion region to exist in the GaN layer next to the InGaN layer. For InGaN tunnel junction devices this n-type GaN region constitutes the first barrier region. While a similar effect will occur in the p-type GaN layer. The subsequent barrier is negligibly small and is therefore not treated as a barrier where tunneling is needed. Neglecting the valence band barrier is justified as we assume 70% of the bandgap is in the conduction band and only 30% in the valence band. The resulting barrier from such a small offset is generally only a few hundredths of an electron Volt.

Often the gridding used in Silvaco is too coarse and needs to be refined for accurate calculations. MATLAB's interp1 function is then used to add data points to the x-coordinate, and energy band vectors. While the interpolation function in MATLAB uses a linear approximation between points, which tends to destroy the step discontinuity at heterointerfaces, this is assumed to not introduce significant errors. Further to the point, however, is that it is highly unlikely that in physical devices such extreme junctions even exist.

Once the $F(E, V_{AB})$ and $T(E, V_{AB})$ are determined, a double Riemman sum is used to evaluate Equation 35.

4.5 GaN/AlN/GaN PTJ

The first experimental device using a PTJ was the n-p-n structure by Grundmann in 2005 [102]. However, in a full device such as this it is often difficult to determine exactly the contribution of the PTJ region to the current of the device. Therefore the first device we modeled was that of Simon et al., which demonstrated a single PTJ in reverse bias conditions [6]. This design was shown in Figure 34(b), and consists of an AlN layer sandwiched between a p-type GaN layer and an n-type GaN layer. The only parameter that varied in the study was the thickness of the AlN layer, which was 1.4, 2.8, 3.5, 4.3, and 5.0 nm thick for different samples.

While Simon et al., reported a calculated WKB transmission coefficient for a 0.5 V reverse bias, these results were not reproducible. A private communication with the author, John Simon, acknowledged the use of several fitting parameters in the reported probability curve and the use of an effective mass of .19 eV for the entire tunneling region. The 2.8 nm and 5.0 nm AlN layer experimental I-V curves published in the paper are compared with the results of Equation 35 with i, the number of eigenenergy states used, equal to 20 in Figure 38.

Both Equation 35 and the reported transmission probability in ref [6] indicate that no tunneling is likely for the 5.0 nm AlN layer sample. However, a strong current was reported which is therefore most likely due to trap assisted tunneling or other mechanisms. These same defects are expected to exist in the 2.8 nm AlN layer sample and could contribute to the difference between the simulation and experimental results seen in Figure 38.

In addition, the simulated current would increase if more eigenenergy levels were modeled. The limitation of 20 is due to constraints in the Silvaco output file. The contribution of the 1st and 20th energy levels are shown in Figure 39. Only the first two or three eigen states are below the Fermi level. The rest form a quasi-continuum where the energy levels are nearly identical. As the progressively higher energy levels lift above the Fermi level, the probability of an electron existing at that point decreases. Thus each energy state will

contribute progressively smaller currents to the overall tunneling current. No attempt at evaluating the limiting tunneling current was made.

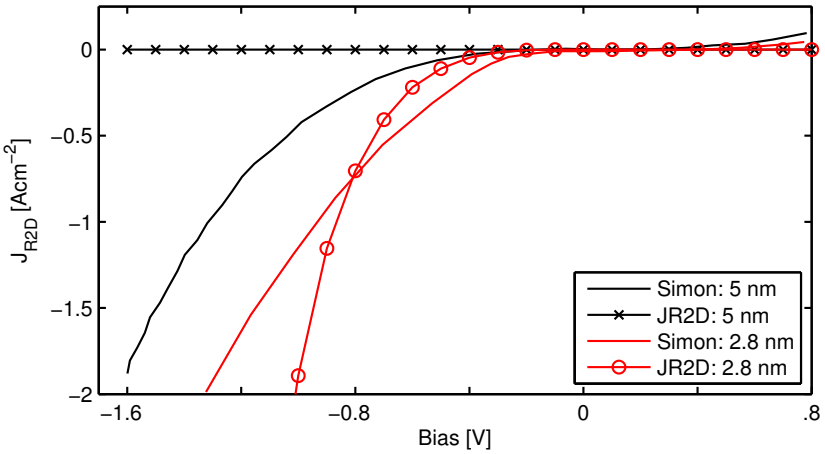

Figure 38: Using the first 20 eigenenergies for Equation 35 results in a tunneling current within an order of magnitude of the experimental result for the 2.8 nm AlN layer. Neither the WKB or QM method predict any significant current for the 5.0 nm layer, which indicates other mechanisms are likely responsible for the high current reported.

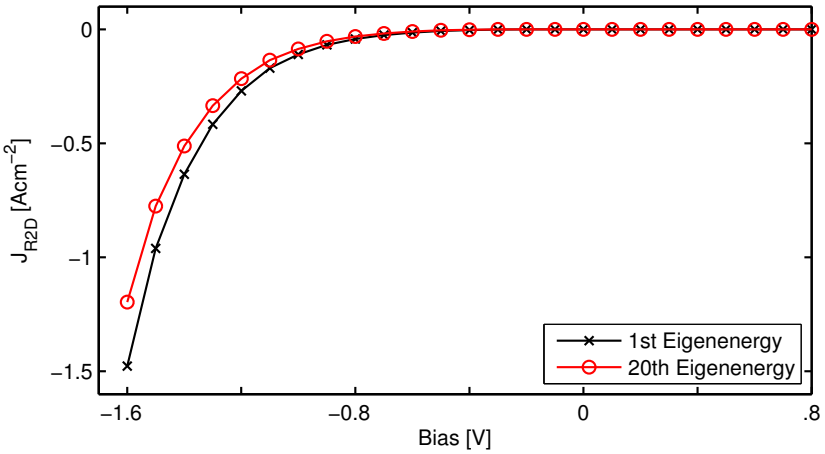

Figure 39: A comparison of the tunneling current contributions of the 1st and 20th energy states. The decrease in current for higher energy states is due to both a decreased band crossing and a lower probability of carriers existing at higher energies.

For the 2.8 nm configuration, the conduction band and valence band were engineered to become crossed. This is the optimal reverse bias condition as any applied bias will contribute directly to tunneling. However, no forward bias is possible as any applied bias will immediately uncross the bands and prohibit tunneling. The 3.5 nm case provides enough distance for the strong electric field to push the conduction and valence bands through the Fermi level, producing 2DEG and a 2DHG regions on the interfaces of AlN and GaN. The 3.5 nm case is also interesting in that at this thickness two quantum energy states exist in the 2DEG region. The forward bias current that either of these states contribute is indicated in Figure 40. While the current predicted is in the pico-amp range, and not useful or likely even detectable, the principle is useful for future design considerations. When Figure 40 is compared to Figure 39 it can be seen that for forward bias conditions only the ground state energy level is important in predicting the current. This is due to the fact that the second energy state is nearly uncrossed with the valence band at zero bias. Thus any applied bias will quickly uncross the higher energy levels and pinch off any current from them. This rapid current cutoff with applied bias is seen in Figure 40(b) where the current is zero for only 10 mV while for the ground state energy of Figure 40(a) displays current for higher than 100 mV.

The 5.0 nm AlN layer could possibly have a second or even third energy level as the 2DEG region formed is deeper than the 3.5 nm case. However, this slight advantage is negated by the difficulty of tunneling through such a substantial barrier, and no forward bias is predicted even for the ground state level.

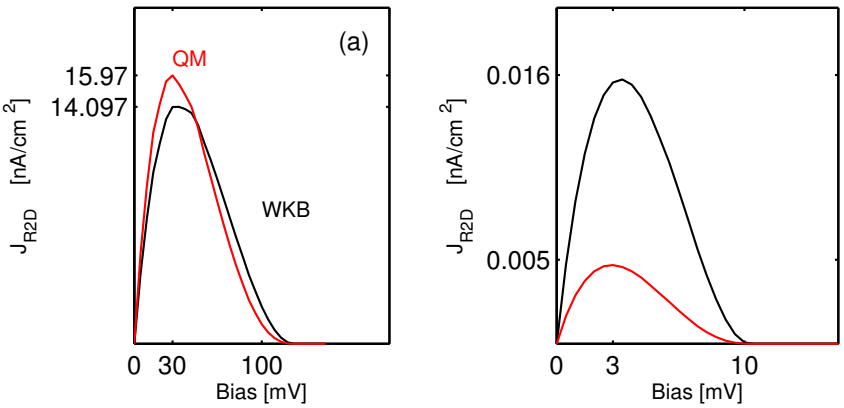

Figure 40: (a) The I-V curve for the ground state energy level. (b) The I-V curve for the second energy state level. This second energy state is barely crossed with the lowest ground state on the valence band side. Therefore the applied bias uncrosses this band very quickly resulting in very little current contribution to the PTJ.

4.6 GaN/InGaN/GaN PTJ

In 2011 Krishnamoorthy et al., created a PTJ using InGaN as the tunneling material. The smaller bandgap of InGaN as well as the lower effective mass, as low as $0.07m_0$ for InN, is very advantageous for tunneling. However, growing strained InGaN with high In is very difficult. Nevertheless, a 7 nm, $In_{.4}Ga_{.6}N$ layer was successfully grown of sufficient quality to demonstrate a peak forward bias current of 17.7 Acm^{-2} at a forward bias of 0.8 V. The large voltage for this current is attributed to the lack of a poor p-type contact on the device which added a schottky barrier to the device.

The I-V curve for this device is shown in Figure 41. The agreement of the experimental and the simulated I-V curves is very promising. The substantial forward bias of nearly 20 Acm^{-2} is more than sufficient for MJSC applications.

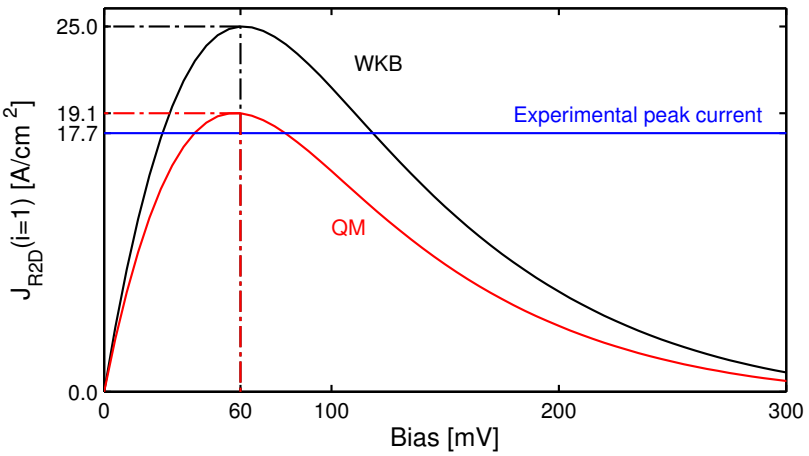

Figure 41: (a) The simulated I-V curve for the ground state compared to the experimentally achieved current. The discrepancy in the voltage scale is due to the presence of a schottky barrier as indicated above. This model predicts that only 0.06 V drops across the PTJ, the other 0.74 V is dropped across the series resistance of the GaN layers and contacts of the experimental device.

It should be noted that once again only the ground state level was used to create the I-V curve using Equation 35. The second energy level results in a smaller current as shown in Figure 42.

In addition to this forward bias PTJ device, Krishnamoorthy et al., demonstrated a

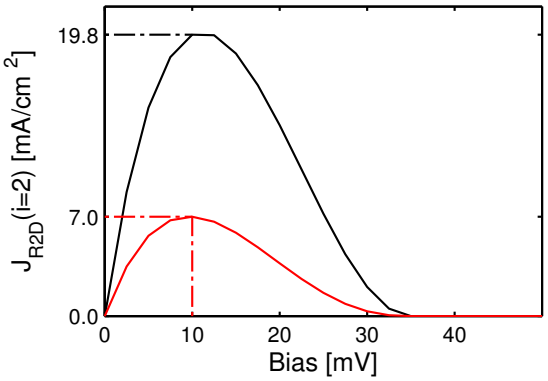

Figure 42: The simulated I-V curve for the second energy state. The second state is quickly pinched off with forward bias, preventing any significant contribution to the tunneling current.

clever way of bypassing the need for p-type contacting. The device configuration is shown in Figure 43. In this device an n-p-n configuration is used where the p-n component is a PTJ. In essence the goal is to allow for electrons to tunnel through the PTJ and recombine with carriers in the p-type region. If the tunneling rate is sufficiently high, then there is no need to create a p-type contact. As seen in ref [5], a p-type contact can add a substantial amount of series resistance to a device.

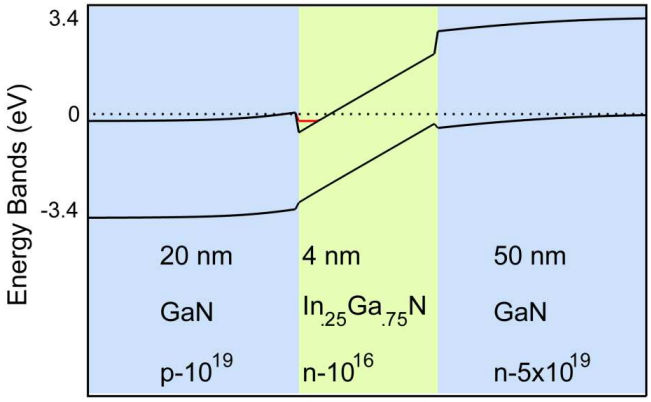

Figure 43: The PTJ design used in ref [7]. The 4 nm thickness of the InGaN is insufficient to cross the bands using only 25 percent In. The large tunneling current values reported in the paper are likely due to trap assisted tunneling.

The thickness of the $In_{.25}Ga_{.75}N$ layer is insufficient to adequately cross the conduction and valence bands. Therefore the crossing of the bands is assumed to originate from the

exceptionally high doping concentrations report. It was not indicated in the paper whether the high p-type doping of 10^{19} cm^{-3} was electrically activated carriers or simply the dopant concentration. Figure 43 assumes that all the carriers are activated.

Because the TJ in this device is not created as a result of PC effects, the current is simulated using Equation 26 and is shown in Figure 44. Krisnamoorthy et al., reported a tunnel junction resistance of $1.2x10^{-4}\Omega cm^2$ at 12 mV or reverse bias. The simulated current is almost zero for the same amount of reverse bias, which indicates that other means of tunneling account for the high current in the experimental device. Due to the very large doping levels reported, it is likely that the tunneling is trap assisted.

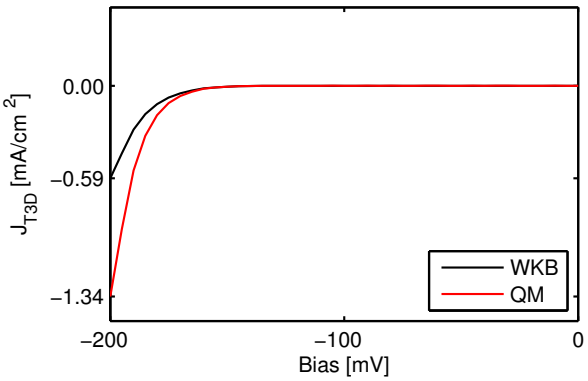

Figure 44: Simulated current using Equation 26 for the design in Figure 43. Due to the wide-bandgap of the materials involved, tunneling using either the QM or WKB methods predicts very little current for this device configuration.

4.7 PTJ designs for InGaN MJSCs

A simple solar cell is generally made with either a p-i-n or n-i-p configuration where the goal is to absorb photons in the intrinsic region. The carriers are then separated by the internal fields of the space charge region and eventually travel to the contacts, creating one of the only true current source devices in existence. A multi-junction solar cell uses several simple solar cells, each called a subcell, that can be connected either in series or in parallel. For MJSCs designed in series, the top subcell has the largest bandgap, to absorb higher

energy photons, and is designed to be as transparent as possible to allow lower energy photons to travel to the next subcell, where another range of photon energies are designed to be collected, and so forth, for each subcell. While it is conceivable to have two contacts on each subcell, in practice this is not possible. Therefore a two-terminal device, where only the top and bottom surfaces are contacted with metal, is needed and tunnel junctions provide the connections between each of the subcells. This places the currents in each subcell in series and as such, each subcell must be designed to have matching currents. In addition each tunnel junction should be able to provide for this same current with as little resistance as possible.

As mentioned above, the photo-generated current in solar cells is created by the separation of charges by the electric field of the pn junction; this is the mechanism behind drift current in pn junctions. This photo-generated current is the short circuit current, J_{SC} and is one of the two characteristic values of solar cells. When the solar cell is attached to an external resistance, called the load, a positive voltage is established on the contacts of the solar cell. The load is generally a battery or some other device. This places the pn junction of the solar cell in forward bias and the short circuit current is eventually matched by the diffusion current mechanism of the solar cell. This occurs at the voltage, V_{OC}, the open circuit voltage when the net current flowing through the solar cell is zero. For the operating voltage of the solar cell, which is less than V_{OC}, the current is negative, meaning that the solar cell is essentially operating as if it is in reverse bias. Therefore, the TJ regions, which have opposite polarities compared to the subcells, must be able to support a forward bias current. So, while the reverse biased TJ current reported in [7] provides exceptionally low resistances, for multi-junction solar cell applications a forward bias PTJ is needed. The only PTJ device which has demonstrated significant forward bias PTJ current is in Ref. [5]. This device consists of a strained InGaN layer and was simulated in the previous section.

A two-junction solar cell device will be studied in this paper. The top subcell will have a 150 nm $In_{.08}Ga_{.92}N$ absorption layer and the bottom subcell will have a 59 nm

$In_{.20}Ga_{.80}N$ absorption layer, both layers are considered to be unintentionally n-type doped at 10^{16} cm^{-3}. The thicknesses of the InGaN absorption layers were chosen to be current matched at 1.62 $mAcm^{-2}$ under AM0 illumination. The relatively low In incorporation used is consistent with current MOCVD growth limitations, and does not correspond to an optimal two-junction solar cell design. The absorption of sunlight in the InGaN layers was modeled after [52].

The remainder of this chapter deals with the use of PTJ designs to create viable MJSC designs. The PTJ region requires a highly strained, typically with less than 10% relaxation, InGaN or AlGaN layer. The use of AlGaN or InGaN as the tunnel junction material and the amount of strain in the InGaN absorption layers collectively determine if a p-type layer or n-type layer is used as the surface layer of the device. A p-type surface device will be referred to as a pin configuration and an n-type as a nip. The remainder of this chapter is as follows. The first section will discuss MJSCs where unstrained InGaN absorption regions are used. This will allow for a strained InGaN PTJ region to be used. The next section will show that for strained InGaN absorption regions, no possible configuration of the InGaN PTJ region will allow for a MJSC. The third section will discuss the design of an AlGaN layer as the material of choice for the PTJ. Finally, the use of a double barrier AlGaN PTJ is shown to enable resonant-tunneling in order to increase tunneling current to help offset the inherent difficulties of tunneling through AlN regions. This design is examined to optimize tunneling.

4.7.1 InGaN PTJ for relaxed absorption layers

The design consisting of unstrained InGaN absorption layers with a strained InGaN PTJ region is shown in Figure 45. A GaN substrate is used and the contacts are assumed to be ohmic. The doping levels and thicknesses of each layer is shown. The inset is focused on the PTJ region and indicated the formation of the 2DEG and 2DHG regions resulting from the strong PCs. The PTJ has the same current as the device in Figure 41. This current is

included for convenience. The simulated current for the QM method peaks at 19.1 Acm^{-2}, which slightly overestimates the experimental peak of 17.7 Acm^{-2}. It should be noted that no extra fitting parameters are needed for this curve. While the peak current provides a rough estimation of the maximum current achievable with the PTJ, for the purposes of a solar cell the key figure is the resistance at 1.62 $mAcm^{-}2$ for 1 sun illumination and 1.62 $Acm-^{2}$ for concentrated 1000 sun illumination. These values were calculated to be 1.4 mΩ for both 1 sun and concentrated illumination. Due to the low series resistance of the PTJ, this design is well suited for concentrated photovoltaic operation.

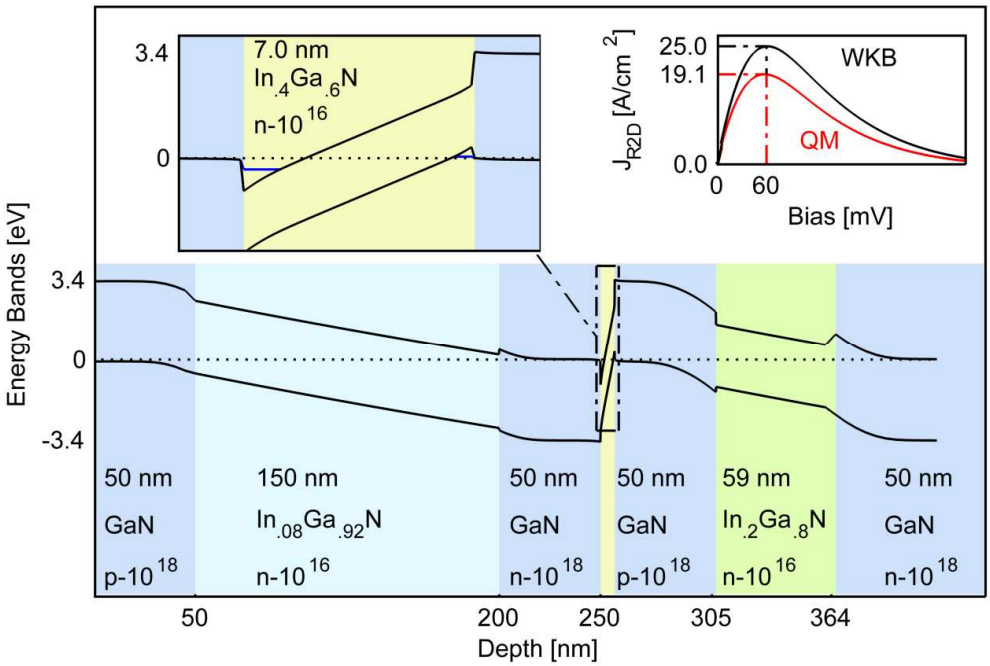

Figure 45: A MJSC design using the 7.0 nm $In_{.40}Ga_{.60}N$ PTJ reported in [5]. The PTJ has a series resistance of less than 1.2 mΩ for 1000x AM0 concentration.

4.7.2 InGaN PTJ for strained absorption layers

For these devices we have assumed that the InGaN absorption regions are 100% relaxed. As was shown in Figure 20, with even as much as 20% strain, the polarization effects of InGaN can drastically reduce the conversion efficiency of pin devices [27, 92]. However,

for MJSC devices, the use of a InGaN PTJs prohibits the solution of switching from a pin to a nip design as indicated in [55]. This is clearly seen in Figure 46. The electric field in the PTJ must be opposite of that formed in the subcell absorption regions. As the polarization vectors in all three strained InGaN layers align, and the fact that the polarization electric fields are larger than fields created by doping schemes, there is no configuration utilizing an InGaN PTJ layer that will work with strained InGaN absorption regions. Thus InGaN PTJ constrains the use of a pin configuration with greater than 80% relaxation in the InGaN absorption regions. While current growth techniques are incapable of growing strained InGaN layers thicker than 100 nm, with high In incorporation, this can eventually become a problem as growth techniques improve. In other words, even if thick, high-quality layers, which are generally associated with low levels of relaxation, were possible, then devices would have to include either graded heterointerfaces, purposely grow relaxed layers, or come up with some other method for reducing the PCs so that a pin configuration would become possible.

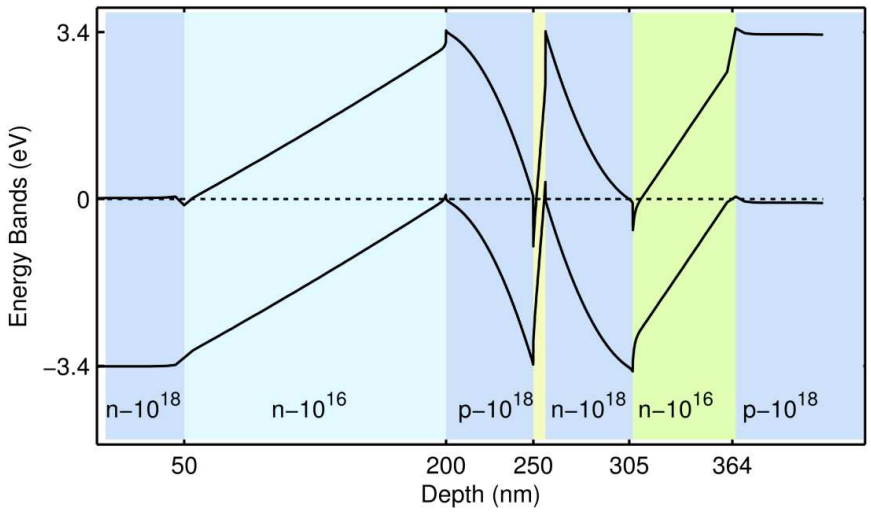

Figure 46: Utilizing an nip configuration for the same device as shown in Figure 45. Using strained InGaN absorption layers, in this case 100% strained, is incompatible with an InGaN PTJ region as the electric fields align in the same direction. The PTJ must utilize an electric field anti-parallel to those formed by the subcells pn junctions.

4.7.3 Single AlN layer PTJ for low In InGaN MJSC designs

The quality of InGaN absorption region can improve if the layers can be grown relaxation-free [37]. As indicated above InGaN cannot be used for the PTJ as the electric fields need to be anti-parallel. The polarization vectors in AlGaN layers strained on GaN are opposite in sign compared to those of InGaN strained on GaN. Therefore AlGaN would be a suitable candidate for a MJSC for strained InGaN absorption regions. However, as was shown in Figure 40, a very insignificant forward tunneling current is available for AlN on GaN. By simply removing the GaN layers on either side of the PTJ of Figure 45 we can utilize the higher PC developed on the InGaN absorption regions to decrease the thickness of the AlN region needed to cross the conduction and valence bands. This design in shown in Figure 47. Decreasing the AlN thickness is critical as the tunneling probability reduces by nearly an order of magnitude for each additional 1 nm of thickness.

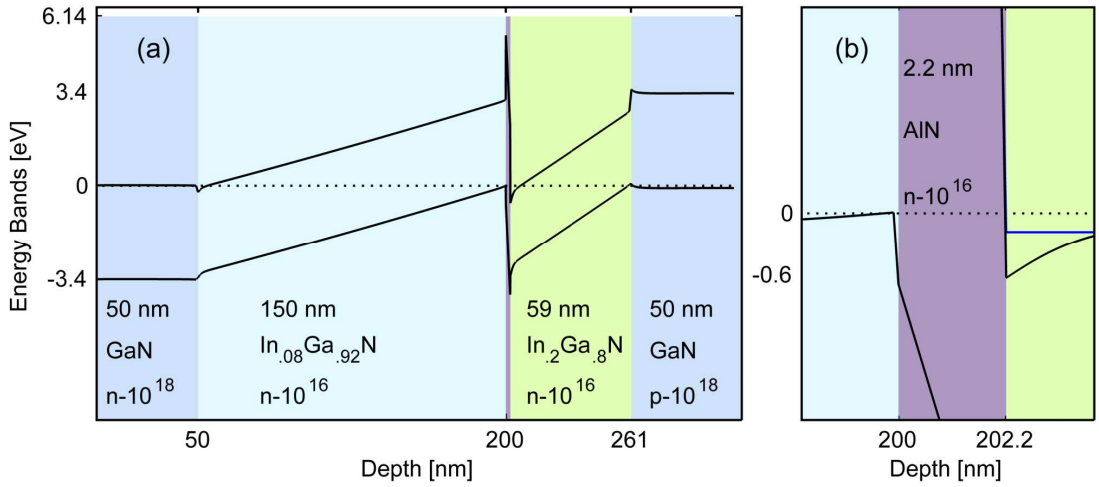

Figure 47: AlN for a MJSC design. The InGaN layers are assumed to be 100% strained. The high polarization induced sheet charge at the AlN/InGaN interfaces alleviates the need for n-type or p-type GaN layers to create the charge separation fields.

The AlN layer thickness was varied from 16 to 30 angstroms in 2 angstrom increments. The maximum current was found using a 2.2 nm thick AlN region. As indicated in Figure 48 this device is not able to produce the current needed for even 1 sun illumination.

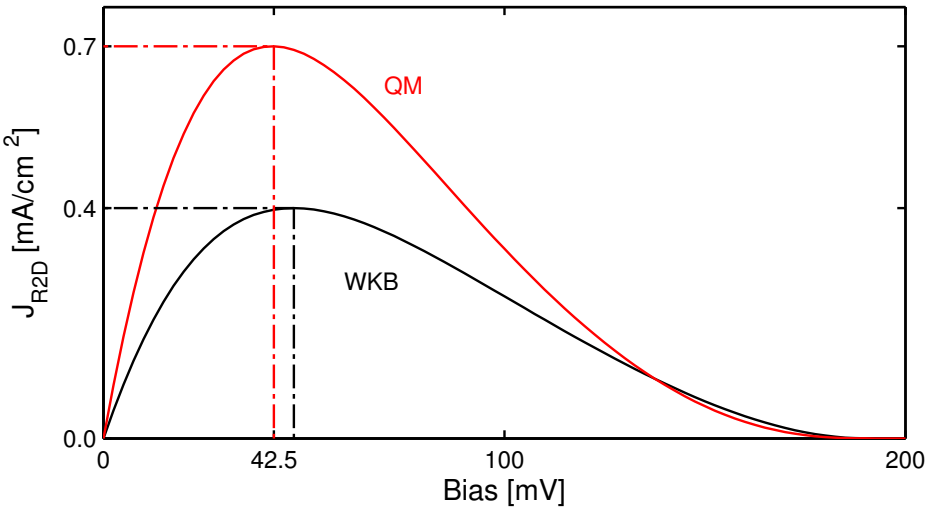

Figure 48: The I-V curve corresponding to a 2.2 nm AlN PTJ region for the device in Figure 47. The maximum current is insufficient for the device design and will limit the current through the subcells to a maximum of 500 mAcm^{-2}.

4.7.4 Resonant AlN/InGaN/AlGaN double barrier PTJ for low In InGaN MJSC designs

The design can be improved by adding a second AlGaN layer within a few nanometers of the AlN barrier. This second barrier allows for the resonant tunneling possibility as discussed in section 4.2.1. If InGaN is used to separate the AlGaN and AlN layer, resonant tunneling may occur. The AlN layer is the primary layer for crossing the conduction and valence band and therefore needs to have a high Al content. It should be noted that the ordering of the AlN and AlGaN layer is important as shown in Figure 49.

In essence, the AlN layer is primarily responsible for crossing the bands, as such, the interband tunneling occurs through the AlN layer. For strained InGaN layers, an nip structure is necessary. The p-type side of the device is therefore on the bottom of each subcell. If the AlN layer is grown on the bottom of a particular subcell, then the bottom of the AlN layer will be n-type, the conduction band is closer to that Fermi level. The InGaN interlayer and subsequent AlGaN layer will have conduction bands closer to the Fermi level and the

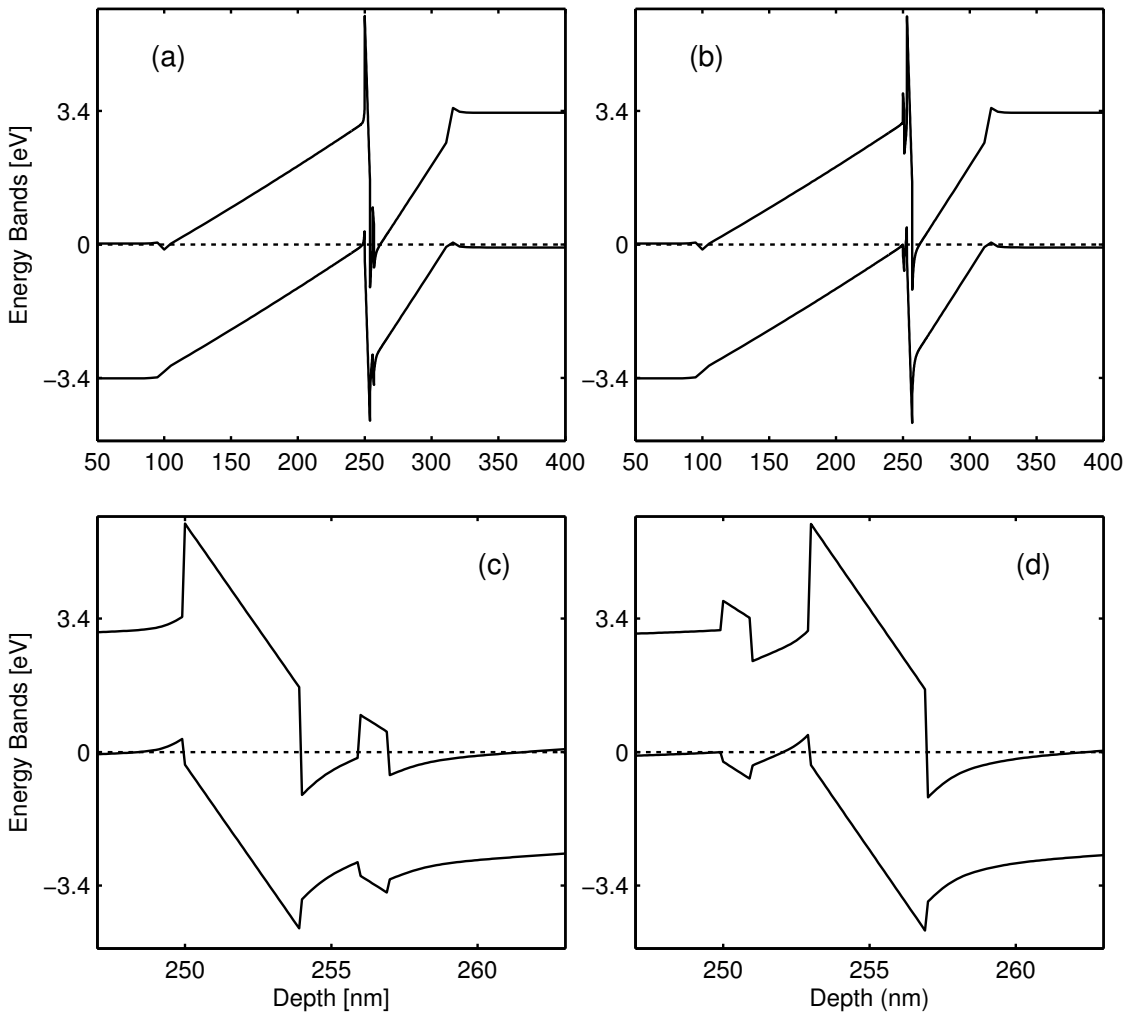

Figure 49: The location of the AlN layer, which is responsible for crossing the energy bands, and the second barrier is important. Either placing the AlN closer to the surface or closer to the substrate appears to correctly cross the energy bands as needed. (a) The AlN layer is closer to the surface of the MJSC. (b) The AlN layer is closer to the bottom of the the MJSC. (c) For the AlN layer on top, the tunneling particle through both the $Al_{.3}Ga_{.7}N$ and AlN barriers is an electron. (d) For the AlN layer on the bottom, the AlN tunneling particle is an electron. However, for the $Al_{.3}Ga_{.7}N$ layer, the tunneling particle is a hole, which will both decrease the tunneling probability as well as eliminate the possibility of resonant tunneling.

overall tunneling through these layers will be that of an electron. If the AlN is placed on the top of a subcell, then the top of the AlN layer will be p-type as the valence band is closer to the Fermi level. In this situation, the subsequent InGaN and AlGaN PTJ layers will have valence bands closer to the Fermi level and tunneling will be primarily due to holes. As the hole effective mass is as much as five times or more larger than the effective mass of electrons, the tunneling probability will be drastically reduced.

With the ordering of the AlN and AlGaN layers established, the PTJ is designed as shown in Figure 50. Thus the overall MJSC design is identical to that of Figure 47, except that the single AlN barrier has been replaced by an AlN/InGaN/AlGaN configuration. A gamut of simulation parameters were varied in order to find an optimal configuration. These parameters include: the thickness and In content of the InGaN layer between the AlN layer and the AlGaN layer, the thickness of the AlN layer, and the thickness and content of the AlGaN layer. The polarization was assumed to be 100% strained in all cases.

The optimal configuration simulated was as follows. The AlN layer was 2.2 nm thick, which was the same as the single barrier design above. This is expected because we need the AlN layer to cross the energy bands and yet be as thin as possible to allow for more tunneling. The InGaN interlayer was set to have a 1.5 nm thickness with 25% In content. Finally the AlGaN layer was set to have 30% Al and was 1 nm thick.

The current predicted using Equation 35 is shown in Figure 51. The QM method predicts a resonant current resulting from the double barrier configuration. The triangular shape of Figure 51 is a well documented result of resonant tunnel diodes as seen is several experimental and theoretical works [108–111]. Additionally the magnitude of the QM method is nearly 3000 times larger than the current predicted using the WKB method, which is another indicator of resonant tunneling effects. With a series resistance of only 4.6 $m\Omega cm^2$ and a maximum peak current of almost 12 mAcm−2 this configuration would sustain a 7 sun current of 11.4 $mAcm^{-2}$ with less than a 50 mV drop across the PTJ.

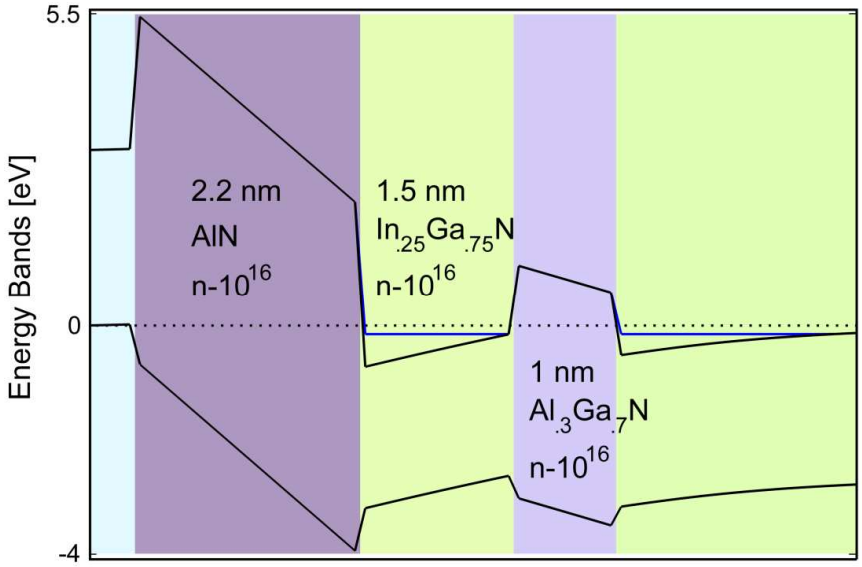

Figure 50: Resonant PTJ design using a double barrier configuration. The InGaN interlayer In content is slightly higher than the InGaN absorption regions on either side of the PTJ. The AlN layer is 2.2 nm, which is the thinnest possible thickness that will cross the energy bands.

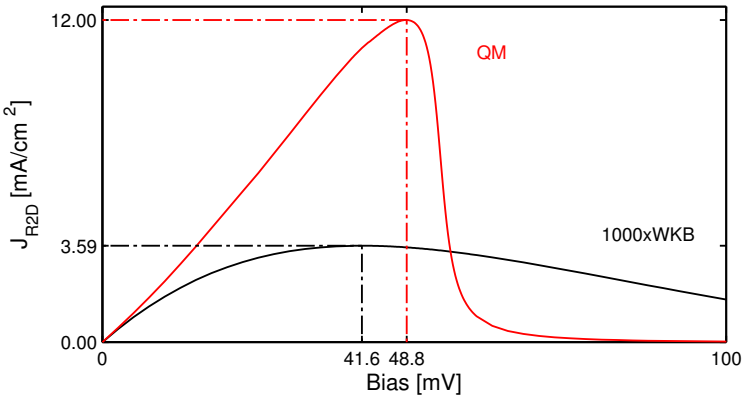

Figure 51: Resonant tunneling through the PTJ design of Figure 50. The peak resonant current is 11.9 mAcm^{-}3, which is almost 24 times as large as the single barrier design. The 4.6 mΩcm^2 series resistance of the PTJ is able to support up to 7 sun illumination. The triangular shape of the I-V curve is characteristic of resonant tunnel diodes. The WKB current is also shown here, magnified 1000 times, and is another indicator that the current is due to resonant effects of the double barrier design.

4.7.5 Single AlN layer PTJ for high In InGaN MJSC designs

While the designs and I-V curves of the previous section are instructional, they are not the optimal configuration for a multi-junction solar cell design. For a 4 subcell device the topmost subcells should have a bandgap of approximately 2.48 and 1.68 eVs, which correspond to a 25% In and 51% In InGaN layers respectively. While it is understood that this is not currently technologically feasible, it is the underlying push behind InGaN solar cell research to make this possible in the future.

A single barrier design was first modeled in order to obtain the minimum thickness needed for the AlN layer. All layers are assumed to be 100% strained on GaN. Due to the larger In incorporation, and the smaller bandgap of the InGaN layers involved, the amount of AlN thickness needed is reduced by nearly a full nanometer as seen in Figure 52. This alone greatly increases the tunneling probability of this device as seen by the current in Figure 53. This design has a series resistance of 7.0 $m\Omega cm^2$ at 1.62 $mAcm-2$ and a series resistance of 11.8 $m\Omega cm^2$ at the peak current of 6.8 Acm^{-2}.

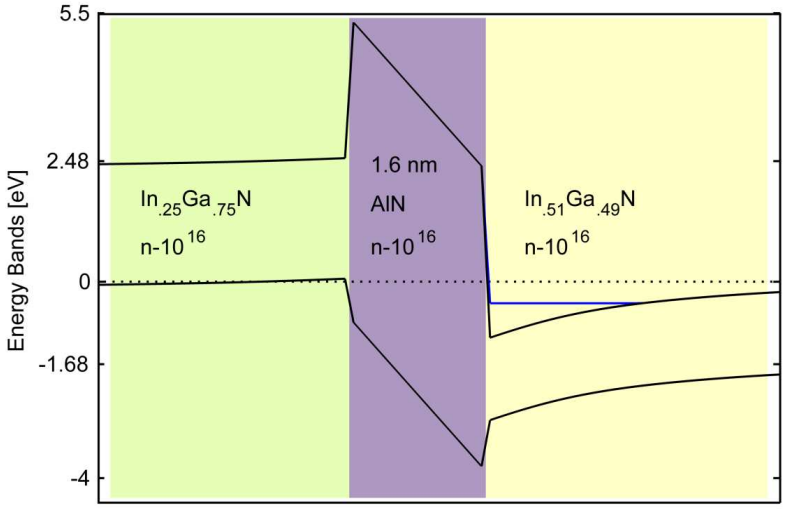

Figure 52: A single barrier PTJ for a multi-junction solar cell consisting of $In_{.25}Ga_{.75}$ and $In_{.51}Ga_{.49}N$ for the top and bottom subcells, respectively. Due to the strong PC charges from the 100% strained layers, only 1.6 nm of AlN is needed to cross the conduction and valence bands.

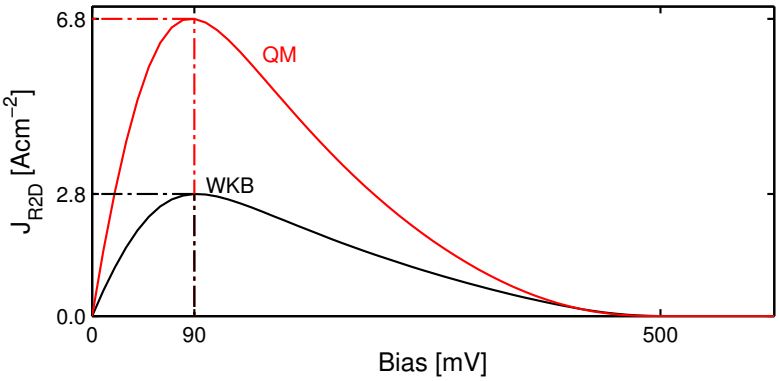

Figure 53: The I-V curve predicted for the device in Figure 52.

4.7.6 Resonant AlN/InGaN/AlGaN double barrier PTJ for high In InGaN MJSC designsn

Once again, the device design can be improved by using the AlN/InGaN/AlGaN resonant PTJ structure. The layer compositions and thicknesses were varied as before. A promising design is shown in Figure 54. In this design a 46% In InGaN layer, 1.5 nm thick, is sandwiched between a 1.5 nm AlN layer and a 1.0 nm $Al_xGa_{1-x}N$ layer with x=.3. With 100% strain for all the layers involved, Equation 35 was used to predict the I-V curve shown in Figure 55.

The series resistance of this device is 0.33 mΩcm^2 which is 21 times lower than the single barrier design. Furthermore, this resistance is nearly constant while the voltage increases and is only 0.4 mΩcm^2 for a current of 104.1 Acm−2.

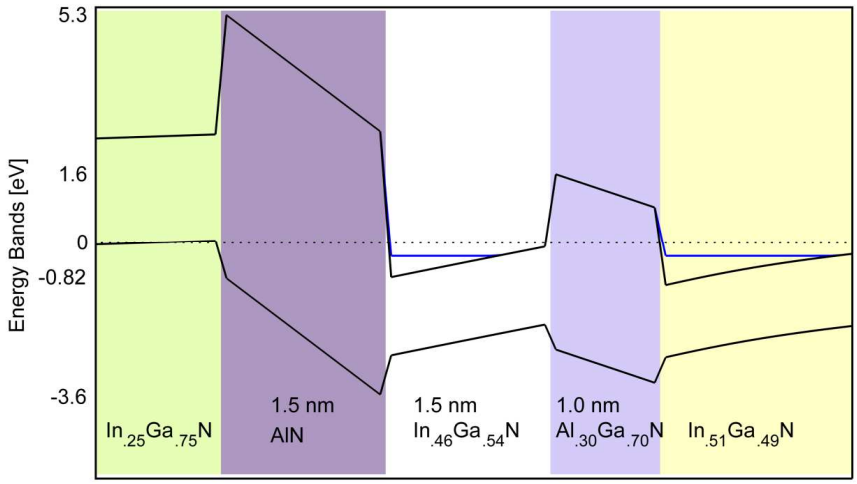

Figure 54: A double barrier PTJ for a multi-junction solar cell consisting of an $In_{.25}Ga_{.75}$ top subcell and an $In_{.51}Ga_{.49}N$ bottom subcell. Due to the strong PC charges from the 100% strained layers, only 1.5 nm of AlN is needed to cross the conduction and valence bands.

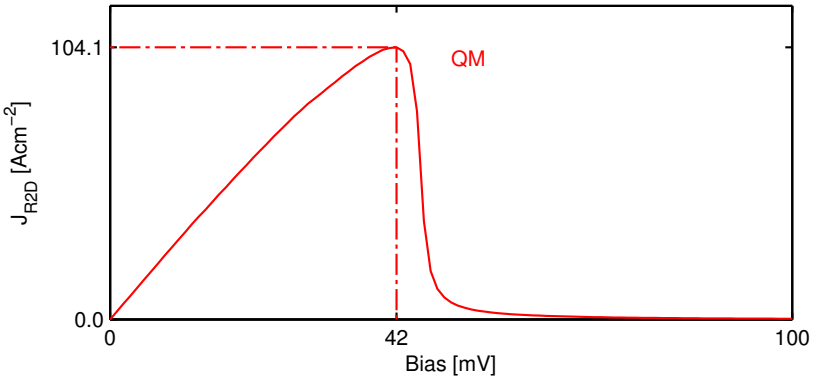

Figure 55: The I-V curve for the PTJ of Figure 54. The triangular shape predicted by the QM method is indicative of a strong resonant tunneling effect.

CHAPTER 5

CONCLUSION

The strong polarization charges of the III-N provide an alternative design parameter for semiconductor devices. With careful design these PCs can enable increased device performance and reliability.

This study has shown how BGaN back-barriers can tightly confine carriers to the high mobility GaN channel region in HEMT devices. Simulations show that electrons can be confined to within 17 nm of the AlGaN/GaN interface using a 50 nm $B_{.01}Ga_{.99}N$ back-barrier and a GaN channel width of 30 nm. It was also shown that MQW designs are possible that would allow for thinner interlayers of BGaN to be used to help alleviate growth issues if thicker layers prove difficult to grow. This design confines carriers to a region comparable to that of the current state-of-the-art InGaN back-barrier design [90, 91].

It has also been demonstrated that PCs can be used to create active regions in solar cells. The space charge regions typically produced with careful planning of dopants can be created with polarization charges. These designs are remarkably robust and show independence from the thickness and doping levels of the p- and n-doped layers. The minimum thickness, d_{min}, of the InGaN layer to reach maximum V_{oc} is predicted, delineating the regime where electrostatics are controlled by PCs.

The semibulk method was created as a means to increase InGaN material quality. Using GaN can substantially decrease efficiency for solar cell applications if the GaN layers are strained and thicker than 2.0 nms. However, the device conversion efficiencty is decreased less than 10% as long as the GaN layers are ≤ 1 nm thick and $\varphi \leq 0.5$.

Finally polarization effects can be used to create tunnel junctions that are currently impossible due to the inability to create p-doped layers of sufficiently high concentrations. A mathematical model for predicting the current through PTJ devices was developed. This model successfully predicted the current shown in Ref. [5].

Multi-junction solar cells can become competitive with Si-based solar cells when used with solar concentrator arrays. By focusing more sunlight onto the device, the surface area of the device can be reduced, thus reducing cost. In order to accomplish this the solar cell must be able to sustain the increased photo-generated current. For AM1 sunlight, a 2.48 eV bandgap has a theoretical maximum current of 7 $mAcm^{-2}$. By using a double barrier design the PTJ can take advantage of resonant tunneling effects to achieve higher currents with lower resistances than otherwise allowed. The resonant configuration of Figure 54 will support more than 1000xAM0 sunlight illumination.

This work has demonstrated an mathematical model for predicting tunneling current that agrees very well with experimental I-V curves. The resonant PTJ design introduced is provides an avenue for producing InGaN MJSCs that would not be possible otherwise.

5.1 Future work

This work has several potential research possibilities. Experimentally it is interesting to investigate the growth of the InGaN MJSC with 8% and 20% absorption regions to test the application of the resonant PTJ design in Figure 50. This design negates the need for high doping levels. The research would investigate the stability of the resonant PTJ with respect to AlN/InGaN/AlGaN growth constraints.

In addition, the thermal effects of multiple sun illumination on PTJs has not been explored. Heating affects device bandgaps, carrier mobilities, and many other properties. Future work would include a study of thermal effects on polarization sheet charge densities. Heating effects in solar cells is a common cause of decreased efficiency in performance. As the PCs are responsible for the creation of the PTJs, it is important that heating effects do not diminish the electric field strengths as this could cut off the tunneling current.

Another aspect of heating that has not been addressed is the nature of the resonant tunneling as the average carrier temperature increases. This would affect the Fermi statistics

and possibly alter the strength of the resonant tunneling. A study to determine if this is beneficial or detrimental to resonant tunneling would be very useful. Additionally, tunneling is expected to increase due to the decrease in the bandgab height as a result of heating.

It is possible that the strong electric fields of the PCs could lead to increased device performance in LEDs, photo-detectors, and many other devices. Other materials, such as ZnO and MgZnO, are also expected to greatly benefit from strong polarization charges.

REFERENCES

[1] I. Vurgaftman and J. R. Meyer, "Band parameters for nitrogen-containing semiconductors," *Journal of Applied Physics*, vol. 94, no. 6, p. 3675, 2003.

[2] A. Coelho, M. Adam, and H. Boudinov, "Distinguishing bulk traps and interface states in deep-level transient spectroscopy," *Journal of Physics D: Applied Physics*, vol. 44, no. 30, p. 305303, 2011.

[3] T. Palacios, A. Chakraborty, S. Heikman, S. Keller, S. P. DenBaars, and U. K. Mishra, "AlGaN/GaN high electron mobility transistors with InGaN back-barriers," *Electron Device Letters, IEEE*, vol. 27, no. 1, p. 13, 2006.

[4] V. Ravindran, M. Boucherit, A. Soltani, S. Gautier, T. Moudakir, J. Dickerson, P. L. Voss, M.-A. d. Forte-Poisson, J.-C. D. Jaeger, and A. Ougazzaden, "Dual-purpose BGaN layers on performance of nitride-based high electron mobility transistors," *Applied Physics Letters*, vol. 100, no. 24, p. 243503, 2012.

[5] S. Krishnamoorthy, P. S. Park, and S. Rajan, "Demonstration of forward inter-band tunneling in GaN by polarization engineering," *Applied Physics Letters*, vol. 99, no. 23, p. 233504, 2011.

[6] J. Simon, Z. Zhang, K. Goodman, H. Xing, T. Kosel, P. Fay, and D. Jena, "Polarization-induced zener tunnel junctions in wide-band-gap heterostructures," *Phys. Rev. Lett.*, vol. 103, p. 026801, 2009.

[7] S. Krishnamoorthy, F. Akyol, P. S. Park, and S. Rajan, "Low resistance gan/ingan/gan tunnel junctions," *Applied Physics Letters*, vol. 102, no. 11, p. 113503, 2013.

[8] H. Amano, M. Kito, K. Hiramatsu, and I. Akasaki, "P-type conduction in Mg-doped gan treated with low-energy electron beam irradiation (LEEBI)," *Japanese Journal of Applied Physics*, vol. 28, no. 12, p. L2112, 1989.

[9] G. Meneghesso, G. Verzellesi, F. Danesin, F. Rampazzo, F. Zanon, A. Tazzoli, M. Meneghini, and E. Zanoni, "Reliability of GaN high-electron-mobility transistors: State of the art and perspectives," *Ieee Transactions on Device and Materials Reliability*, vol. 8, no. 2, p. 332, 2008.

[10] Y. Wu, D. Kapolnek, J. Ibbetson, P. Parikh, B. Keller, and U. Mishra, "Very-high power density AlGaN/GaN HEMTs," *Electron Devices, IEEE Transactions on*, vol. 48, no. 3, p. 586, 2001.

[11] M. A. Green, K. Emery, Y. Hishikawa, W. Warta, and E. D. Dunlop, "Solar cell efficiency tables (version 39)," *Progress in Photovoltaics: Research and Applications*, vol. 20, no. 1, p. 12, 2012.

[12] J. Wu, W. Walukiewicz, W. Shan, K. M. Yu, J. W. Ager, S. X. Li, E. E. Haller, H. Lu, and W. J. Schaff, "Temperature dependence of the fundamental band gap of InN," *Journal of Applied Physics*, vol. 94, no. 7, p. 4457, 2003.

[13] A. Barnett, D. Kirkpatrick, C. Honsberg, D. Moore, M. Wanlass, K. Emery, R. Schwartz, D. Carlson, S. Bowden, D. Aiken, A. Gray, S. Kurtz, L. Kazmerski, M. Steiner, J. Gray, T. Davenport, R. Buelow, L. Takacs, N. Shatz, J. Bortz, O. Jani, K. Goossen, F. Kiamilev, A. Doolittle, I. Ferguson, B. Unger, G. Schmidt, E. Christensen, and D. Salzman, "Very high efficiency solar cell modules," *Progress in Photovoltaics: Research and Applications*, vol. 17, no. 1, p. 75, 2009.

[14] J. Wu, W. Walukiewicz, K. M. Yu, W. Shan, J. W. A. III, E. E. Haller, H. Lu, W. J. Schaff, W. K. Metzger, and S. Kurtz, "Superior radiation resistance of $In_{1-x}Ga_xN$ alloys: Full-solar-spectrum photovoltaic material system," *Journal of Applied Physics*, vol. 94, no. 10, p. 6477, 2003.

[15] D. Vanderbilt and R. D. King-Smith, "Electric polarization as a bulk quantity and its relation to surface charge," *Phys. Rev. B*, vol. 48, p. 4442, 1993.

[16] R. Resta, "Macroscopic polarization in crystalline dielectrics: the geometric phase approach," *Rev. Mod. Phys.*, vol. 66, p. 899, 1994.

[17] F. Bernardini, V. Fiorentini, and D. Vanderbilt, "Spontaneous polarization and piezoelectric constants of III-V nitrides," *Physical Review B*, vol. 56, no. 16, p. R10024, 1997.

[18] V. Fiorentini, F. Bernardini, and O. Ambacher, "Evidence for nonlinear macroscopic polarization in III-V nitride alloy heterostructures," *Applied Physics Letters*, vol. 80, no. 7, p. 1204, 2002.

[19] P. Boguslawski, E. L. Briggs, and J. Bernholc, "Native defects in gallium nitride," *Phys. Rev. B*, vol. 51, p. 17255, 1995.

[20] C. Wetzel, T. Suski, J. W. Ager Iii, E. R. Weber, E. E. Haller, S. Fischer, B. K. Meyer, R. J. Molnar, and P. Perlin, "Pressure induced deep gap state of oxygen in gan," *Physical Review Letters*, vol. 78, no. 20, p. 3923, 1997.

[21] P. Kozodoy, J. P. Ibbetson, H. Marchand, P. T. Fini, S. Keller, J. S. Speck, S. P. DenBaars, and U. K. Mishra, "Electrical characterization of GaN p-n junctions with and without threading dislocations," *Applied Physics Letters*, vol. 73, no. 7, p. 975, 1998.

[22] N. Faleev, B. Jampana, A. Pancholi, O. Jani, H. Yu, I. Ferguson, V. Stoleru, R. Opila, and C. Honsberg, "High quality InGaN for photovoltaic applications: Type and spatial distribution of crystalline defects and "phase" separation," in *Photovoltaic Specialists Conference, 2008. PVSC '08. 33rd IEEE*, 2008.

[23] I. Gorczyca, S. P. Lepkowski, T. Suski, N. E. Christensen, and A. Svane, "Influence of indium clustering on the band structure of semiconducting ternary and quaternary nitride alloys," *Physical Review B*, vol. 80, no. 7, p. 075202, 2009.

[24] K. Pantzas, Y. E. Gmili, J. Dickerson, S. Gautier, L. Largeau, O. Mauguin, G. Patriarche, S. Suresh, T. Moudakir, C. Bishop, A. Ahaitouf, T. Rivera, C. Tanguy, P. Voss, and A. Ougazzaden, "Reprinted from semibulk InGaN: A novel approach for thick, single phase, epitaxial InGaN layers grown by MOVPE," *Journal of Crystal Growth*, 2012. with permission from Elsevier.

[25] H. Wang, D. Jiang, U. Jahn, J. Zhu, D. Zhao, Z. Liu, S. Zhang, and H. Yang, "Cathodoluminescence study on in composition inhomogeneity of thick InGaN layer," *Thin Solid Films*, vol. 518, no. 17, p. 5028, 2010.

[26] K. Pantzas, G. Patriarche, G. Orsal, S. Gautier, T. Moudakir, M. Abid, V. Gorge, Z. Djebbour, P. L. Voss, and A. Ougazzaden, "Investigation of a relaxation mechanism specific to InGaN for improved movpe growth of nitride solar cell materials," *physica status solidi (a)*, vol. 209, no. 1, p. 25, 2012.

[27] J. J. Wierer, A. J. Fischer, and D. D. Koleske, "The impact of piezoelectric polarization and nonradiative recombination on the performance of (0001) face GaN/InGaN photovoltaic devices," *Applied Physics Letters*, vol. 96, no. 5, p. 051107, 2010.

[28] M. Lestrade, Z. Li, Y. Xiao, and Z. Li, "Modeling of polarization effects in InGaN pin solar cells," *Optical and quantum electronics*, vol. 42, no. 11, p. 699, 2011.

[29] M. Asif Khan, A. Bhattarai, J. N. Kuznia, and D. T. Olson, "High electron mobility transistor based on a GaN-$Al_xGa_{1-x}N$ heterojunction," *Applied Physics Letters*, vol. 63, no. 9, p. 1214, 1993.

[30] Y.-F. Wu, B. Keller, S. Keller, N. Nguyen, M. Le, C. Nguyen, T. Jenkins, L. Kehias, S. Denbaars, and U. Mishra, "Short channel AlGaN/GaN MODFET's with 50-GHz f_t and 1.7-w/mm output-power at 10 GHz," *Electron Device Letters, IEEE*, vol. 18, no. 9, p. 438, 1997.

[31] J. Redwing, M. Tischler, J. Flynn, S. Elhamri, M. Ahoujja, R. Newrock, and W. Mitchel, "Two-dimensional electron gas properties of AlGaN/GaN heterostructures grown on 6H-SiC and sapphire substrates," *Applied physics letters*, vol. 69, no. 7, p. 963, 1996.

[32] P. M. Asbeck, E. T. Yu, S. S. Lau, G. J. Sullivan, J. Van Hove, and J. Redwing, "Piezoelectric charge densities in AlGaN/GaN HFETs," *Electronics Letters*, vol. 33, no. 14, p. 1230, 1997.

[33] O. Ambacher, J. Smart, J. R. Shealy, N. G. Weimann, K. Chu, M. Murphy, W. J. Schaff, L. F. Eastman, R. Dimitrov, L. Wittmer, M. Stutzmann, W. Rieger, and J. Hilsenbeck, "Two-dimensional electron gases induced by spontaneous and piezoelectric polarization charges in n- and ga-face AlGaN/GaN heterostructures," *Journal of Applied Physics*, vol. 85, no. 6, p. 3222, 1999.

[34] S. J. Pearton, J. C. Zolper, R. J. Shul, and F. Ren, "GaN: Processing, defects, and devices," *Journal of Applied Physics*, vol. 86, no. 1, p. 1, 1999.

[35] O. Ambacher, J. Majewski, C. Miskys, A. Link, M. Hermann, M. Eickhoff, M. Stutzmann, F. Bernardini, V. Fiorentini, V. Tilak, B. Schaff, and L. F. Eastman, "Pyroelectric properties of Al(In)GaN/GaN hetero- and quantum well structures," *Journal of Physics: Condensed Matter*, vol. 14, no. 13, p. 3399, 2002.

[36] O. Jani, I. Ferguson, C. Honsberg, and S. Kurtz, "Design and characterization of GaN/InGaN solar cells," *Applied Physics Letters*, vol. 91, no. 13, p. 132117, 2007.

[37] C. J. Neufeld, N. G. Toledo, S. C. Cruz, M. Iza, S. P. DenBaars, and U. K. Mishra, "High quantum efficiency InGaN/GaN solar cells with 2.95 eV band gap," *Applied Physics Letters*, vol. 93, no. 14, p. 143502, 2008.

[38] X. Zheng, R.-H. Horng, D.-S. Wuu, M.-T. Chu, W.-Y. Liao, M.-H. Wu, R.-M. Lin, and Y.-C. Lu, "High-quality InGaN/GaN heterojunctions and their photovoltaic effects," *Applied Physics Letters*, vol. 93, no. 26, p. 261108, 2008.

[39] X.-m. Cai, S.-w. Zeng, and B.-p. Zhang, "Fabrication and characterization of InGaN p-i-n homojunction solar cell," *Applied Physics Letters*, vol. 95, no. 17, p. 173504, 2009.

[40] R. Dahal, B. Pantha, J. Li, J. Y. Lin, and H. X. Jiang, "InGaN/GaN multiple quantum well solar cells with long operating wavelengths," *Applied Physics Letters*, vol. 94, no. 6, p. 063505, 2009.

[41] E. Matioli, C. Neufeld, M. Iza, S. C. Cruz, A. A. Al-Heji, X. Chen, R. M. Farrell, S. Keller, S. DenBaars, U. Mishra, S. Nakamura, J. Speck, and C. Weisbuch, "High internal and external quantum efficiency InGaN/GaN solar cells," *Applied Physics Letters*, vol. 98, no. 2, p. 021102, 2011.

[42] J.-Y. Chang and Y.-K. Kuo, "Numerical study on the influence of piezoelectric polarization on the performance of p-on-n (0001)-face GaN/InGaN p-i-n solar cells," *Electron Device Letters, IEEE*, vol. 32, no. 7, p. 937, 2011.

[43] J. Simon, V. Protasenko, C. Lian, H. Xing, and D. Jena, "Polarization-induced hole doping in wide-band-gap uniaxial semiconductor heterostructures," *Science*, vol. 327, no. 5961, p. 60, 2010.

[44] P. Lefebvre, A. Morel, M. Gallart, T. Taliercio, J. Allegre, B. Gil, H. Mathieu, B. Damilano, N. Grandjean, and J. Massies, "High internal electric field in a graded-width InGaN/GaN quantum well: Accurate determination by time-resolved photoluminescence spectroscopy," *Applied Physics Letters*, vol. 78, no. 9, p. 1252, 2001.

[45] S. Krishnamoorthy, D. N. Nath, F. Akyol, P. S. Park, M. Esposto, and S. Rajan, "Polarization-engineered GaN/InGaN/GaN tunnel diodes," *Applied Physics Letters*, vol. 97, no. 20, p. 203502, 2010.

[46] V. Bougrov, M. E. Levinshtein, S. L. Rumyantsev, and A. Zubrilov, *Properties of advanced semiconductor materials : GaN, AlN, InN, BN, SiC, SiGe*. New York: Wiley, 2001.

[47] T. Inushima, M. Higashiwaki, and T. Matsui, "Optical properties of Si-doped InN grown on sapphire (0001)," *Physical Review B*, vol. 68, no. 23, p. 235204, 2003.

[48] K. Shimada, "First-principles determination of piezoelectric stress and strain constants of wurtzite III-V nitrides," *Japanese Journal of Applied Physics*, vol. 45, no. No. 12, p. L358, 2006.

[49] J. Wu, W. Walukiewicz, K. M. Yu, J. W. Ager, E. E. Haller, H. Lu, and W. J. Schaff, "Small band gap bowing in $In_{1-x}Ga_xN$ alloys," *Applied Physics Letters*, vol. 80, no. 25, p. 4741, 2002.

[50] A. Ougazzaden, S. Gautier, T. Moudakir, Z. Djebbour, Z. Lochner, S. Choi, H. J. Kim, J. H. Ryou, R. D. Dupuis, and A. A. Sirenko, "Bandgap bowing in BGaN thin films," *Applied Physics Letters*, vol. 93, no. 8, p. 083118, 2008.

[51] M. Feneberg and K. Thonke, "Polarization fields of III-nitrides grown in different crystal orientations," *J Phys Condens Matter*, vol. 19, no. 40, p. 403201, 2007.

[52] G. Brown, J. A. III, W. Walukiewicz, and J. Wu, "Finite element simulations of compositionally graded InGaN solar cells," *Solar Energy Materials and Solar Cells*, vol. 94, no. 3, p. 478, 2010.

[53] N. W. Ashcroft and N. D. Mermin, *Solid State Physics*. Philadelphia: Saunders College: Brooks Cole, 1976.

[54] R. M. Martin, "Piezoelectricity," *Phys. Rev. B*, vol. 5, p. 1607, 1972.

[55] J. R. Dickerson, V. Ravindran, T. Moudakir, S. Gautier, P. L. Voss, and A. Ougazzaden, "A study of BGaN back-barriers for AlGaN/GaN hemts," *The European Physical Journal - Applied Physics*, vol. 60, no. 03, 2012. Reprinted with permission.

[56] C. Wood and J. Debdeep, *Polarization Effects in Semiconductors: From Ab Initio Theory to Device Applications*. Boston, MA: Springer-Verlag US, 2008.

[57] F. Bernardini and V. Fiorentini, "Polarization fields in nitride nanostructures: 10 points to think about," *Applied Surface Science*, vol. 166, no. 14, p. 23, 2000.

[58] V. Fiorentini, F. Bernardini, F. Della Sala, A. Di Carlo, and P. Lugli, "Effects of macroscopic polarization in III-V nitride multiple quantum wells," *Physical Review B*, vol. 60, no. 12, p. 8849, 1999.

[59] B. K. Ridley, O. Ambacher, and F. E. Lester, "The polarization-induced electron gas in a heterostructure," *Semiconductor Science and Technology*, vol. 15, no. 3, p. 270, 2000.

[60] F. D. Sala, A. D. Carlo, P. Lugli, F. Bernardini, V. Fiorentini, R. Scholz, and J.-M. Jancu, "Free-carrier screening of polarization fields in wurtzite GaN/InGaN laser structures," *Applied Physics Letters*, vol. 74, no. 14, p. 2002, 1999.

[61] A. D. Carlo, F. D. Sala, P. Lugli, V. Fiorentini, and F. Bernardini, "Doping screening of polarization fields in nitride heterostructures," *Applied Physics Letters*, vol. 76, no. 26, p. 3950, 2000.

[62] A. Taflove and S. C. Hagness, *Computational Electrodynamics: The Finite-difference Time-domain Method. 3rd ed*. Boston: Artech House, 2005.

[63] R. F. Pierret, *Semiconductor Device Fundamentals*. Addison Wesley: Reading, Mass., 1996.

[64] S. M. Sze and K. K. Ng, *Physics of Semiconductor Devices 3rd ed.* Hoboken, N.J.: Wiley-Interscience, 2007.

[65] K. F. Brennan, *The Physics of Semiconductors: With Applications to Optoelectronic Devices*. Cambridge ; New York: Cambridge University Press, 1999.

[66] I. Tan, x, H, G. L. Snider, L. D. Chang, and E. L. Hu, "A self consistent solution of schrodinger-poisson equations using a nonuniform mesh," *Journal of Applied Physics*, vol. 68, no. 8, p. 4071, 1990.

[67] I. Silvaco, "Silvaco atlas user manual, 2012 available from www.silvaco.com," 2012.

[68] D. Lang, "Deep-level transient spectroscopy: A new method to characterize traps in semiconductors for $In_xGa_{1-x}N$," *Journal of Applied Physics*, vol. 45, no. 7, p. 3023, 1974.

[69] R. Mosca, E. Gombia, A. Passaseo, V. Tasco, M. Peroni, and P. Romanini, "Dlts characterization of silicon nitride passivated algan/gan heterostructures," *Superlattices and Microstructures*, vol. 36, no. 4, pp. 425–433, 2004.

[70] K. Yamasaki, M. Yoshida, and T. Sugano, "Deep level transient spectroscopy of bulk traps and interface states in si mos diodes," *Jpn. J. Appl. Phys.*, vol. 18, no. 1, pp. 113–122, 1979.

[71] T. Baghdadli, S. O. S. Hamady, S. Gautier, T. Moudakir, B. Benyoucef, and A. Ougazzaden, "Electrical and structural characterizations of BGaN thin films grown by metal-organic vapor-phase epitaxy," *physica status solidi (c)*, vol. 6, no. S2, p. S1029, 2009.

[72] D. S. Lee, X. Gao, S. P. Guo, D. Kopp, P. Fay, and T. Palacios, "300-GHz InAlN/GaN HEMTs with InGaN back barrier," *Ieee Electron Device Letters*, vol. 32, no. 11, p. 1525, 2011.

[73] J. B. Webb, H. Tang, S. Rolfe, and J. A. Bardwell, "Semi-insulating C-doped GaN and high-mobility AlGaN/GaN heterostructures grown by ammonia molecular beam epitaxy," *Applied Physics Letters*, vol. 75, no. 7, p. 953, 1999.

[74] S. Heikman, S. Keller, S. P. DenBaars, and U. K. Mishra, "Growth of Fe doped semi-insulating GaN by metalorganic chemical vapor deposition," *Applied Physics Letters*, vol. 81, no. 3, p. 439, 2002.

[75] Z. Y. Fan, J. Li, M. L. Nakarmi, J. Y. Lin, and H. X. Jiang, "AlGaN/GaN/AlN quantum-well field-effect transistors with highly resistive AlN epilayers," *Applied Physics Letters*, vol. 88, no. 7, p. 073513, 2006.

[76] C. Q. Chen, J. P. Zhang, V. Adivarahan, A. Koudymov, H. Fatima, G. Simin, J. Yang, and M. Asif Khan, "AlGaN/GaN/AlGaN double heterostructure for high-power III-N field-effect transistors," *Applied Physics Letters*, vol. 82, no. 25, p. 4593, 2003.

[77] R. Chu, Y. Zhou, J. Liu, D. Wang, K. J. Chen, and K. M. Lau, "AlGaN-GaN double-channel HEMTs," *Electron Devices, IEEE Transactions on*, vol. 52, no. 4, p. 438, 2005.

[78] Y. Cordier, F. Semond, M. Hugues, F. Natali, P. Lorenzini, H. Haas, S. Chenot, M. Laugt, O. Tottereau, and P. Vennegues, "AlGaN/GaN/AlGaN DH-HEMTs grown by MBE on Si(111)," *Journal of Crystal Growth*, vol. 278, no. 1-4, p. 393, 2005.

[79] E. Bahat-Treidel, O. Hilt, F. Brunner, J. Wrfl, and G. Trnkle, "AlGaN/GaN/AlGaN double heterojunction HEMTs on n-type SiC substrates," *physica status solidi (c)*, vol. 7, no. 10, p. 2408, 2010.

[80] A. Zhang, L. Rowland, E. Kaminsky, V. Tilak, J. Grande, J. Teetsov, A. Vertiatchikh, and L. Eastman, "Correlation of device performance and defects in AlGaN/GaN high-electron mobility transistors," *Journal of Electronic Materials*, vol. 32, no. 5, p. 388, 2003.

[81] H. Yu, S. B. Lisesivdin, B. Bolukbas, O. Kelekci, M. K. Ozturk, S. Ozcelik, D. Caliskan, M. Ozturk, H. Cakmak, P. Demirel, and E. Ozbay, "Improvement of breakdown characteristics in AlGaN/GaN/$Al_xGa_{1-x}N$ HEMT based on a grading $Al_xGa_{1-x}N$ buffer layer," *physica status solidi (a)*, vol. 207, no. 11, p. 2593, 2010.

[82] R. Gaska, M. S. Shur, T. A. Fjeldly, and A. D. Bykhovski, "Two-channel AlGaN/GaN heterostructure field effect transistor for high power applications," *Journal of Applied Physics*, vol. 85, no. 5, p. 3009, 1999.

[83] Q. Si, H. Yue, M. Xiaohua, Z. Pengtian, and X. Yuanbin, "AlGaN/GaN double-channel HEMT," *Journal of Semiconductors*, vol. 31, no. 4, p. 044003, 2010.

[84] E. Cho, F. Brunner, R. Zhytnytska, P. Kotara, J. Wurfl, and M. Weyers, "Enhancement of channel conductivity in AlGaN/GaN heterostructure field effect transistors by AlGaN:Si back barrier," *Applied Physics Letters*, vol. 99, no. 10, p. 103505, 2011.

[85] J. Liu, Y. Zhou, J. Zhu, K. M. Lau, and K. J. Chen, "AlGaN/GaN/InGaN/GaN DH-HEMTs with an InGaN notch for enhanced carrier confinement," *Electron Device Letters, IEEE*, vol. 27, no. 1, p. 10, 2006.

[86] K. H. Lee, P. C. Chang, S. J. Chang, Y. K. Su, and C. L. Yu, "AlGaN/GaN high electron mobility transistors based on InGaN/GaN multiquantum-well structures," *Applied Physics Letters*, vol. 96, no. 21, p. 212105, 2010.

[87] M. Zervos, A. Kostopoulos, G. Constantinidis, M. Kayambaki, S. Mikroulis, N. Flytzanis, and A. Georgakilas, "The pinch-off behaviour and charge distribution in AlGaN-GaN-AlGaN-GaN double heterostructure field effect transistors," *physica status solidi (a)*, vol. 188, no. 1, p. 259, 2001.

[88] H. Kim, F. Flth, and T. Andersson, "Unintentional incorporation of B, As, and O impurities in GaN grown by molecular beam epitaxy," *Journal of Electronic Materials*, vol. 30, no. 10, p. 1343, 2001.

[89] G. Orsal, N. Maloufi, S. Gautier, M. Alnot, A. A. Sirenko, M. Bouchaour, and A. Ougazzaden, "Effect of boron incorporation on growth behavior of BGaN/GaN by MOVPE," *Journal of Crystal Growth*, vol. 310, no. 23, p. 5058, 2008.

[90] Y. Bi, X. L. Wang, H. L. Xiao, C. M. Wang, E. C. Peng, D. F. Lin, C. Feng, and L. J. Jiang, "The influence of the InGaN back-barrier on the properties of $Al_{0.3}Ga_{0.7}N$/AlN/GaN/InGaN/GaN structure," *The European Physical Journal Applied Physics*, vol. 55, no. 1, p. 10102, 2011.

[91] O. Kelekci, S. B. Lisesivdin, S. Ozcelik, and E. Ozbay, "Numerical optimization of In-mole fractions and layer thicknesses in $Al_xGa_{1-x}N$/AlN/GaN high electron mobility transistors with InGaN back barriers," *Physica B: Condensed Matter*, vol. 406, no. 8, p. 1513, 2011.

[92] J. Dickerson, K. Pantzas, T. Moudakir, P. Voss, and A. Ougazzaden, "Modeling of n-i-p vs. p-i-n InGaN solar cells with ultrathin GaN interlayers for improved performance," in *Numerical Simulation of Optoelectronic Devices (NUSOD), 2012 12th International Conference on*, p. 113, 2012. 2012 IEEE, Reprinted with permission.

[93] J. R. Dickerson, K. Pantzas, T. Moudakir, P. L. Voss, and A. Ougazzaden, "Modeling of n-i-p vs. p-i-n InGaN solar cells with ultrathin GaN interlayers for improved performance," *submitted to Optical and Quantum Electronics*, 2012. with kind permission from Springer Science and Business Media 2012.

[94] J. R. Dickerson, K. Pantzas, A. Ougazzaden, and P. L. Voss, "Polarization-induced electric fields make robust n-GaN/i-InGaN/p-GaN solar cells," *submitted to IEEE Electron Device Letters*, 2012. 2012 IEEE, Reprinted with permission.

[95] J. Nelson, *The Physics of Solar Cells*. London: Imperial College Press, 2003.

[96] G. Simin, X. H. Hu, A. Tarakji, J. P. Zhang, A. Koudymov, S. Saygi, J. W. Yang, A. Khan, M. S. Shur, and R. Gaska, "AlGaN/InGaN/GaN double heterostructure field-effect transistor," *Japanese Journal of Applied Physics Part 2-Letters*, vol. 40, no. 11A, p. L1142, 2001.

[97] H. Xing, D. S. Green, H. Yu, T. Mates, P. Kozodoy, S. Keller, S. P. DenBaars, and U. K. Mishra, "Memory effect and redistribution of mg into sequentially regrown GaN layer by metalorganic chemical vapor deposition," *Japanese Journal of Applied Physics*, vol. 42, no. 1, p. 50, 2003.

[98] www.universitywafer.com, 2012.

[99] L. Esaki, "New phenomenon in narrow germanium $p - n$ junctions," *Phys. Rev.*, vol. 109, pp. 603–604, 1958.

[100] S.-R. Jeon, Y.-H. Song, H.-J. Jang, G. M. Yang, S. W. Hwang, and S. J. Son, "Lateral current spreading in gan-based light-emitting diodes utilizing tunnel contact junctions," *Applied Physics Letters*, vol. 78, no. 21, pp. 3265–3267, 2001.

[101] T. Takeuchi, G. Hasnain, S. Corzine, M. Hueschen, R. P. S. Jr., C. Kocot, M. Blomqvist, Y. lan Chang, D. Lefforge, M. R. Krames, L. W. Cook, and S. A. Stockman, "Gan-based light emitting diodes with tunnel junctions," *Japanese Journal of Applied Physics*, vol. 40, no. Part 2, No. 8B, pp. L861–L863, 2001.

[102] M. Grundmann, J. S. Speck, and U. K. Mishra, "Tunnel junctions in gan/aln for optoelectronic applications," in *Device Research Conference Digest, 2005. DRC '05. 63rd*, vol. 1, pp. 23–24, 2005.

[103] D. K. Ferry, *Quantum Mechanics An Introduction for Device Physics and Electrical Engineers*. Bristol and Philadelphia: Institute of Physics Publishing, 2001.

[104] B. Ricco and M. Y. Azbel, "Physics of resonant tunneling. the one-dimensional double-barrier case," *Physical Review B*, vol. 29, no. 4, p. 1970, 1984.

[105] Y. Ando and T. Itoh, "Calculation of transmission tunneling current across arbitrary potential barriers," *Journal of applied physics*, vol. 61, no. 4, pp. 1497–1502, 1987.

[106] J. S. Walker and J. Gathright, "Exploring one-dimensional quantum mechanics with transfer matrices," *American Journal of Physics*, vol. 62, pp. 408–422, 1994.

[107] C. R. Crowell and S. M. Sze, "Quantum mechanical reflection of electrons at metal semiconductor barriers: Electron transport in semiconductor metal semiconductor structures," *Journal of Applied Physics*, vol. 37, no. 7, pp. 2683–2689, 1966.

[108] N. Kluksdahl, A. Kriman, D. K. Ferry, and C. Ringhofer, "Self-consistent study of the resonant-tunneling diode," *Physical Review B*, vol. 39, no. 11, p. 7720, 1989.

[109] J. Soderstrom, D. Chow, and T. McGill, "New negative differential resistance device based on resonant interband tunneling," *Applied Physics Letters*, vol. 55, no. 11, pp. 1094–1096, 1989.

[110] D. Day, R. Q. Yang, J. Lu, and J. Xu, "Experimental demonstration of resonant interband tunnel diode with room temperature peak-to-valley current ratio over 100," *Journal of applied physics*, vol. 73, no. 3, pp. 1542–1544, 1993.

[111] H. Tsai, Y. Su, H. Lin, R. Wang, and T. Lee, "Pn double quantum well resonant interband tunneling diode with peak-to-valley current ratio of 144 at room temperature," *Electron Device Letters, IEEE*, vol. 15, no. 9, pp. 357–359, 1994.